CHARACTERIZATION OF CATALYST MATERIALS FOR PEMFCS USING ANALYTICAL ELECTRON MICROSCOPY

In Loving Memory of My Dear Dad

I Miss You so Much

Characterization of Catalyst Materials for PEMFCs using Analytical Electron Microscopy

By

FEIHONG NAN, M.A.Sc.

A Thesis

Submitted to the School of Graduate Studies

in Partial Fulfillment of the Requirements

for the Degree of

Doctor of Philosophy

McMaster University

DOCTOR OF PHILOSOPHY (2015) McMaster University

Department of Materials Science and Engineering Hamilton, Ontario

TITLE: **Characterization of Catalyst Materials for PEMFCs using Analytical Electron Microscopy**

AUTHOR: **Feihong Nan, M.A.Sc (McMaster University)**

SUPERVISOR: **Gianluigi A. Botton**

NUMBER OF PAGES: **XIV, 145**

Abstract

The goal of current research is probing the relationship between catalyst features and the fuel cell performance with a range of in-depth structural analysis. The study investigated different catalyst systems including core-shell structured catalyst, catalysts with unique carbon-transition metal oxide supports.

PtRu catalysts nanoparticles with unique core-shell structure, one of the most practical catalysts in PEMFC technology, have been successfully obtained with the evidence from the characterization results. It is found that the enhanced CO oxidation may be achieved through the interactions between the Pt shell and Ru core atoms, which can modify the electronic structure of the Pt surface by the presence of subsurface Ru atoms or by disrupting the Pt surface arrangement. Furthermore, the possibility of presence of the compressive strain within the Pt rich shell is proved by the lattice measurements, which could significantly affect the catalytic activity.

Pt catalysts supported on complex oxide and carbon support were studied to investigate the relationship between the catalyst and its support. Observations from STEM images and HAADF and energy dispersive X-ray spectrometry demonstrate the preferential distribution of Pt nanoparticles on the hybrid supports, which include Nb_2O_3 / C, Ta_2O_5 / C, (Nb_2O_3+TiO_x) / C, (Ta_2O_5+TiO_x) / C, and (WO_3+TiO_x)/C). Such evidence indicates the interaction between the catalyst and support is based on the presence of an interconnected oxide network over the carbon support and the presence of Pt strongly connected to the oxide network. In addition, using electron energy loss spectroscopy (EELS), the electronic structure of the catalyst support under various conditions was also studied to provide further evidence of the strong metal support interaction effect.

Acknowledgements

The path towards this thesis is the journey involving years of scientific research and contribution of many people. This journey is also the philosophy questioning myself all the time and studying the nature of the reality, existence, knowledge, values, and reason, not only for work, but also for life. I would like to thank everyone who has supported and inspired me during my entire doctoral study.

The first person I would like to thank is my supervisor Dr. Gianluigi Botton for his great encouragement, invaluable suggestions, and financial support helped me to complete this Ph.D. work.

I wish to thank Dr. Jiujun Zhang's research group at Institute of Fuel Cell Innovation in British Columbia, for the continuous support on not only providing series of samples, but also helpful discussion and opportunity to complete this work.

I would like to thank Dr. Milan Jaksic at University of Patras in Greece, his hard work ensures an excellent source of high quality samples I could study in details.

I wish to thank Dr. Matthieu Bugnet, for his generous help, often late of night, helped me in acquisition EELS spectra and many discussion about the experimental approach.

I am also very grateful to CCEM, a place where I received a number of trainings on analytical electron microscopy, a place I worked with a big and nice "family", a place about good memory.

Finally, I would like to thank my beloved husband Yi Yang and my dearest parents, for the motivation they gave me, the freedom to follow my mind, and their never-ending support.

Table of content

List of Figures

Chapter 1. Introduction to PEMFCs

H_2/air Proton Exchange Membrane Fuel Cells (PEMFCs) have many attractive features, including low or zero emissions, high power density and rapid start-up, which make them the most clean and efficient energy technology for automobiles and stationary power plants. Therefore it is easy to understand that even ten years ago, the US already invested in an energy bill that included over a billion dollars in incentives for automakers to develop technology related to Fuel-Cell Vehicles, [1] later six world-wide major automakers signed a memorandum of understanding in September 2009, to develop light duty fuel cell vehicles and the accompanying H_2 facilities. In the meantime, various government energy departments have also taken a positive attitude toward fuel cell funding. The American Department of Energy awarded the Fuel Cell Energy industry with approximately $1.9 million for the development of the fuel cell infrastructures. The United Kingdom launched a £7.2 million competition for hydrogen and fuel cell demonstrations. [1-5]

A major challenge facing PEMFCs is degradation of the membrane and catalyst. Currently, over 90% of the research effort is focused on improving the membrane of PEMFCs, while only a few studies were conducted on the catalyst layers. These catalyst layers are the most important components during fuel cell operation, performance of which is usually governed by the precise atomic structure and composition of very specific

catalytically active sites. Therefore, structural and chemical characterization at the atomic scale becomes a key aspect in order to investigate any structure–performance relationships existing in fuel cell catalyst systems. It is also obvious that the detailed characterization of the catalyst layers is very important for several reasons: (i) to develop new catalysts with high activity and durability; (ii) to determine the structures of catalysts, and (iii) to investigate the interaction mechanism of the catalyst layer. [6-11]

The activity and stability of the new catalysts are significantly affected by the surface area and morphology. High-resolution transmission electron microscopy (HRTEM) is therefore necessary for structural analysis at the atomic scale. Knowing the valence state variation of the dopants to the catalysts is also key to understanding the oxidation behavior during the electrode reaction. Therefore, quantitative element mapping and valence state distribution are also necessary and have been achieved in this work using scanning transmission electron microscopy–electron energy-loss spectroscopy STEM-EELS.

1.1 Historical development of PEMFC

The history of fuel cell can be traced back to 1839 while Sir William Grove, who is considered as "the father of the fuel cell", found that electrolysis could be performed in reverse with the right catalyst, producing electricity. However, for almost a century there

was not any significant practical progress after Grove's discovery the fuel cell, remaining only a scientific curiosity. It was not until 1937, Francis T. Bacon started to work on practical fuel cells. By the end of 1950 Francis Bacon developed a 40-cell stack that was able to power a welding machine, circular saw, and forklift [12]

PEM fuel cell technology served as one part of the NASA's Gemini Program from 1950s to 1970s. In early 1960s, the PEM fuel cells were invented at General Electric (GE) by Thomas Grubb and Leonard Niedrach. Initially, sulfonated polystyrene membranes were used as the solid electrolytes. Then they were soon replaced by Nafion® membranes in 1966 due to the improved performance and durability. Nafion membranes are still the most popular membrane in use today. [6]

Fuel cell systems were limited to space missions and other special applications due to their high cost. However the research in late 1980s and early 1990s by Ballard Power Systems (founded in 1979) enabled fuel cells to be a pratical option for wider applications. Soon in 1983, Ballard began developing PEM fuel cells.[6]

Today, the interest in the research and development of PEM fuel cells has been intensified, and has attracted more and more involvements of scientific institutes and universities over the world becoming involved. Till now, several key innovations, such as the low platinum catalyst loading, novel membranes, and new bipolar plates, have continuously made the application of PEMFC systems more or less realistic. [6]

1.2 Components and operation of PEMFCs

A PEMFC stack include membrane, electrodes, gas diffusion layer and bipolar plates (as illustrated in Figure 1-1). One of the key components of PEMFCs is the proton exchange membrane, the lifetime of which determines the lifetime of PEMFCs. The membrane separates the fuel and the oxidant, preventing the mixing of the two gases. Another important role taken by PEMFC polymer membranes is to facilitate the transport of the protons from the anode to the cathode by sulfonic groups within the membrane. Thus, one ideal polymer membrane must possess excellent proton conductivity, chemical and thermal stability, strength, flexibility, and at the same time low cost and low gas permeability as well. [13]

Anode, the negative electrode, is the hydrogen feed side where the hydrogen splits into its primary constituents, protons and electrons. Protons first travel through the membrane, then meet with catalyst sites between membrane and the other electrode, while electrons are traveling through electrically conductive electrode, current collector and external circuits where they perform useful works. At the oxygen feed side, the cathode (positive electrode), water is generated from the electrochemical reaction and pushed away with the excess of the oxygen flow. Net results from anode and cathode are a direct electrical current at the external circuits, usually about 1V. [6]

Another critical component in PEMFC is gas diffusion layers GDLs (or the backing layers), main function of which is to diffuse the gas. The porous nature of the GDLs facilitates the effective diffusion of each reactant gas to the catalyst. In addition to that, the GLD is also building up the electrical connection between catalyst and current collectors, such as bipolar plates. Water management is also achieved through the GLD by carrying the product water away from the electrolyte surface.

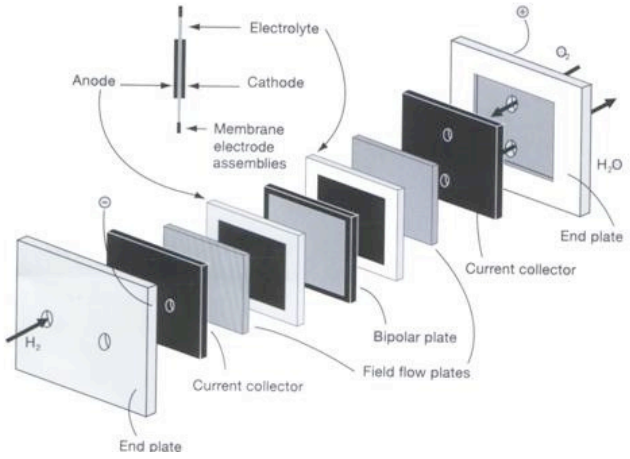

Figure 1-1 Schematic diagram of the PEMFC, image courtesy of fuelcell.org.au

The bipolar plate is considered as a multi-function component in the fuel cell stack, however it is also costly and problematic. The primary role of bipolar plate is to supply reactant gases to the gas diffusion electrodes through flow channels, flowfield design of which could affect the effectiveness of the reactant transport. Bipolar plates must provide electrical connections between the individual cells, and also be able to remove the product water at the cathode effectively. [6]

The principle of how a PEM fuel cell generates electricity is straightforward. However, the cell power output depends on material properties, cell design and structure, and operation conditions, such as the gas flow, pressure regulation, heat, and water management. High performance of a PEM fuel cell requires maintaining optimal temperature, membrane hydration, and partial pressure of the reactants across the membrane to avoid any degradation of performance. These critical operation parameters must be controlled over a wide range of current.[13]

1.3 Advantages and applications

Proton exchange membrane fuel cells (PEMFCs) have many promising advantages: higher efficiency than in the conventional internal combustion engines and power plants; low or zero emissions since the only exhaustion is the unused air and water from the fuel cell operation, which is attractive not only for transportation but also for indoor applications and submarines; simplicity and promising of low cost because the structure of fuel cell is usually layers of repetitive components and no moving parts; a wide range of size and weight since fuel cells can be made in a variety of sizes-from microwatts to megawatts. The numerous advantages make the PEMFC particularly promising for applications in the fields of transportation, home-based distributed power distribution, and portable power supplies. [13]

1.4 Challenges and Objectives

PEMFCs are considered the next generation of fuel cell technology due to their low cost reduction and reliability in terms of enhanced electrochemical kinetics and catalyst tolerance, simplified cooling process, and improved water management. In spite of these successes, several technique challenges hindered their widespread commercialization, among which the high cost, unsatisfactory durability and operation flexibility are the top three. [6,14]

The most widely used catalysts in low temperature PEMFCs are based on Pt with carbon support materials, the stability and durability of which is always a challenging issue for long-term and high temperature fuel cell operation. During the cell operation, poisoning effects due to the impurities from the fuel, Pt sintering or agglomeration can make the catalysts loss the electro-active surface loss on the catalysts, resulting in a degradation of the fuel cell performance. Therefore, it is essential to develop new catalyst with reduced Pt usage and effective supporting materials which offers stronger interaction to avoid the loss of active-surface. [6]

It is also critical to understand the chemical reactivity of the catalyst layer in commercially important PEMFC technologies. However, currently there are very limited detailed studies focused on how the nanostructures affect the catalytic activity and stability of the catalyst layer, and how the cell performance change consequently.

Furthermore, it is also important to achieve the deeper insight of the change of the Pt loading on the support materials during the fuel cell operation, such as the shape, size and distribution, which significantly affect the stability and catalytic activity of the catalyst layer. [15]

For example, titanium oxides such as Ti_nO_{2n-1} (Magnéli phases), one of the novel catalyst supporting materials, attract significant theoretical and industrial interest for their structural, electrical, and catalytic properties. Magnéli phases are important representatives of transition metal oxides with variable valences of the parent metal and can form extended series of compounds. Moreover, there is also added disorder in such superstructures as compared with standard idealized crystallographic phases [16]. However, there is no systematically investigation applied on these oxides to study the change of the valence state and the distortion within the structure because those work require a much higher resolution on the observation techniques. Furthermore, there are also no in-situ studies and morphology characterizations applied on the dynamic catalysis process. Moreover, characterizations of the morphology at atomic level before and after fuel cell working cycles are also lacking. This information plays an important role to explore and provide a better understanding of the interaction between the catalyst support and catalyst materials and atomic interfacial transformations in other transition metal carbides and oxides.

To overcome these challenges, initially comparable studies of the morphology and microstructure of the catalyst support were carried out using X-Ray Diffraction (XRD), High Resolution Transmission Electron Microscopy (TEM) as well as the electron diffraction. In situ and tomography measurements were also conducted to track the dynamic process of the catalyst materials which including the change of the distribution, morphology and the size of the active catalytic particles supported on the transition metal oxides and carbides. EELS and EDX mapping will be applied in the studies of the doping effect on the valence state, element distribution and cell performance.

Based on the investigations proposed, a clearer picture can be drawn on the relationship between catalyst features and the fuel cell performance. The efficiency and durability of PEMFCs will be significantly improved by using stable catalyst with stronger interaction within the catalyst layer. The synthesis routes of the new catalysts will be also optimized according to the analysis of the measurements. Therefore, the fabrication cost will also be greatly reduced compared with the conventional Pt-loaded catalyst with higher mass ratio.

Chapter 2. Literature Review of PEMFC Catalyst

The important challenges in PEMFC research arise in the catalyst layers (CLs) due to their complexity and heterogeneous structure. The catalyst layers need to be designed to generate high rates of the desired reactions and minimize the amount of catalyst usage for reaching the required levels of power output. To meet the goal, the following requirements need to be considered: (1) large three-phase interface in the CL, (2) efficient transport of protons, (3) easy transport of the reactant and the product gases and removal of condensed water, and (4) continuous electronic current passage between the reaction sites and the current collector. The overall CL performance depends on all these critical factors and is therefore essential to identify the electrode structures and operation conditions. [6]

2.1 Components and Structure of CLs

The catalyst layer includes ionic conductor, metal catalysts, and water-repelling agent. Ionic conductors, such as perfluorosulfonate acid ionomer, are used in CLs to provide a passage path for protons transportation. Metal catalysts supported on conducting matrix (carbon) provide path for electron conduction. Water-repelling agent provides sufficient porosity for the gaseous reactants to be transferred to catalyzed sites. The catalyst ink in

the PEMFC system usually consists of catalyst, carbon powder, binder, and solvent, other additives might be sometimes added in order to improve the dispersion and stability of the catalyst ink. [6,6-12,17]

2.2 Functions and Reactions (Roles of the CL)

In a H_2/O_2 (or air) PEMFC, the cathode and the anode reactions are respectively the oxygen reduction reaction (ORR) and the hydrogen oxidation reaction (HOR), as shown below

$$O_2 + 4H^+ + 4e^- \leftrightarrow 2H_2O \text{ (ORR)}$$

$$H_2 \leftrightarrow 2H^+ + 2e^- \text{ (HOR)}$$

The relationship between the cathode (anode) current density *Ic* (I_a): and the over potential $\eta_c(\eta_a)$ is given by the following Equations:

$$I_c = i^o_{O_2}\left(e^{\frac{n_{aO}\alpha_O F\eta_c}{RT}} - e^{-\frac{n_{aO}(1-\alpha_O)F\eta_c}{RT}}\right)$$

$$I_a = i^o_{H_2}\left(e^{\frac{n_{aH}\alpha_H F\eta_H}{RT}} - e^{-\frac{n_{aH}(1-\alpha_H)F\eta_H}{RT}}\right)$$

$i^o_{O_2}(i^o_{H_2})$: The exchange current density for cathodic O_2 reduction/ anodic H_2 oxidation;

n_{aO} (n_{aH}): The number of electrons transferred in the rate determining step;

α_O(α_H): The electron transfer coefficient;

F: the Faraday constant;

R: the gas constant (8.314 J.mol–1.K–1);

T: the temperature (K)

In a fuel cell, the reaction kinetics is mainly dominated by the O_2 reduction reaction since the exchange current density of H_2 oxidation (10^{-4} A/cm^2) is significantly larger than that of O_2 reduction (~10^{-9} A/cm^2).

The exchange current density change with temperature follows the Arrhenius Equations, respectively

$$i^o_{O_2} = I^o_{O_2} e^{-(E_a/RT)}$$

$$i^o_{H_2} = I^o_{H_2} e^{-(E_a/RT)}$$

$i^o_{O_2}$ ($i^o_{H_2}$) : The cathode (anode) exchange current densities at infinite temperature;

E_c(E_a): The reaction activation energies for the cathode (anode)

According to above equations, an increase in the exchange current density is dominated by the reaction activation energies, the values of which are strongly dependent on the catalysts used.[6,13,18]

2.3 Catalyst support materials for PEM Fuel Cells

Catalysts are the key materials in the PEMFCs. Nano-structured Pt particles dispersed on carbon materials are still the most widely used catalysts for both anode and cathode in PEMFCs.[19] However, the high cost and limited resources of Pt hinder fuel cell practical applications. Another serious problem is that Pt is readily poisoned by the CO-like species produced during the alcohol oxidation even at ppm level. Therefore, efforts have been focused on either reducing the Pt loadings by forming Pt alloys with others metals or exploring non-noble catalysts to minimize the catalyst cost. Among various non-noble catalysts, transition metal carbides or oxides as Pt alternatives and support materials attract a lot of attention. On the other hand, tungsten carbides or nitrides as novel supports have been evaluated to be a promising candidate not only because of their catalytic is similar to that of platinum group metals, but also because of their enhanced the resistance to CO and bisulphide poisoning.

2.3.1 Transition metal oxide as support materials for PEMFC

It is necessary for the support materials in PEMFC catalyst to achieve a high surface area, in order to provide sufficient physical area for dispersion of the small catalyst

particles. There are additional requirements for electrochemical reactions under fuel cell operation; the catalyst support materials must have high conductivity, CO tolerance and corrosion resistance to allow efficient charge transfer and stable operation.

In recent years, catalysts based on transition metal oxides modified by platinum group metals have attracted more and more attention as new electrode material and catalyst support in fuel cell applications. It was shown that, titanium oxides such as Magnéli phase (which have been commercially recognized under the *Ebonex*® trade name) exhibit unique electrical conductivity and high chemical stability. The electrical conductivity of these transition metal oxides can match those of carbon and graphite, which is frequently, used in catalyst support layers for fuel cell. In addition to that, their high corrosion resistance and stability in aqueous electrolytes make them the one of the most promising candidates as catalyst supports. Furthermore, these materials have a wide potential window with a large overpotentials for hydrogen and oxygen evolution and unique electron transfer kinetics also make them more suitable as the catalyst support. [11,13] These oxides show remarkable characteristics in their crystalline structures as well as electrical properties. These blue/black ceramic materials can be produced from high temperature reduction of titania in a hydrogen atmosphere and exhibit conductivity comparable to that of graphite and can be produced in a number of forms, such as tiles, rods, fibers, foams and powders. For PEMFC systems,

Ebonex has been considered as a unique electron conductive and interactive support for electrocatalysis support both in hydrogen and oxygen electrode reactions. The Strong Metal-Support Interaction between Ebonex and Pt loading is related to: the hypo–hyper d-inter bonding effect and its catalytic consequences, which will be explained in the following section. The stronger bonding in Ti_nO_{2n-1} supported Pt compared with that of conventional carbon supported Pt, results in the less strong the intermediate adsorptive strength in the rate determining step (RDS) in fuel cell operation, and therefore, the faster catalytic electrode reaction. [20] [21]

2.3.2 Strong metal-support interaction (SMSI) effect

The strong metal-support interaction (SMSI) effect was first reported by Tauster in 1978 and attracted widespread interest for decades particularly in a number of heterogeneous catalysis processes. The most important signature of the SMSI effect accounts for the drastic changes in the performance of the catalyst when group VIII metals like Pt, supported on transition metal oxides, are reduced at elevated temperature. The Brewer theory a priori has predicted one would expect transfer of d electrons from platinum (d^7sp^2) to low-lying vacant orbitals of titanium, for every electron transferred with resulting unpairing of two internally paired electrons, two electrons are made available for bonding by pairing between atoms, and the most stable and most strong

hypo-hyper bonding between Ti and Pt is symmetric $TiPt_3$. Tauster also proposed that at the interphase Pt/TiO_2 should grow and appear the intermetallic phase $TiPt_3$ as the indication. For over 30 years, numerous of researchers have studied SMSI effect though various approaches as below:

1) Building up models of the SMSI phenomenon by theoretical discussions and calculations including thermal programed desorption (TPD) and first-principles density functional theory DFT;

2) Tailoring the selectivity and enhancing the activity of the catalysts; [22] [23] [24] [25] [26] [27]

3) Detecting the SMSI behavior on CO adsorption and hydrogenation by using XRD, [28,29] TPR, XPS, [13,30] [6,14,31] TOF-SIMS, [6,32] coaxial impact–collision ion scattering spectroscopy (CAICISS) reflection high-energy electron diffraction (RHEED), [15,33] in situ ambient pressure photoemission spectroscopy (APPES) [16,34] and in Situ Electrochemical X-ray Absorption Fine Structure Study .[6,35]

It has been shown for many highly active heterogeneous catalyst systems that, in some cases, the relevant catalytic structure may only constitute a minor part of the catalyst material. Conventional optical and X-ray spectroscopy characterization tools have the drawback of obtaining spatially averaged information over a relatively large surface area. These techniques must be complemented with local structure and compositional analysis

techniques available with Analytical Electron Microscopy (AEM), a powerful structure solving toolbox, allowing insight into the complexity of the supported catalyst nanoparticles. Earlier electron microscopy studies were carried out by Baker and his colleagues in 1979 (right after SMSI mechanism was proposed) who demonstrated that Pt supported on TiO_2 exhibited unique features which are not apparent with conventional supports. [36-38] In the past decades, AEM characterization has experienced a number of parallel revolutionary advances in the design of the microscopes, electronic devices for their control, data acquisition and processing. [39] These new tools lead to enhanced capabilities for researchers to probe the microscopic nature of the active sites [6,40,41] [13,42-44] [13,45-47] and to obtain local details regarding the nature of the SMSI state of transition metal oxide supported platinum catalysts. [40,48-50] [43,44,51-54] However, the catalyst systems presented in these works are not close to the real catalyst used in fuel cell application. Previous work has focused on the structural details of specific orientation, e.g. Pt/TiO_2 (110), or Pt on titania powder, very little work was directly conducted to the system used in industrial application. [44,55] In addition to that, it is challenging to get further structure details regarding the SMSI effect due to the limited spatial and energy resolution. There has been no detailed analysis done directly on the mechanism of the SMSI effect down to the atomic structure leading, for example, to the morphology variations under different catalyst supports. Furthermore, there is no direct evidence showing the electronic structure effects contributing to SMSI effects.

2.4 Physical Characterization Techniques of PEM Fuel Cells

The physical characterization of catalyst layers in PEMFC plays an essential role for the development of new catalyst materials with high activity and high stability, investigating the material structures, and exploring the mechanisms of catalysts and certain dopants.

General physical characterization methods of PEMFC catalyst materials include the measurement of the specific surface area, identifying the phase and composition of catalytic composites, determination of the particle size and distribution of active components, characterization of the morphology as well as other features of the catalysts and support materials. [6,56]

The surface area of solids has been recognized as an important feature in various research fields including PEMFC systems, because it is capable of affecting the properties of materials in different types. Therefore, it is critical to characterize and control the surface area as well as electrochemical surface activity accurately. For determining the surface area, the BET method, named after Brunauer, Emmett, and Teller who established this technique in 1938, is the most widely used technique. The BET method is based on the understanding of the adsorption of gases by a solid material with a

complicated shape, and therefore helped researchers draw an insight picture of the relationship between surface area and adsorbed gas components. [20,57]

X-ray diffraction (XRD) is another popular physical characterization technique used in PEMFC research. This non-destructive technique can provide detailed information about the chemical composition and crystallographic structure of the materials such as catalyst layer and membrane in fuel cell. The catalytic activity is strongly dependent on the particle size and shape, as well as the active component distribution, which can be investigated by using XRD measurement. Moreover, catalyst support materials are also very important to optimize the performance of the catalyst layer, composition of which can be determined by XRD. [6,21]

A number of electrochemical characterization methods can be used to evaluate the performance of the fuel cell. Characterization of new catalysts and the reaction mechanisms and kinetics studies can be achieved by controlled potential techniques (e.g., potential step, potential sweep, and potential cycling). Rotating (ring) disk electrodes, cyclic voltammetry, and impedance spectroscopy are also widely used in the investigation of the electrochemical properties of the materials.

Chapter 3. Overview of analytical electron microscopy for catalysts

Catalysis plays key role in the industrial world, since more than 90% of industrial chemical processes and it is essential for large-scale production of plastics and fuel. The properties of a catalyst are determined by its microstructure and chemistry on an atomic scale. [22,58-62] A wide range of techniques has been developed to characterize the composition and structure of the catalysts from single-crystals of metals to alloys or oxides. The characterization traditionally has been achieved using optical spectroscopy techniques (including UV–vis, Raman, and infra-red (IR) spectroscopies) and X-ray techniques (including X-ray diffraction (XRD), small angle X-ray scattering (SAXS), extended X-ray absorption fine structure (EXAFS), X-ray absorption near edge structure (XANES), and X-ray photoelectron spectroscopy (XPS)). [23,63-65] However averaged information generated from these techniques in the characterization of commercial catalysts limit their value in determining structural, electronic, or compositional information for functioning catalysts.

No other single tool rivals analytical electron microscopy (AEM) in such a wealth of diverse information concerning solid catalysts and their surfaces. With high-resolution imaging capabilities, with a powerful scanning electron probe, and with an electron

energy loss spectroscopic (EELS) and Energy Dispersive X-ray Spectroscopy, AEM provides essential structural, morphological, and electronic information of solid catalysts used commercially, for laboratory researches or model studies. AEM also provides deep insights into the atomic structure and chemistry of reactions that profoundly influence catalytic properties: such as the location of active sites, especially those atoms at active sites and their coordination to surrounding atoms; the atomic structure of the framework, as well as the nature of its nanoporosity for the porous catalyst and catalyst supports. These approaches have actively promoted the development of new catalysts, solved complex structures, assisted scientists to determine the structure and chemical compositions.

3.1 Historical development of AEM on catalyst (Time line)

Here is a chronological review of the major developments in electron microscopy and examples of applications of this technique in the area of catalysis is provided while details technical description of the techniques is described in the subsequent sections. One of the biggest milestones of the AEM history starts with the pioneer work conducted by Ernst Ruska in 1939, who won the Nobel Prize in 1986 due to his great contribution to electronic microscope development. One year later in 1940, M. von Ardenne and D. Beischer presented TEM micrograph of platinum oxide. [22,24,66] One of the earliest surveys

of the application of EM to the study of catalyst was published by Turkevich in 1945 at RCA Research Laboratories at Princeton, and EM work is conducted by Drs. J. Hillier and R. F. Baker. [23,25,67] It was not until 1968, A. V. Crewe initiated pioneer work on STEM HAADF, technique of which later on became one of the most popular characterization approaches for analyzing structure details of the catalyst. [24,26,68]

Major improvements in the resolution and spectroscopic capabilities took place around 1970s, with earlier HRTEM images and HRTEM technique breakthrough reported in the Iijima's paper on the structure of oxides. [25,27,69] Key research related to aberration corrected imaging and spectroscopy started from 1936 while Scherzer raised up the theoretical proof that spherical aberration-correction Cs and Chromatic aberration correction Cc are unavoidable with round electron lenses. (Scherzer O. (1936) "Über einige Fehler von Elektronenlinsen", Z. Physik 101, 593). Followed by over decades of theoretical research and experimental trials, the first demonstration of working sextupole/round lens/sextupole image Cs corrector was introduced in Haider's report (Haider M., Braunshausen G. and Schwan E. (1995) "Correction of the spherical-aberration of a 200-KV TEM by means of a hexapole-corrector", Optik 99, 167). [26,28,29,70,71]

One of the earliest works on imaging single atoms to clusters particles, usually the popular form of catalyst, was also achieved by James and other scientists. [27,72,73] Soon after,

more scientists started to realize the important role of HRTEM application in catalyst materials research and widely applying the technique to extract more information on these materials.[28,29,74,75] On top of that, other AEM techniques including EELS and plasmon energy mapping and electron tomography were also efficiently used in heterogeneous catalysts. [76] [77]

In the past ten years, diverse studies on catalyst materials using AEM, were reported including a detailed review of the technology development and application. [78] For example, atomic scale characterization of the Pt/TiO_2 interface provided evidence related to the strong interaction between catalyst and support (2005) [44]; it was also reported in 2006 that it is possible to conduct atomic resolution chemical analysis in a scanning transmission electron microscope [79]; using spherical aberration corrected HRTEM, direct observation of oxygen atoms in rutile TiO_2 was reported by Yoshida in 2006. [9] Various system of catalyst including Ag/SiO2 and Au/FeOx were also studied using aberration-corrected microscopes by different groups of research scientists.[80] [64] [81,81,82]

With the development of advanced technology and improved accessories in AEM, more and more original and informative works were undertaken for example using specialty heating stages to study temperature treatment to the catalyst material (2009) [83,84] and electron tomography. In addition, 4-dimensional electron tomography (Kwon, 2010) provided additional insight in catalyst research by adding time series so that mechanical

motion of catalysts, morphological dynamics could be monitored. [85] Similarly, tracking of the controlled growth of nanoparticles from solution was also achieved using in-situ Liquid Transmission Electron Microscopy which was first reported by Evans in 2011. [86] Furthermore, Scott reported a method of advanced electron tomography with improved resolution of 2.4-ångström in 2012 for providing more details in 3-dimension [87]; visualizing gas molecules interacting with supported nanoparticulate catalysts at reaction conditions become possible through the demonstration of Yoshida 2012. [88]

1939 Ernst Ruska

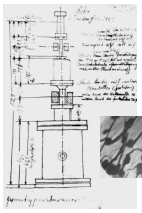

1940 M. von Ardenne and D. Beischer presented TEM micrograph of platinum oxide

1945 Turkevich one of earliest survey of the application of EM to the study of catalyst, RCA Research Laboratories at Princeton

1968 A. V. Crewe Pioneer work on STEM HAADF

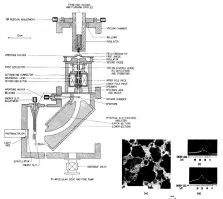

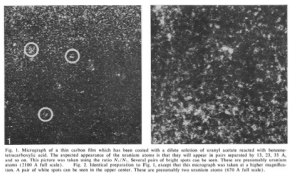

1970 Crewe work aberration corrected TEM

1971 earlier HRTEM image and HRTEM technique breakthrough

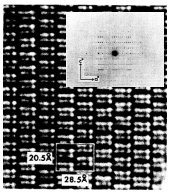

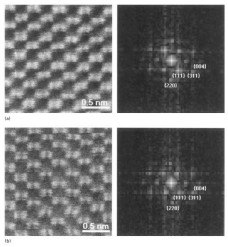

1999 imaging single atoms

2000 imaging Pt catalyst atom clusters

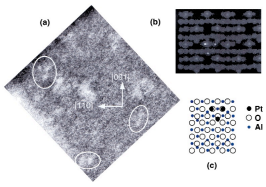

2002 HRTEM application, Rolison

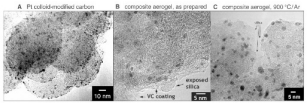

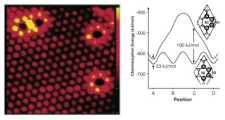

2003 HRTEM application, Bell

2004 EELS and plasmon energy mapping, Howe

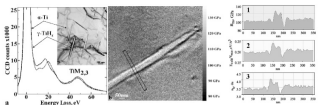

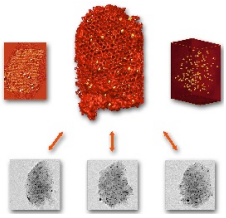

2004 Electron tomography application for heterogeneous catalysts, Ziese

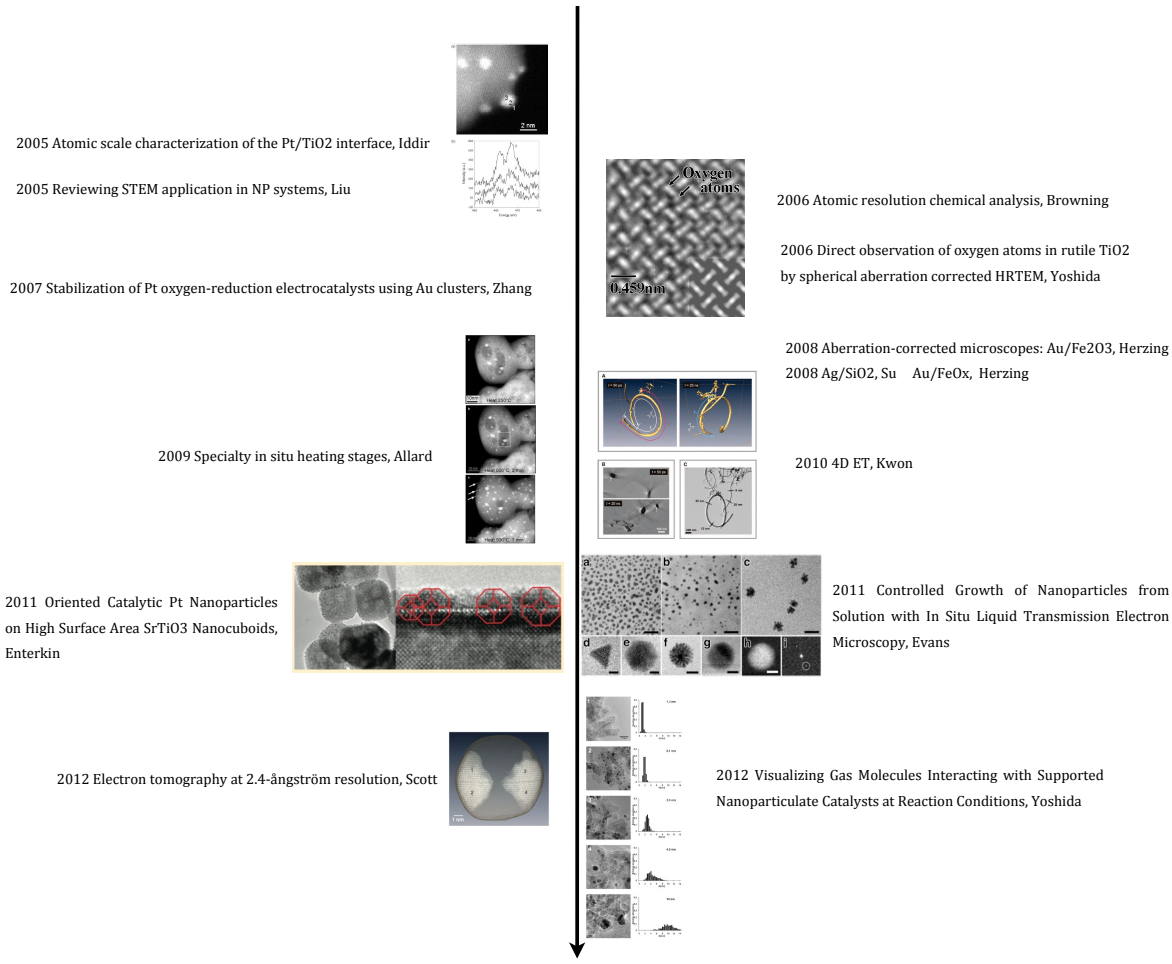

Figure 3-1 Timeline of the historical development of analytical electron microcopy techniques

Seeing through the historical development of the AEM techniques, the earlier work began with obtaining electron micrograph of the catalyst particles. Nowadays AEM has a wide range of applications, especially on catalysts related research works. These works demonstrate the capabilities of the AEM in the characterization of probing catalyst at atomic resolution, the determination of the chemical distributions, the observation of the local information in 3D and tracking the variation of the electronic structure and etc..

3.2 HR(S)TEM imaging

As shown in Figure 3-2, when a high-energy incident electron beam interacts with a sample, a lot of signals are emitted resulting from both elastically and inelastically scattering electrons, characteristic X-rays, secondary electrons and back-scattered electrons. All these signals can be used for structural and chemical characterizations of catalyst materials. [89]

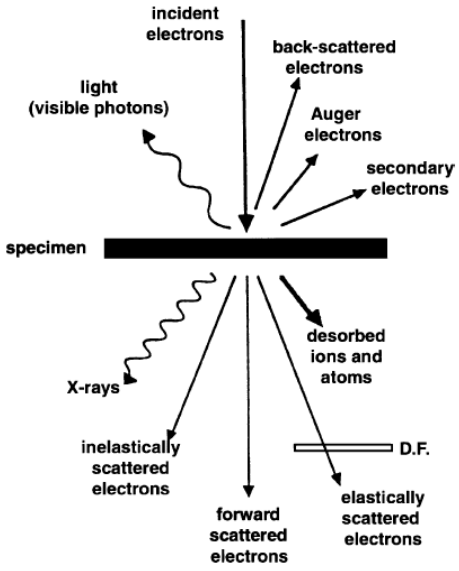

Figure 3-2 Schematic of the signals generated from elastically and inelastically scattered electrons during the electron beam–sample interactions

One of the most important capabilities of a TEM is electron diffraction. According to Bragg's law, crystals diffract electrons and the resulting diffraction pattern maybe regarded as the Fourier Transform (FT) of the real-space structure and it is found in the

back-focal plane of the objective lens. Therefore an inverse FT of the information in the back-focal plane of the objective lens forms the image. If only the diffracted beam corresponding to the incident electron beam direction is included in the objective aperture, a bright-field (BF) image is formed. The contrast of a BF image arises as a consequence of differences in electron intensities scattered into Bragg reflections from different areas of TEM sample. On the other hand, if the objective aperture only includes scattered electrons, a dark-field (DF) image is obtained.

The contrast of conventional BF and DF images is affected by the changes in specimen thickness, orientation or defocus due to the coherent nature of low-angle scattered electrons. However, high angle scattering is predominantly incoherent, and STEM images formed using a scanned focused probe, together with a high-angle annular dark field (HAADF) detector, do not suffer the contrast changes associated with coherent scattering. In simple terms, high angle scattering is brought about by the interaction of the electron beam with the atom nucleus, and are approximately proportional to the square of the atomic number, Z^2. This sensitivity to composition together with the incoherence of the scattering process enables small heavy particles to be highly visible within a matrix or support. [90]

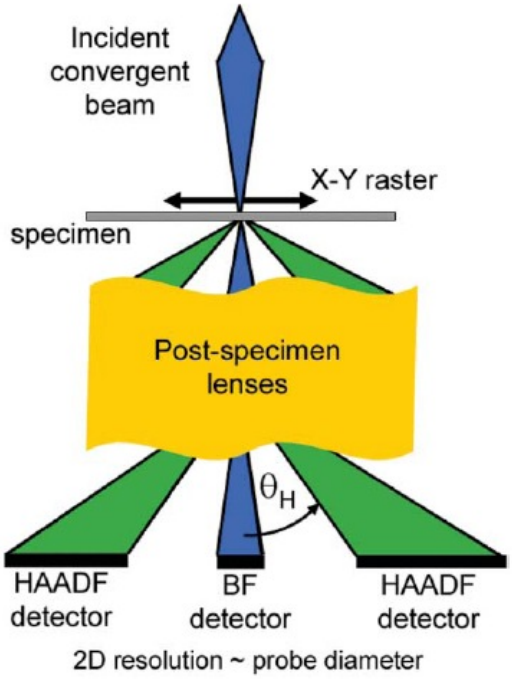

Figure 3-3 Schematic diagram of a scanning transmission electron microscope (STEM), showing the position of bright-field (BF) and high-angle annular dark-field (HAADF) detectors. As the probe is scanned across the specimen, the high collection angle (greater than 40 mrad) of the HAADF detector records a signal dominated by incoherent, thermal diffuse scattering. This intensity is insensitive to probe defocus, and the coherent Bragg (diffraction) contrast characteristic of conventional transmission electron microscopy . Image courtesy of Midgley [90]

3.2.1 High resolution TEM application in conventional Pt catalyst analysis

Most applications of electron microscopy to catalysis take advantage of high-resolution transmission TEM (HRTEM) instruments, which offer the direct structural analysis at atomic level. In HRTEM, the determination of chemical compositions of catalysts to the sub-nanometer level is achieved with energy dispersive X-ray

spectroscopy, which can be used for the investigations for both the surface and bulk structures of catalysts [89].

Furthermore, combined with digital image processing and simulation, quantitative analysis of HRTEM images can contribute to the understanding of performance-critical structural aspects of conventional fuel cell catalyst based on Pt materials (Figure 3-4).[91] For example, expansion of the lattice parameter,[91] unique shape of face-selective Pt catalysts, atomic structures of surface monatomic steps on industrial Pt nanoparticles, and evolution of the particle sizes (Figure 3-6), [92] can be resolved and tracked by HRTEM.

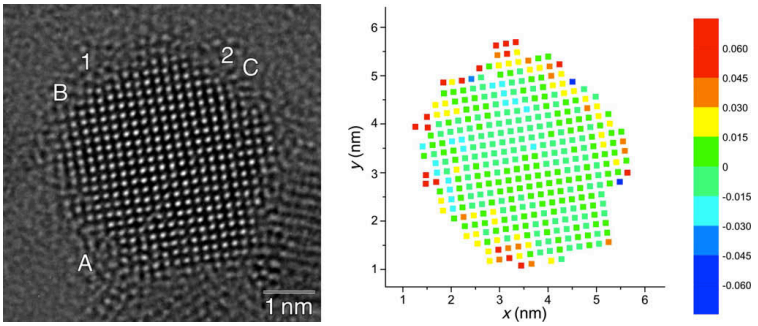

Figure 3-4 Experimental micrograph of the particle and map of the elastic strain component. Image courtesy of Du[91]

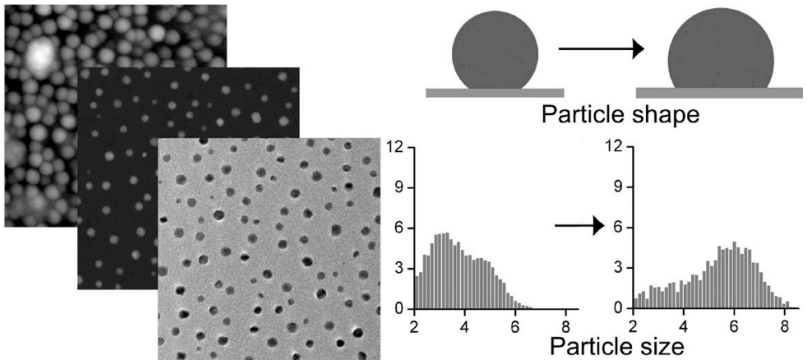

Figure 3-5 Size-dependent particle morphology is proposed as an explanation for the observed bimodal particle size distribution shape. Image courtesy of Jensen [92]

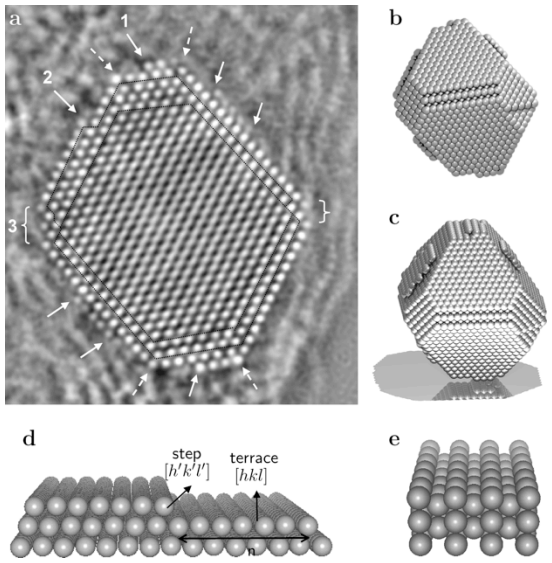

Figure 3-6 Surface defects on carbon supported Pt nanoparticles. The edges of nanoparticles can significantly alter the atomic positions of monatomic steps in their proximity, which can lead to substantial deviations in the catalytic properties compared with the extended surfaces. Image courtesy of Jensen [92]

3.2.2 HRTEM imaging of Bi-metallic catalyst

The field of multi metallic catalyst has become a central topic since 1950s when it was demonstrated that adding a second metal to Pt can significantly change catalytic properties of the nanoparticles as well as open the way for more advanced catalysts layers. In particular, the case of Pt is essential due to its highly active catalytic property in many important reactions related to fuel cells. Volcano plots shown in Figure 3-7 presented the electrocatalytic trends on pure metals as well as Pt_3M (M=Ni, Co, Fe, Ti, V) surfaces between the experimentally determined surface electronic structure (the d-band centre) and activity for oxygen-reduction reaction, where the maximum catalytic activity is governed by a balance between adsorption energies of reactive intermediates and surface coverage by spectator (blocking) species.[93] [94]

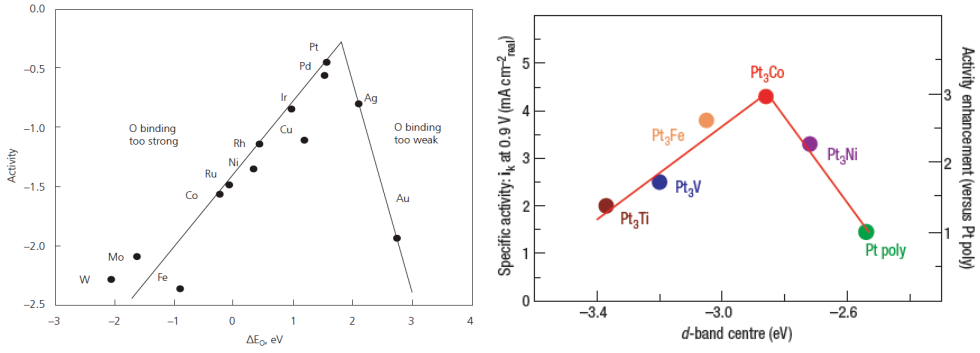

Figure 3-7 Trends of pure metals in oxygen reduction activity plotted as a function of the oxygen binding energy (left) and Trends on on Pt3M (M=Ni, Co, Fe, Ti, V) surfaces between the experimentally determined surface electronic structure (the d-band centre) and activity for oxygen-reduction reaction (right). Image courtesy of Norskov and Stamenkovic [93,94]

Using quantitative aberration corrected TEM, combined with other characterization methodologies, including EDX and XRD, alloy catalytic nanoparticles with reduced Pt loading can be investigated down to the atomic scale, furthermore atomic displacement can be measured and provide quantitative evidence of surface relaxation. Figure 3-8 and Figure 3-9 presented PtFe catalyst with reduced usage of Pt, one of promising cost-effective fuel cell catalysts comparing with commercial Pt catalyst. HAADF observations indicated that the nanoparticle possess platinum rich surface and iron ordering starts 2 to 3 atomic layers below it. The observed structure is expected to lead to the optimization of platinum usage and active surface sites. Furthermore, there were research reports proposing that Pt enriched surface on top of an alloy structure will be beneficial to ORR activity. [95] Quantitative measurements presented in Figure 3-9, where the variation of the interatomic distances suggested majority of the atoms expanded at surface layers whereas a few atomic columns are compressed inwards, leading to high possibility of impact on catalytic activity. [95] Individual atoms, 3D structure of bimetallic nanoclusters and changes in the positions of metal atoms in sequential images can also be resolved and identified using high resolution scanning transmission electron microscopy (Z-contrast), as shown in Figure 3-10 leading to the development of new and improved catalysts and other functional nanostructures [96]

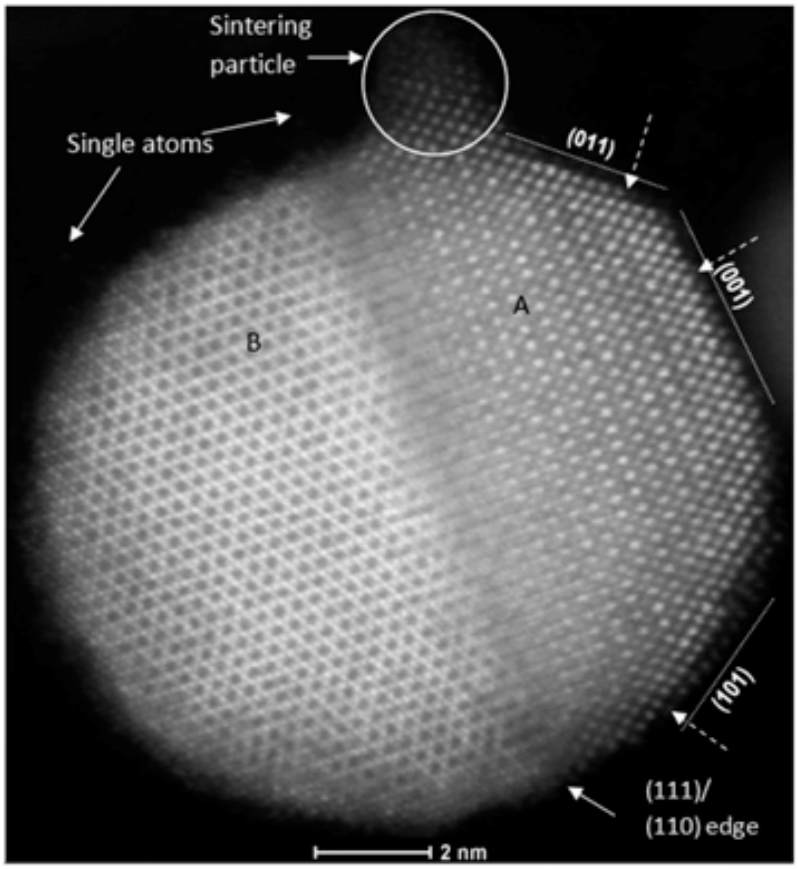
Sintering
particle
Single atoms
(011)
(001)
A
B
(101)
(111)/
(110) edge
2 nm

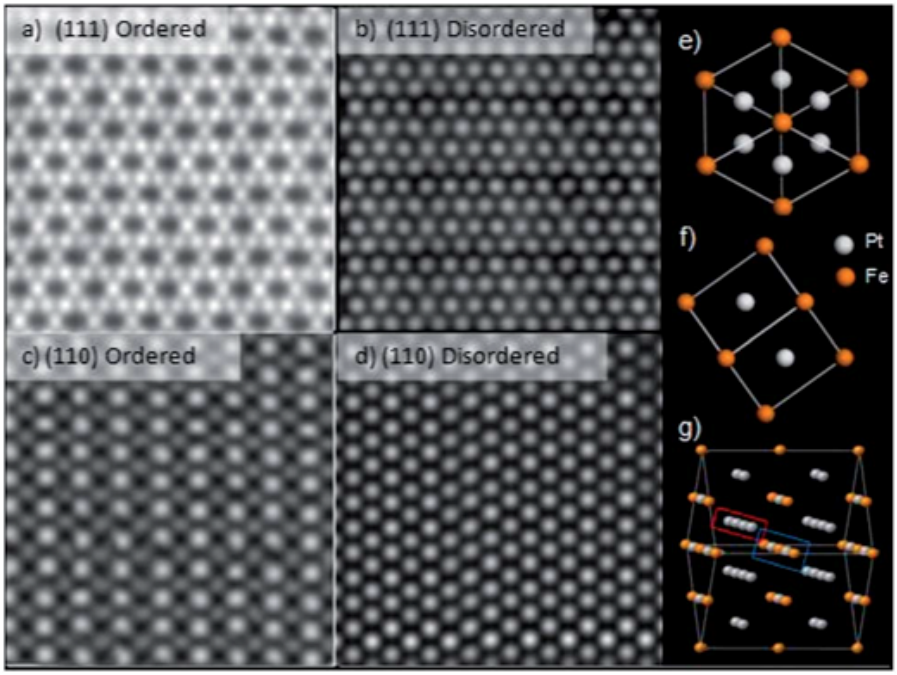

Figure 3-8 STEM HAADF image, multi-slice simulation and crystal models, image courtesy of Chan[1]

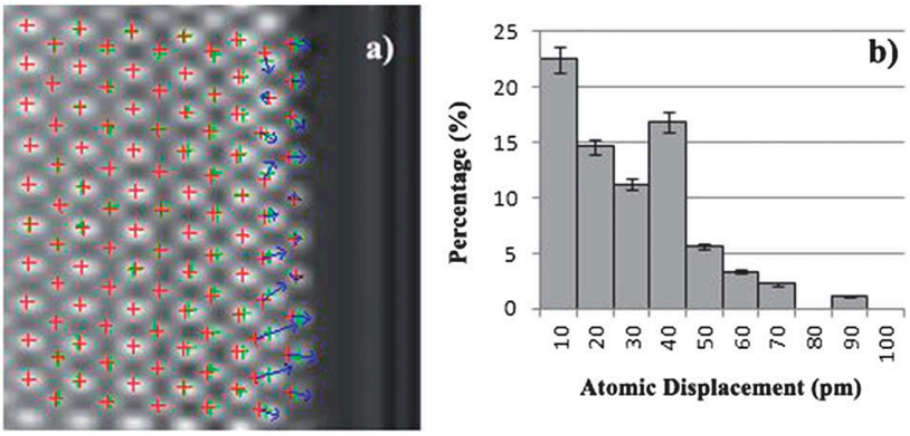

Figure 3-9 Atomic displacement calculations of the Pt3Fe surface, green and red crosses are the atomic local maximum and the extrapolated references respectively, image courtesy of Chan [95]

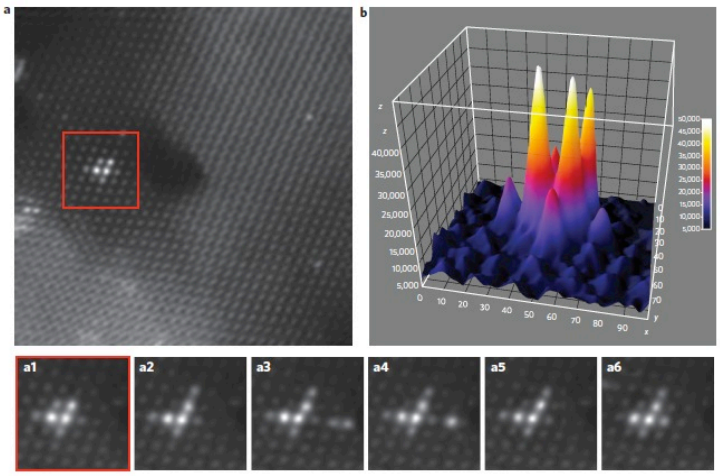

Figure 3-10 Sequentially taken STEM Z-contrast images and intensity surface plot of a rhodium–iridium cluster, image courtesy of Ortalan [96]

3.3 EELS/EDXS

HRTEM and HAADF STEM imaging provide the necessary the morphological information of the catalyst nanoparticles, such as energy favorable facets, strain, the combination of these approaches with Electron Energy Loss Spectroscopy and Energy Dispersive X-ray Spectroscopy (EELS and EDXS) provides further chemical information on the chemical nature of the samples and ultimately any possible interaction between the catalysts and supports.

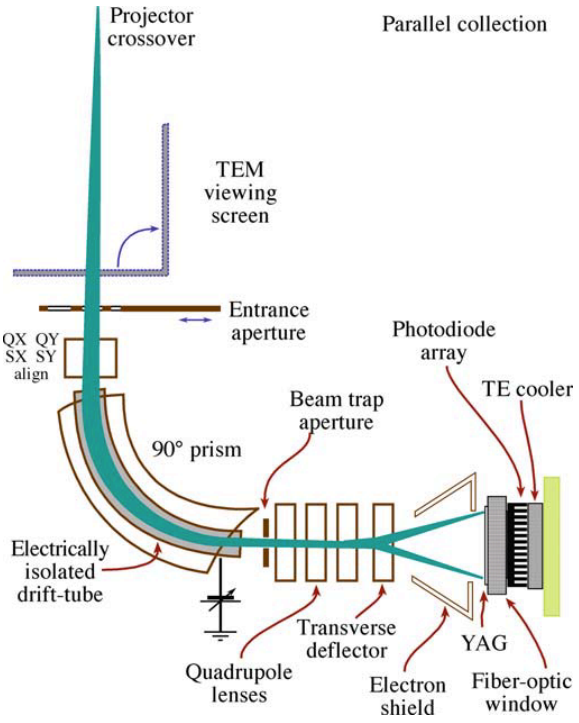

Figure 3-11 Schematic Diagram of the collection of EELS spectrum, image courtesy of Williams and Carter [97]

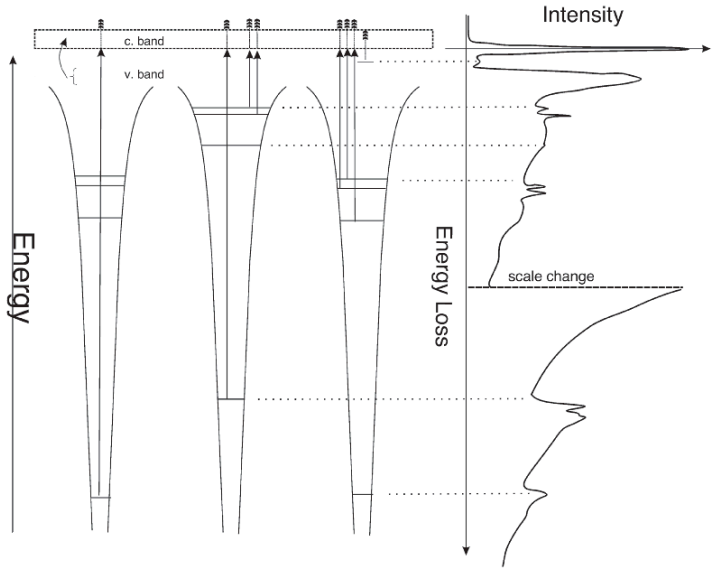

Figure 3-12 Schematic diagram of EELS spectrum, image courtesy of Hawkes [98]

The signal in EELS is obtained when a high-energy electron beam (100 to 1000keV) passes through a thin film with the thickness of 10 to 100nm, and the energy distribution of the transmitted electrons is recorded with an energy analyser. The spectrum generated from the sample under analysis contains two types of signals (Figure 3-12). First and most useful for the chemical analysis are the core ionization edges that allow the identification of the atoms that are ionized and, through the edge fine structure shape, the chemical state information on the valence and coordination. Second, at lower energy losses (0-100eV) valence band spectra may be also obtained, presenting useful information regarding local dielectric response of the solid. Typical conventional TEM/EELS systems possess, at best, an energy resolution of 0.6eV even with a field emission gun (Schottky emitter). Such energy resolution limits the amount of information that can be obtained from the fine structure of the ionization edges. With the recent developments and introduction of commercial (S)TEM/EELS microscopes equipped with monochromators, significant improvements in energy resolution were made and a resolution of about 0.2eV was typically obtained, leading to more opportunities for understanding the fine structure.[99]

While HRSTEM is widely applied to reveal the morphology profiles of complex structures of the catalyst support, EELS analyses provide the possibility to confirm changes in the oxidation state of atoms, such as the change in the valence of ceria in the vicinity of Pt nanoparticles that are present at different depth in the valleys.[100] EELS

maps provide useful information to deduce the elemental distribution in a thin film of complex oxides at the unit cell level and the changes in the near-edge structure within the inequivalent regions in the crystalline unit cell.[101] Valence state and site geometry of Ti L3, 2 and O K of different phases of Ti_xO_y can also be probed by using EELS.[102]

For example, the combination of Z contrast imaging and EELS, has been used to reveal the variations of catalyst particles (Pt) and their tendency to nucleate on the certain phases, indicate that the selective growth of Pt on rutile must be controlled by the lower formation energy on rutile because of the strong tendency to nucleate on the rutile phase of TiO_2 rather than on anatase. [43] Evidence of a strong interaction between the Pt particles and the support is found to be dependent on the Pt cluster size, being manifested either as an encapsulation of the Pt particles by the support or a distortion of the structure of the Pt particles. [44]

With development of EELS spectrum imaging in STEM, this technique can be used to map, at the atomic level, the composition of atomic columns and the valence of atoms at defects, interfaces, and surfaces. Recent applications of this technique are provided as examples showing the potential of the method for materials research. [103] For beam sensitive catalyst nanoparticles, Braidy's work demonstrated the design of analytical TEM measurements of beam-sensitive nanoparticles, probing composition variation/evolution, especially at relatively lower accelerating voltage. [104,105] In-situ heating experiments along

with EELS spectrum imaging offer a promising way to investigate the dynamic redispersion of elements during a catalyst's calcination and reduction, and characterize the occurrence of SMSI at the nano-scale. [106]

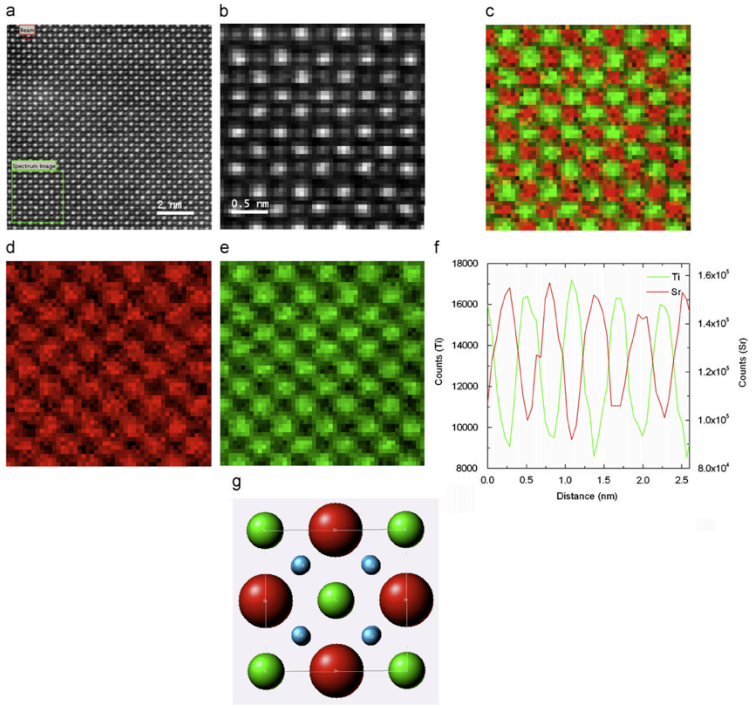

Figure 3-13 Elemental mapping at atomic scale using AEM approach combing spectrum imaging technique, image courtesy of Botton [105]

3.4 Tomography

Metallic nanoparticles or bi-metallic catalysts are currently of great interest, not only because of their high performance in a variety of energy conversion processes, but also

because of their structural and electronic properties. It is desirable to develop tomographic techniques in order to obtain more information of the complex structure of the catalyst. In nanotomography, projections of the object are recorded from different directions and then merged into a three-dimensional reconstruction, which is also called tomogram. Nowadays, the most useful modes for nanotomography are HAADF STEM tomography.

In general, many catalyts consist of heavy (high-Z) atoms such as platinum, palladium or alloys and bimetallic variants of these elements, supported on relatively low-Z, high-area solids such as carbon, silica and some of the transition metal oxides or carbides. The small heavy catalyst particles are highly visible within the support material by applying the technique of high-angle annular dark-field HAADF STEM imaging. Furthermore, atomic spatial resolution and precise composition of individual particles are attainable in modern aberration-corrected and monochromated STEM instruments for HAADF STEM tomography. [107] [108]

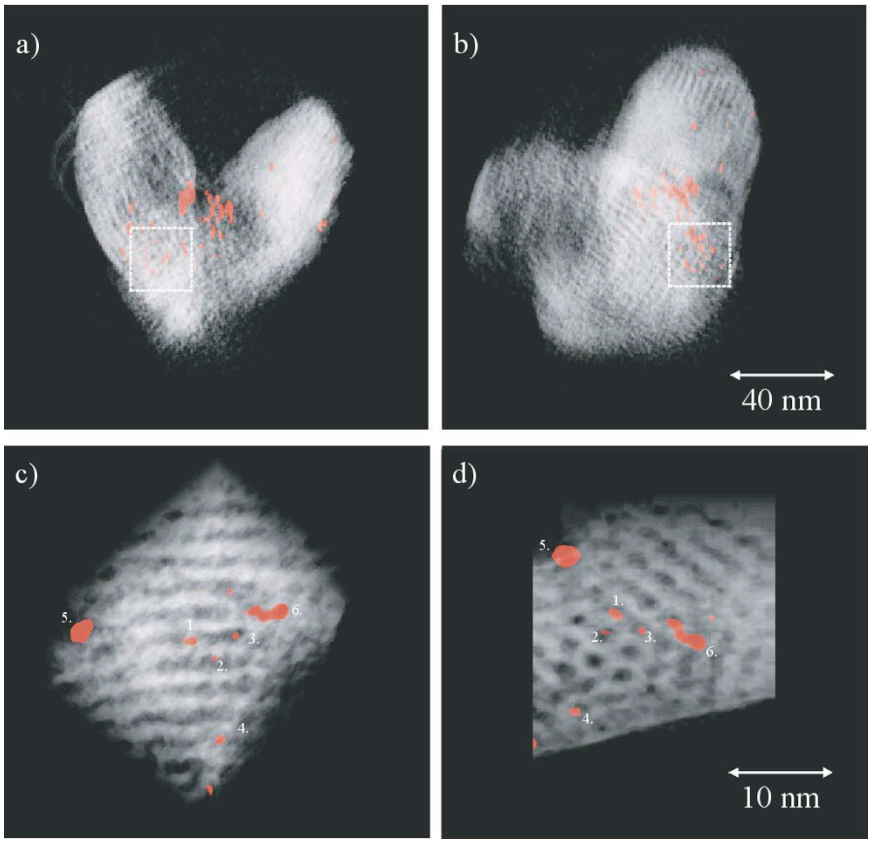

Figure 3-14 Voxel projection of a tomographic reconstruction of a heterogeneous catalyst composed of Pt/Ru nanoparticles (red) within an MCM-41 mesoporous silica (white), image courtesy of Weyland [108]

The reactivity of the catalyst is highly dependent on the active surface areas; the most efficient catalyst often possessed the most complex morphology. Rough surface, pores and regular channels are all common approaches to increase the active surface area.[108-111] Such dense and packed structure make the characterization challenging for conventional TEM since the 2-dimensional projections cannot fully resolve the true structure of the catalysts.[89] As a result, electron tomography providing 3-dimensional morphological

information has been developed in order to fully present the detailed structure of the materials under investigation. In order to reduce the effects due to the non-monotonic intensity variation of images with orientation of the sample and radiation damage inherent with conventional bright-field tomography, the HAADF STEM tomography technique was developed and applied for acquisition of the tomogram. This is due to the fact that the HAADF STEM signal varies monotonically with atomic number and specimen thickness and is also independent of diffraction effects which give rise to the strong variations of scattering intensity when the sample is close to Bragg diffraction conditions. Nanotomography is widely used in the fields of chemical, biological and materials sciences, especially nowadays. This technique has become an essential tool for probing 3D structure of heterogeneous catalysts at the nanometer scale. [64,112,113]

3.4.1 Development of Electron Tomography

An excellent example of the use of nanotomography in catalysis is shown in Figure 3-15. The center panel of the top three images shows the surface-rendered visualization of the reconstructed density of an Au/SBA-15 model catalyst particle (~ 256 nm × 256 nm × 166 nm). 3D reconstructions like these can be utilized to determine the 3D shape, volume, connectivity and location of pores inside a support material. Moreover, the size and location of Au particles inside the material can be seen unambiguously (left: virtual cross-section—thickness 0.64 nm—through the reconstruction, right: surface rendering of gold particles—size 8 nm) and subjected to statistical evaluation. This kind of

information could not be gained from a single transmission electron micrograph only (due to overlap of structures in projection). The slices at the bottom display three of the 151 electron microscopy projection images that were used to calculate the volume. The two-sided arrows indicate the reversible process of projection and back projection. [77]

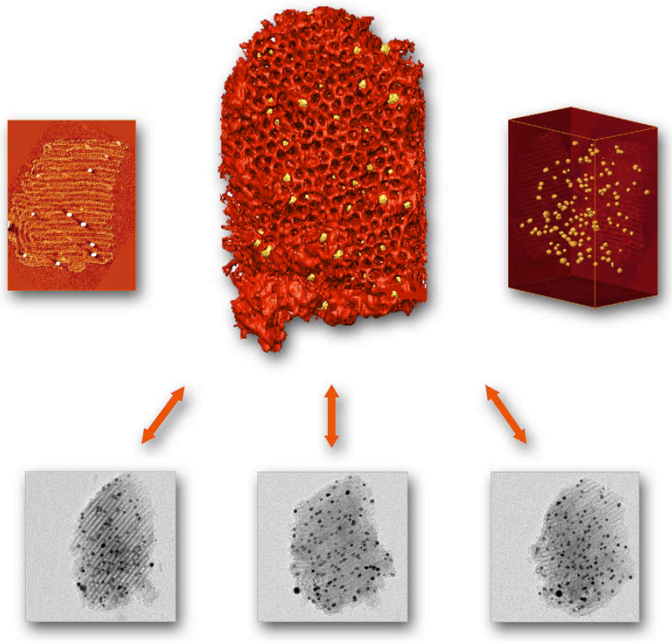

Figure 3-15 Electron Tomography reconstruction for Au/SBA-15 model catalyst particle, image courtesy of Ziese [77]

A strong advantage of electron tomography is that it enables the investigation of truly unique structures instead of averaging the information from the materials. Therefore, the technique allows the visualization of the distribution of active metal particles in the

catalysts in three dimensions. Moreover, it can be complementary to other macroscopic methods like nitrogen physisorption in order to investigate the relationship between microscopic structure and bulk characteristics (between form and function) of heterogeneous catalysts. The resolution of this method is affected by the level of signal to noise in the projection images (tilt series).

The resolution limits for electron tomography have been demonstrated in recent work.[114] By combining a novel projection alignment and tomographic reconstruction method with STEM, 3D structure of an approximately 10nm Au NP is probed at 2.4 Å resolution as shown in Figure 3-16.

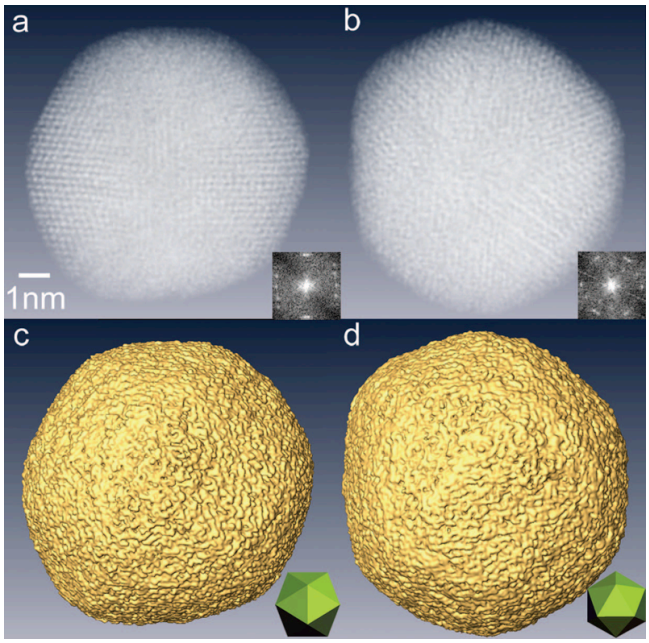

Figure 3-16 3D structure of the reconstructed gold nanoparticle, image courtesy of Scott [114]

3.4.2 The projection requirement

In general, projection requirement procedure is identified as usable image intensity, which has to be a monotonic function of a projected physical quantity for tomographic reconstruction to obtain structural information in three dimensions, especially for catalysts with complicated structure, for example, the mesoporous structures. In electron microscopy, only some of contrast mechanisms obey the projection requirement. For amorphous materials, such as many biological and polymer structures, the contrast in conventional bright-field (BF) TEM images arises from changes in specimen density or thickness and is suitable for tomography. For many crystalline materials, in general, there is no simple relationship between the image intensity and the physical properties of the specimen due to the strong Bragg scattering at particular orientations. [90,111]

3.4.3 Acquisition and Alignment

The quality of a tomographic reconstruction will improve as the number of images used increases. However, the number of images, which can be recorded in the electron microscope, is limited for two practical reasons. The first is that many samples will be beam sensitive and thus the extended exposure to the beam during the course of the tilt series acquisition will lead to sample damage. The second is that, unlike many other tomography methods, electron tomography is undertaken in an instrument with a highly restricted working space and in general it is impossible to tilt beyond a certain maximum angle, either because of the narrow pole-piece gap of the objective lens or because the

specimen (if slab-like in morphology) becomes too thick; for example, the projected thickness at 70° tilt is three times that at zero tilt. To overcome the restricted tilt range, one solution is to prepare a fine 'needle' or 'pillar' specimen and to tilt the specimen about its own axis which allows complete 360° tilt of the specimen without shadowing and without a significant increase in projected thickness. [108]

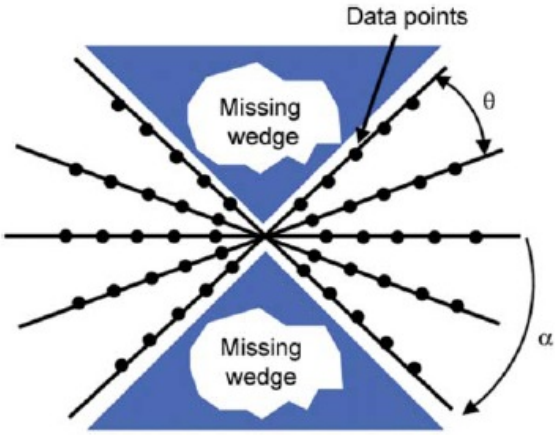

Figure 3-17 schematic plot in Fourier space, illustrating the extent of experimental data available after the acquisition of a series of images taken at a range of tilt angles, image courtesy of Weyland. [108]

3.4.4 Reconstruction

The key to high quality tomographic reconstructions is a very well-aligned data set. One of two approaches is normally used: (i) tracking fiducial markers and (ii) cross-correlation. The fiducial technique determines both spatial alignment and the direction of the tilt axis, plus any secondary distortions caused by optical effects. Cross-correlation alignment makes use of the information in the whole image (rather than a few selected

points in the fiducial technique) and makes no assumptions about the shape of the support film. It also avoids possible reconstruction problems associated with high contrast objects, such as colloidal gold, which can mask details in the reconstruction. However, cross-correlation alignment does not automatically determine the tilt axis direction and this has to be achieved independently.

Chapter 4. Catalysts with novel structures

4.1 Introduction

For a typical PEMFC, the hydrogen fuel (mainly comes from steam reforming of hydrocarbons) is oxidized at the anode catalyst layer to release electrons and protons, and oxygen (from air) is reduced at the cathode catalyst layer by accepting the incoming electrons and the protons from the anode to produce power through the external load, and at the same time to produce water and heat as well. As we have seen in the earlier chapters, the most practical catalysts in current PEMFC technology are Pt-based catalysts for both anode hydrogen oxidation reaction (HOR) and cathode oxygen reduction reaction (ORR). However, it is well known that reformed hydrogen contains significant amount of impurities such as CO and CO_2, which, in particular for CO, could be easily adsorbed on Pt particle surface and poison the anode catalyst layer, leading to significant fuel cell performance degradation even in the presence of as low as 25 ppm CO concentration. Such poisoning effect results from the attachment of a CO molecule onto the catalyst surface, thereby reducing the surface available for hydrogen reactions. Such strong binding has been explained by electron donation from the 5σ carbon monoxide orbital to metal, and subsequent transfer of two electrons from the d metal atomic orbital to the antibinding $2\pi^*$ CO orbital. This electron transfer is known as back-donation.

Therefore, developing novel anode catalysts with improved CO tolerance has been becoming one of the important tasks in PEM fuel cell development and commercialization. In recent years, bimetallic heterogeneous catalyst such as carbon-supported Pt–Ru alloy catalysts have been widely explored due to their improved CO tolerance capability. In particular, Pt-based core–shell structured catalysts with Ru as the core and Pt as the shell (Ru@Pt) show enhanced CO oxidation activity when compared to PtRu alloy and monometallic Pt and Ru nanoparticle catalysts. Recent studies revealed that preferential oxidation of the adsorbed CO on the Pt surface could be achieved through carbon-supported Ru@Pt catalysts, resulting in quick release of active sites occupied by CO, leading to an improved hydrogen oxidation reaction in the presence of CO in the fuel feed stream. [115]

In this chapter, we thus focus on reporting on two different systems. First of all on PtRu for improved CO tolerance, and then PtRu/mixed titanium oxides. After a summary of the synthesis procedures (section 4.2.1) and specific experimental details related to this work (section 4.2.2), I present the results of experimental characterization of the material and discussions on the relevance in terms of catalytic properties (section 4.3) followed by a general conclusion (section 4.4).

4.2 Experimental section

4.2.1 Synthesis of PtRu electrocatalyst

In order to synthesize Pt–Ru catalyst supported on carbon, Institute of Fuel Cell Innovation (IFCI) collaborators first reduced ruthenium (III) acetylacetonate (97% Ru(acac)3, Sigma–Aldrich) in tetra (ethylene glycol) solution (99% t-EG, Sigma–Aldrich) in a microwave oven. Platinum (II) chloride (≥99.99% PtCl2, Sigma–Aldrich) and carbon black (Vulcan-XC-72R) were then added into the solution while keeping constant stirring overnight for forming a slurry mixture, which was then further reduced in the microwave oven. In order to separate the catalyst particles from the solvent, treatment through high-speed centrifuge (Thermo Scientific Sorvall Legend RT+ Centrifuge, Sorvall) was applied, followed by ethanol rinse by several times to remove solvent residues on the catalyst particles. After dried in the oven overnight at 100 ◦C, the final product was ground in a mortar into powder for physical and electrochemical characterization.

For synthesizing Ti_4O_7 supported PtRu catalysts, IFCI scientists developed a two-step pyrolysis and microwave irradiation method. The first step was to co-reduce the mixture of ruthenium precursor and TiO_2 in a H_2 reducing atmosphere under heat-treatment, and the second step was to create a shell of platinum via the microwave irradiation.

4.2.2 Catalyst material characterization using instrument methods

The structure and phase analysis of PtRu/C catalysts obtained above were conducted via XRD (D8 ADVANCE X-ray diffractometer, Bruker Axs, Inc.) with Cu Ka1 radiation. The XRD pattern was recorded between 20° and 90° with a scan speed of 0.1 s/step and increment of 0.02° per step at current and voltage of 40 mA and 40 kV, respectively. The morphology and particle size of the catalyst were analyzed using a transmission electron microscope (Tecnai G2-F20 High-Resolution TEM), and the composition qualitative analysis was conducted by EDX (Link Isis System, Oxford, Hitachi S-3500N).

For a more detailed analysis of the catalyst structure and composition distribution over larger sample areas as well as for individual particle measurements, analytical measurements were conducted by EDX combined with STEM in an aberration corrected microscope (FEI Titan 80–300 cubed) equipped with a high-brightness electron source capable of achieving sub 0.1 nm probe size and a high-angle annular dark-field detector (HAADF) for "atomic number" contrast imaging. Quantitative analysis of the STEM HAADF images is obtained using the ImageJ software from NIST, including the identification of the local maxima of the atomic column and then further conduct the measurement of the lattice spacing deviation and the lattice strain.

The extended X-ray absorption fine structure (EXAFS) technique was also employed as a short-range probe of structure for PtRu/C catalyst, providing information on local correlations around the absorbing atom. In this respect, a series of EXAFS measurements of the synthesized samples were made using synchrotron radiation at room temperature. The measurements were made at the Pt L3 edge (11,564 eV) and the Ru K edge (22,117 eV) and analyzed simultaneously.

4.3 Results and discussions

In this section we report two sets of results and discussions related to novel catalysts for improved CO tolerance.

4.3.1 A novel CO-tolerant PtRu core–shell structured electrocatalyst with Ru rich in core and Pt rich in shell for HOR and its implication in PEMFC

In the current study, a detailed structural characterization is conducted using advanced analytical transmission electron microscopy together with a detailed elemental analysis. The synthesis of the Pt-Ru catalyst is achieved using microwave method, which is considered one of the effective approaches for easy and quick synthesis of catalysts with homogeneous particle size distribution.[14]

There has been work with our collaborators from Institute of Fuel Cell Innovation (IFCI), to investigate the CO tolerance of the in house-prepared 20-wt% PtRu/C catalyst. H_2 containing various CO concentrations (10, 50, 100, 300, and 500 ppm CO)

was applied as anode feed gas. As the concentration of CO is increased in the H_2 stream, the performance is decreased since more CO occupied the active sites on pure commercial Pt particles, leading to higher CO saturation coverage as well as increased overpotential which has to be overcome. However, when the in-house prepared PtRu/C catalyst is used, the overpotential is lower compared to that of both commercial Pt/C and PtRu catalysts in various CO concentrations at the same CO feed concentration, leading to higher CO tolerance, as shown in Table 4-1.

Table 4-1 Overpotentials obtained from commercial available catalyst and in-house developed catalyst for various CO concentrations

	CO concentration (ppm)				
	10	50	100	300	500
Overpotential (mV) vs. RHE					
Commercial Pt/C	51.9	91.1	479.1	824.6	879.5
Commercial PtRu/C	88.6	140.9	306.9	763.4	822.0
In-house developed PtRu/C	32.8	87.8	253.8	710.3	768.9

IFCI collaborators conducted XRD analysis over in-house developed PtRu/C catalyst and commercially available electrocatalysts to obtain the preliminary structure information. As shown in Figure 4-1, (a) and (b) respectively presents the XRD spectra of commercially available 20-wt% Pt and PtRu alloy supported on carbon, the diffractogram of in-house synthesized 20-wt% PtRu deposited on carbon by the microwave irradiation method is shown in Figure 4-1 (c). Standard (1 1 1), (2 0 0), (2 2 0), and (3 1 1)

reflections for pure Pt were observed from different samples including commercially available ones and in-house prepared PtRu catalyst, indicating single phase face-centered cubic (FCC) crystalline structure existed in these samples. Diffraction peaks of commercially available PtRu alloy catalyst are shifted to higher angle while comparing with pure Pt catalyst, indicating the lattice contraction due to the formation of alloying of Ru with Pt. However, without obvious peak shift, the diffraction peaks of the in-house synthesized PtRu/C catalysts show the same diffraction peak positions as those of commercially available Pt/C catalyst as shown in Figure 4-1 (C), indicating that in-housed prepared PtRu/C catalysts are not in the same alloy state as in commercially available PtRu alloy catalyst. Ru peaks were not identified due to the broadening effect. [115]

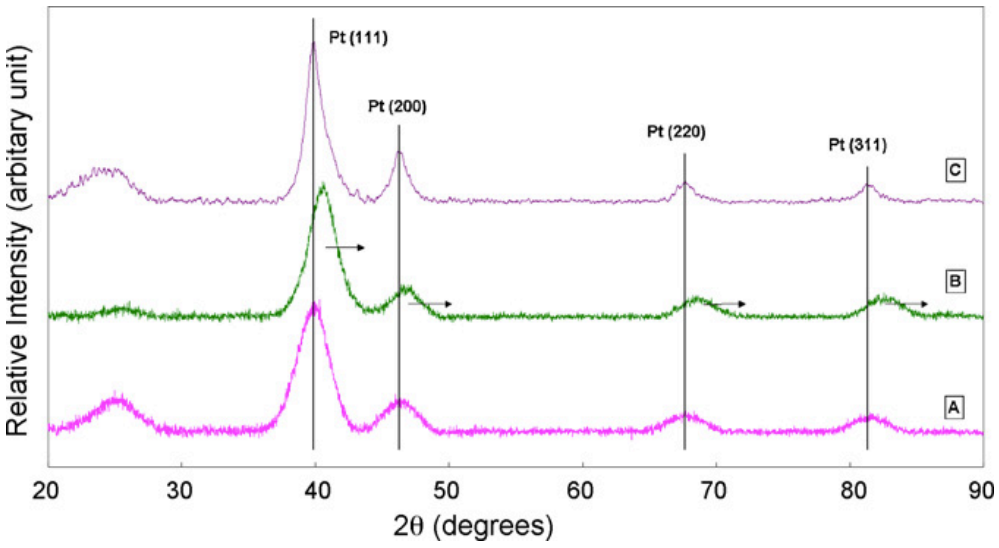

Figure 4-1 XRD analysis results over the samples of: (a) commercially available 20wt% Pt supported on carbon; (b) commercially available 20wt% PtRu supported on carbon; (c) in-house prepared PtRu supported on carbon. Image courtesy of Lei Zhang [115]

EXAFS analyses were also conducted by IFCI collaborators to obtain further insight on the local structure of the catalyst nanoparticles. Figure 4-2 presents the Fourier transform of the EXAFS oscillations of Pt L3-edge for the PtRu/C catalyst and corresponding Pt reference spectrum. The peak position of in-house prepared PtRu/C catalyst is located at a lower distance range than that of the pure Pt reference foil. These results indicate the possibility of Ru atom existing within the first coordination shell. In terms of Ru atoms environment, the Fourier transform of the EXAFS oscillations of PtRu/C showed a strong peak at ~2.4 Å (corresponds to single scattering by Ru–Ru atoms) with a shoulder at ~2.1 Å (assigned to single scattering by Ru-Pt), indicating some Ru atoms diffused into the Pt shell, and vice versa.

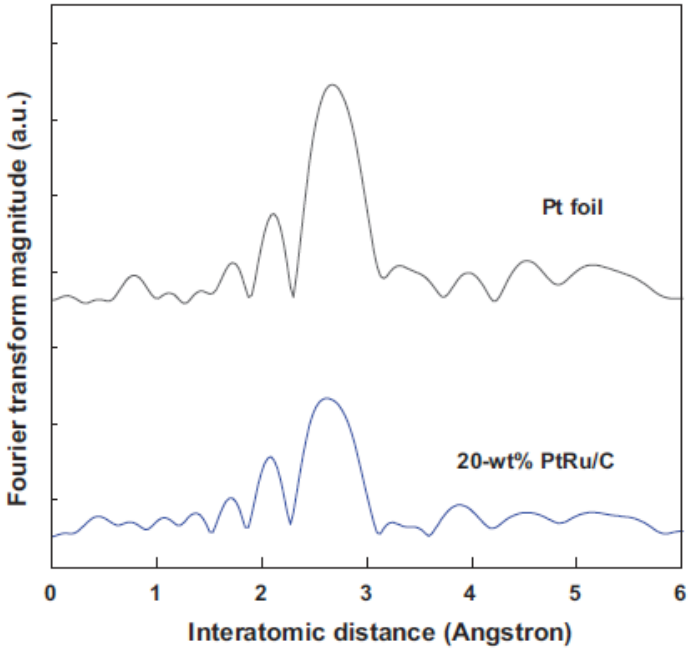

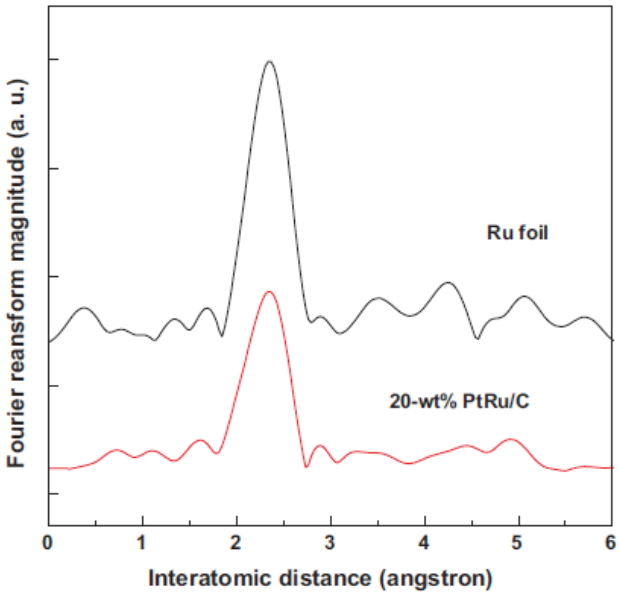

Figure 4-2 Fourier Transforms of EXAFS of PtRu/C catalyst and corresponding reference spectra (top: Pt reference, Bottom: Ru reference). Image courtesy of Lei Zhang [115]

To further characterize these nanostructures, STEM HAADF imaging and EDX mapping over individual particle as well as larger sample area were carried out in order to probe the local composition variation within catalyst particles. As shown in Figure 4-3, STEM HAADF characterization along with EDX elemental analysis is conducted over the PtRu supported on carbon black sample. It was found that catalyst nanoparticles produced through the microwave synthesis process exhibit a structure where the Pt and Ru concentration varies within the particle. HAADF images (Figure 4-3B) show that the shell is generally brighter than the core, suggesting higher atomic number atoms are located on the shell of the nanoparticles. EDXS mapping was also performed over individual nanoparticles. Elemental analysis results also indicate that Pt and Ru distribution varies from shell to core.

Results shown in Figure 4-3C indicate the variation of Ru and Pt from shell to the core area with a Ru L peak stronger in the centre, relative to the Pt L peak. Furthermore, for a typical PtRu nanoparticle supported on carbon, it appears clearly that Ru is mainly distributed in the core area, while Pt distributed in both areas but with higher concentration in the shell.

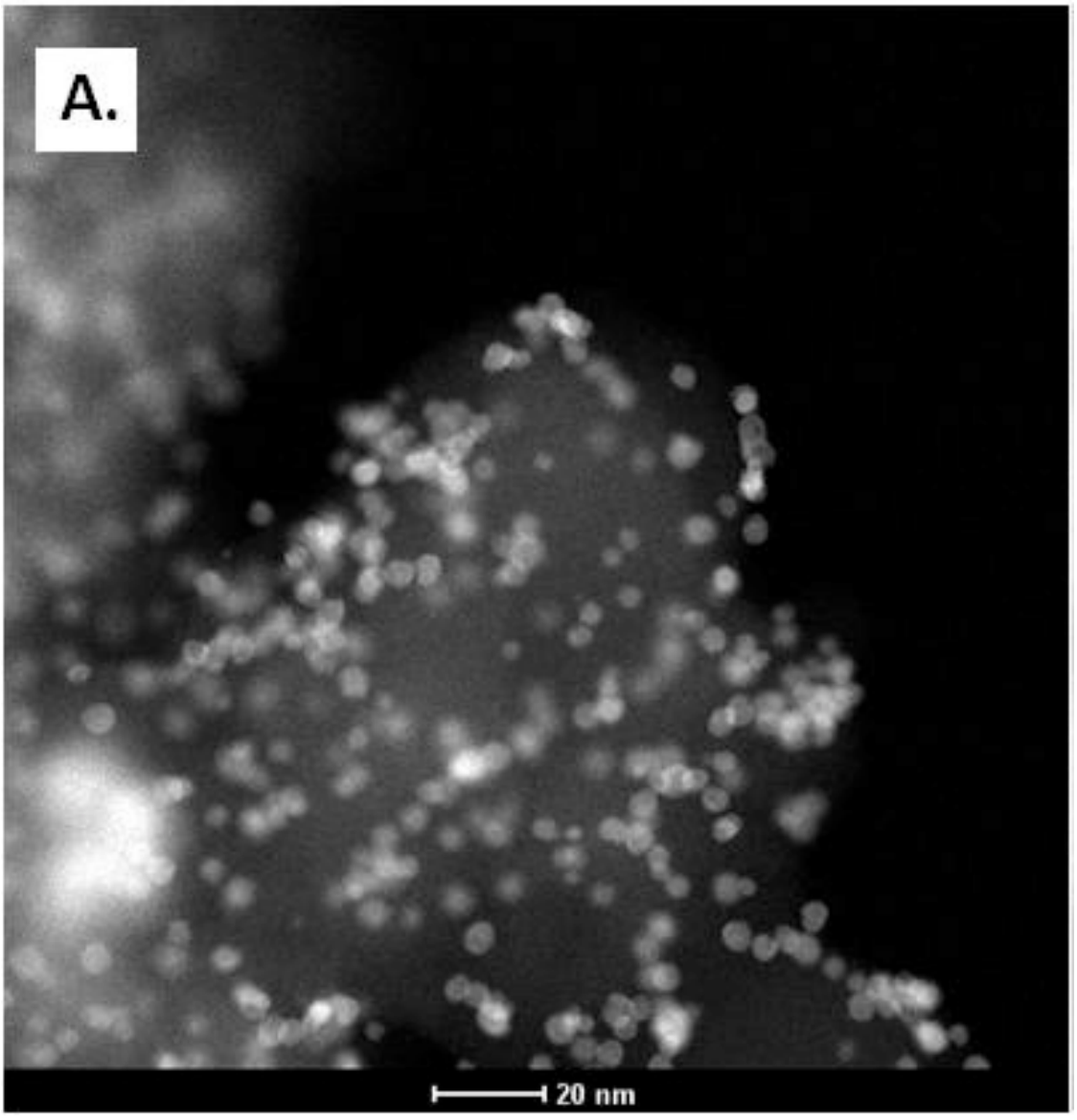
A.
20 nm

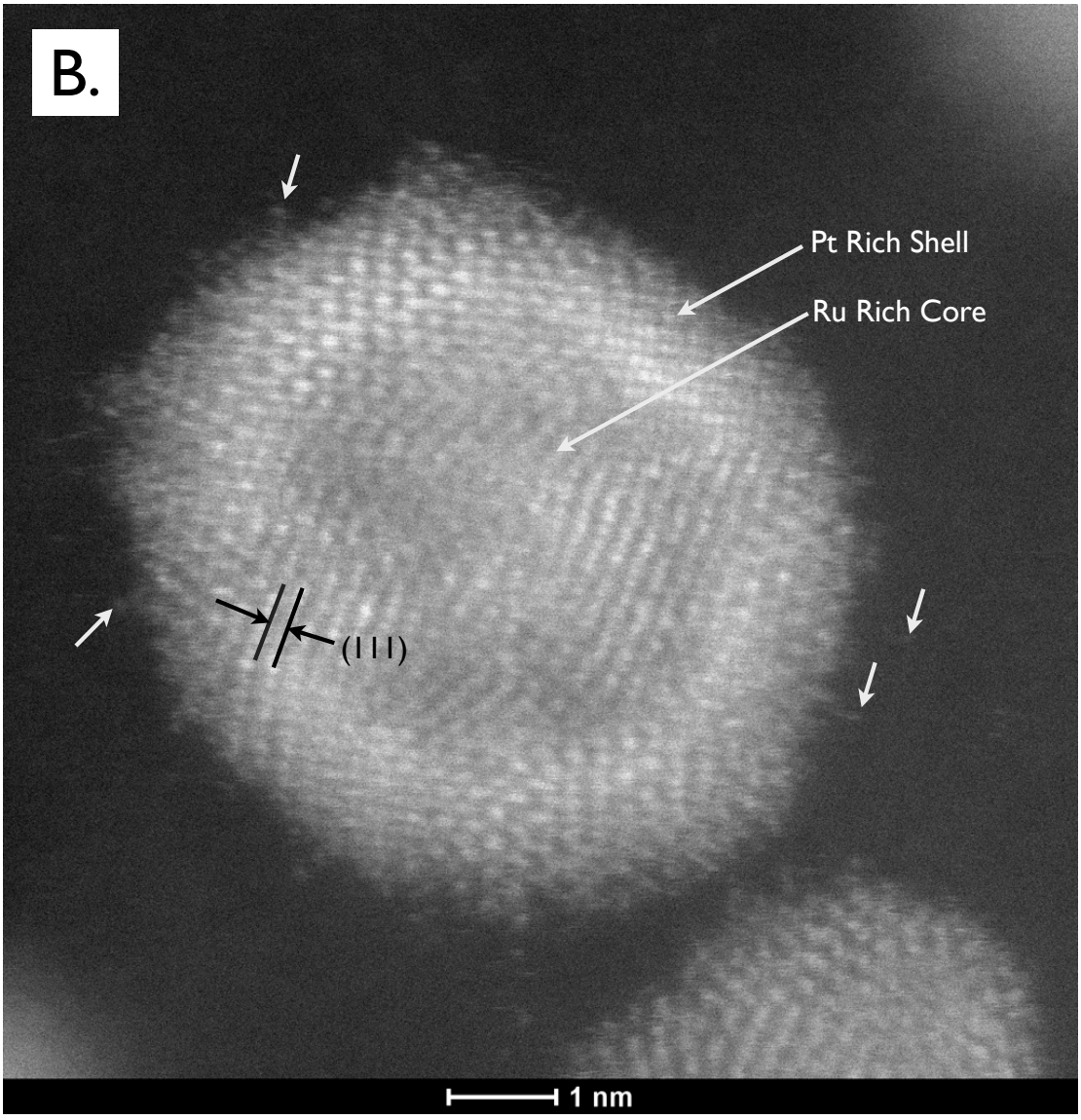
B.
Pt Rich Shell
Ru Rich Core
(111)
1 nm

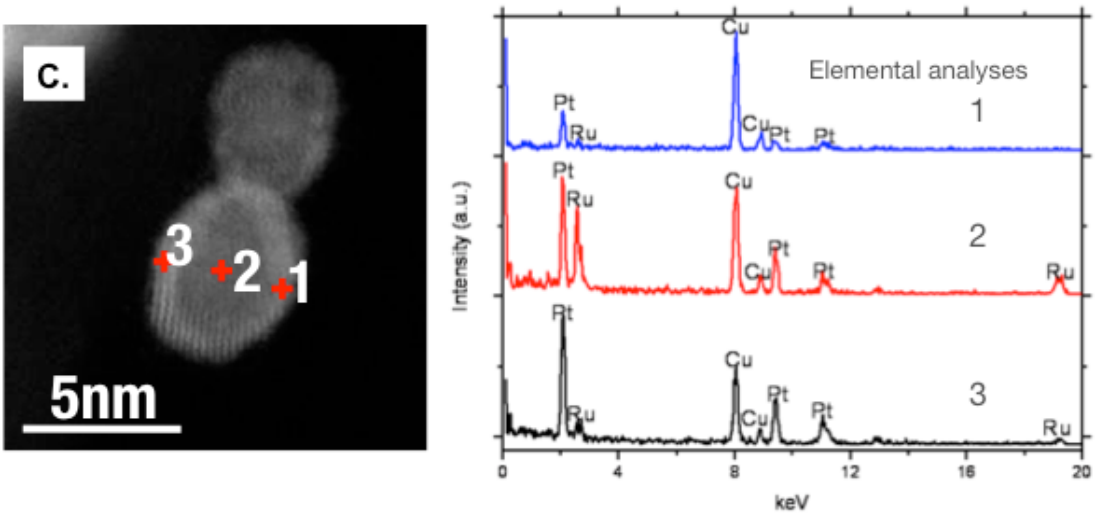

Figure 4-3 Above figures show STEM HAADF (A and B) as well as EDX results (C) which were taken from the sample of RuPt supported by carbon. Characterization results indicate catalyst nanoparticles with core-shell structure were successfully synthesized. According to the elemental analysis results, it is also obvious that the Pt/Ru ratio varies from shell to core ad the Ru peak is stronger in the core (area 2) than the shell (area 1, 3).

EDX mapping was also performed over individual nanoparticles with the maps shown in Figure 4-4 and Figure 4-5 indicating the relative distribution of Ru and Pt from shell to the core area even if the maps are relatively noisy since the extent of the distribution of intensities in the Pt map is larger than the distribution of Ru. For a typical RuPt nanoparticle supported on carbon, it therefore appears that Ru is mainly distributed in the core area, while Pt distributed in both areas but with higher fraction in the shell, which is consistent with nanoparticles has a Pt-rich. Since the electrons in the sample are transmitted through the sample, scattering through the top and bottom surfaces as well as

the core of the particle when the electron beam is placed in the center of the particle, Pt signal from the top and bottom surfaces is also detected.

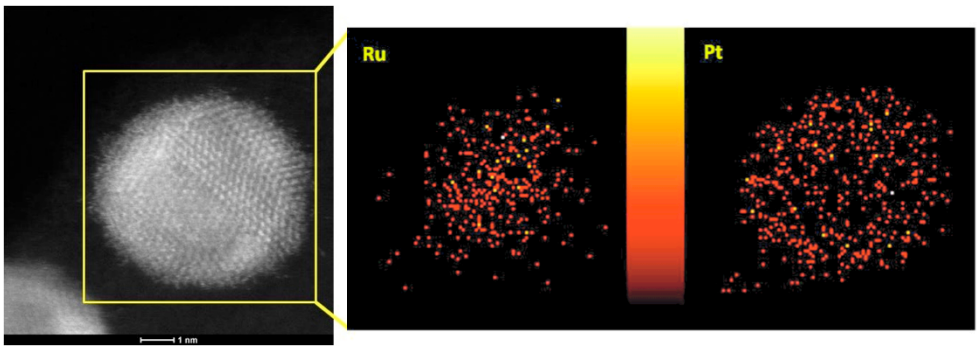

Figure 4-4 EDX mapping over typical RuPt nanoparticle, Ru is mainly distributed in the core area, while Pt distributed in both areas but with higher ratio in the shell,

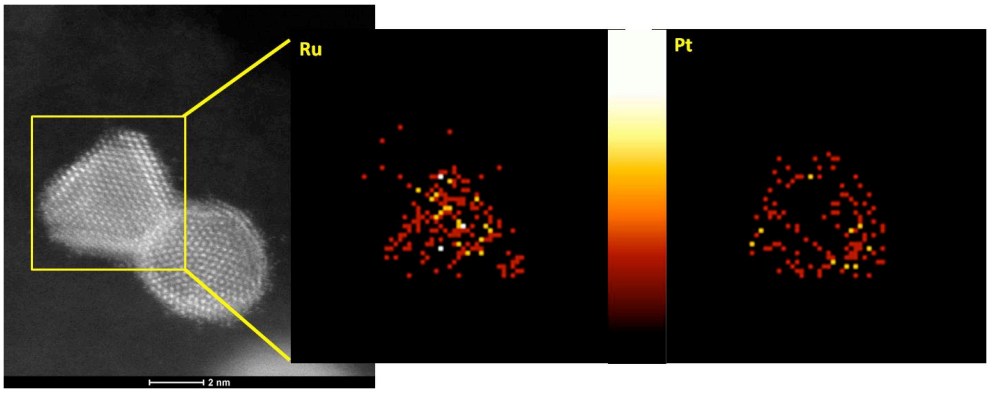

Figure 4-5 EDX mapping over the RuPt nanoparticle with triangle shape (possibly because viewing at different direction)

EDXS mapping and HAADF imaging results presents a very clear evidence that nanoparticle with a Ru rich core and Pt rich shell were successfully obtained from the synthesis route. STEM HAADF observation and EDXS point analysis and mapping is

consistent with EXAFS results above and provides further evidence in terms of elemental distribution within the nanoparticle catalyst. EXAFS indicates the possibility of the decrease of the interatomic distance change of Pt-Pt comparing with pure Pt reference, STEM HAADF observation not only further confirmed the estimation from earlier EXAFS results, but also identify the direction and location. EDX results provides further evidence that, the shell is not pure Pt shell but Pt rich, which indicates the possibility of PtRu formation within the shell which might be the cause of decreasing of the interatomic distance. As a result, we can see that PtRu/C catalysts in the current study have a structure of a Ru-rich core and a Pt-rich shell. From the Ru@Pt nanoparticle center to its surface, the Pt density is gradually increased and the Ru density is gradually decreased. This is the major difference of this PtRu/C core–shell structured nanoparticle from that of traditional Ru–Pt core shell structure, where the core is fully consisting of Ru, and the shell is composed of 1–2 monolayers of Pt. Furthermore, measurement of the interatomic spacing indicate that there is compressive strain existing within the shell of the particle along <111> direction, the measured spacing is 2.14Å, comparing that of 2.265Å (111) of the pure Platinum bulk samples (Wyckoff , Crystal Structures (1963), 1, 7).

We can understand the relevance of these observations in terms of catalytic activity and the increase CO tolerance. Zhang et al, suggested that, since the Ru metal is confined inside a Pt shell, the conventional bi-functional mechanism (where both alloy

components are present on the surface) may not be applied to explain this increased CO removal. [115] We have therefore to use different theory to identify the mechanism in the current Ru@Pt catalyst system. Using Density Functional Theory-DFT, Alayoglu [116] proposed that in common bimetallic catalysts systems, both alloy components are present on the surface, the more oxophilic metal acts as an oxygen activator to form surface OH, which facilitates the oxidation of the CO adsorbed on neighbouring, less oxophilic metal centres. In contrast, Pt monolayers on base metals or bimetallics, known as near-surface alloys (NSAs), possess the high activity of pure Pt for H_2 activation kinetics, whereas at the same bind adsorbates (for example, CO) much weaker than pure Pt. Furthermore, the core–shell architecture observed in the current study where only one type of atom is mainly present on the surface, and thus involves a combination of 'ligand' and surface strain effects. We have also observed a compression of the PtPt bond distances. Based on Strasser's study, it was also suggested that the compression in the shell modifies the d-band structure of the Pt atoms, and thereby weakens the adsorption energy of reactive intermediates compared to unstrained Pt and results in an increase in the catalytic reactivity. [117]

4.3.2 Ti_4O_7 supported Ru@Pt core-shell catalyst for CO-tolerance in PEM fuel cell hydrogen oxidation reaction

In parallel to the CO-tolerance research as presented earlier in this chapter, great efforts have been also made in recent years with respect to the development of non-carbon supported Pt and Pt alloy catalysts. It is well known that corrosion and collapse of the conventional carbon support leads to particle agglomeration, resulting further degradation of the catalyst and negative impact of the fuel cell performance.

Therefore, further and continuous work based on previous study on Ru@Pt/C core–shell catalyst is conducted, exploring the variation of CO-tolerance by using novel oxide supported Ru@Pt core–shell catalyst. Experimental work on synthesis and electrochemical data shown that these materials exhibit improved CO tolerance comparing with carbon supported Ru@Pt catalyst. [118] Here, our goal is to study the detailed structure with advanced analytical electron microscopy to probe atomic-scale information in terms of particle size, elemental distribution and electronic structure, which significantly affects the catalytic activity of the catalyst layer.

The overview of the sample at relative low magnification in STEM HAADF mode are shown in Figure 4-6 A and B. Based on the atomic contrast of the HAADF mode and thickness variations, we show that catalyst nanoparticles are uniformly distributed on the surface of the support. The particle size distribution is shown in Figure 4-6 C after

measuring over 200 particles. The average size of the catalyst nanoparticle is around 5.1 nm, over 35% of the catalyst is ranging from 3nm to 4nm, which is close to average size of about 3.5nm for commercial ETEK Pt/C.

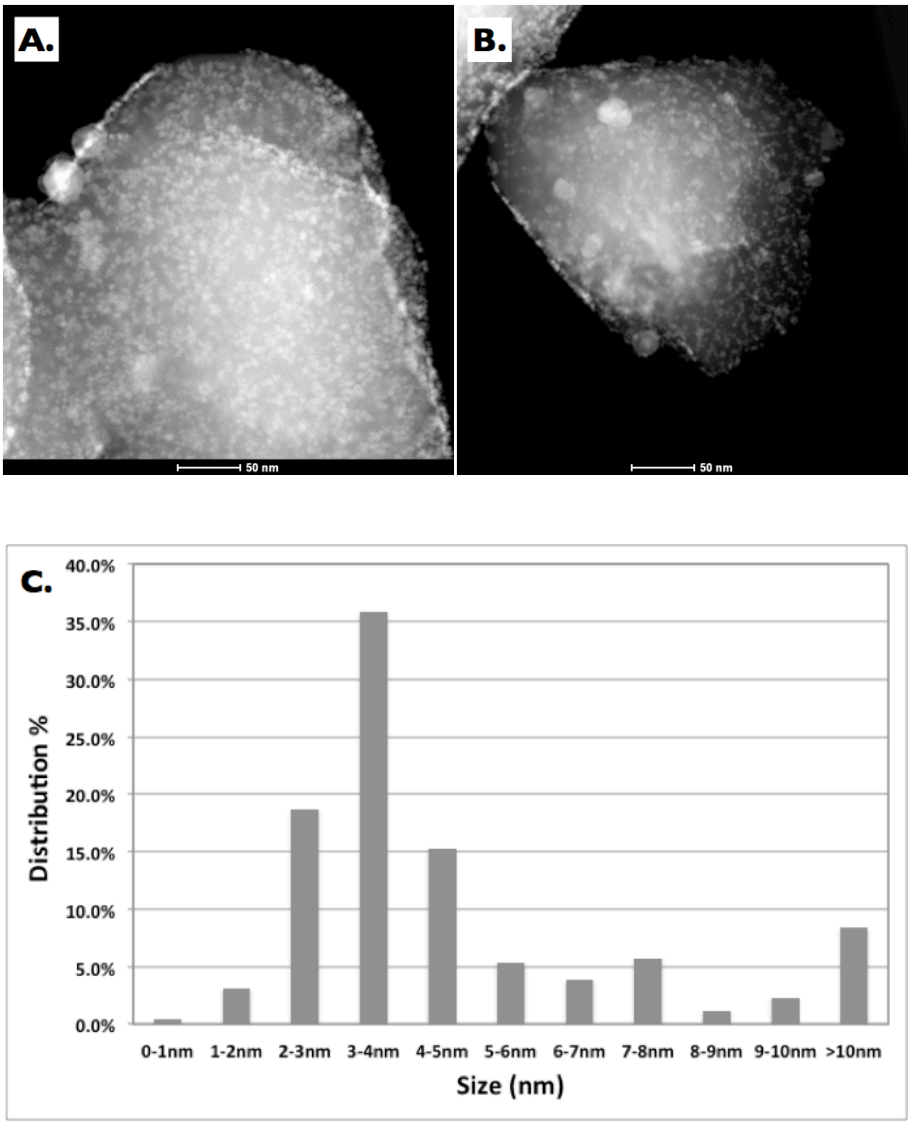

Figure 4-6 A) and B): overviews of different areas from the sample in STEM HAADF mode (atomic number Z sensitive); C): catalyst nanoparticle size distribution

Elemental analysis was performed over the sample by using EDX measurement. EDX spectra of the corresponding areas (highlighted in 1 and 2 in Figure 4-7A) are shown in Figure 4-7 B, respectively, spectrum 1 and 2. It is observed that Ti, O, Pt, and Ru were detected from the sample. Cu signal is from the TEM grid.

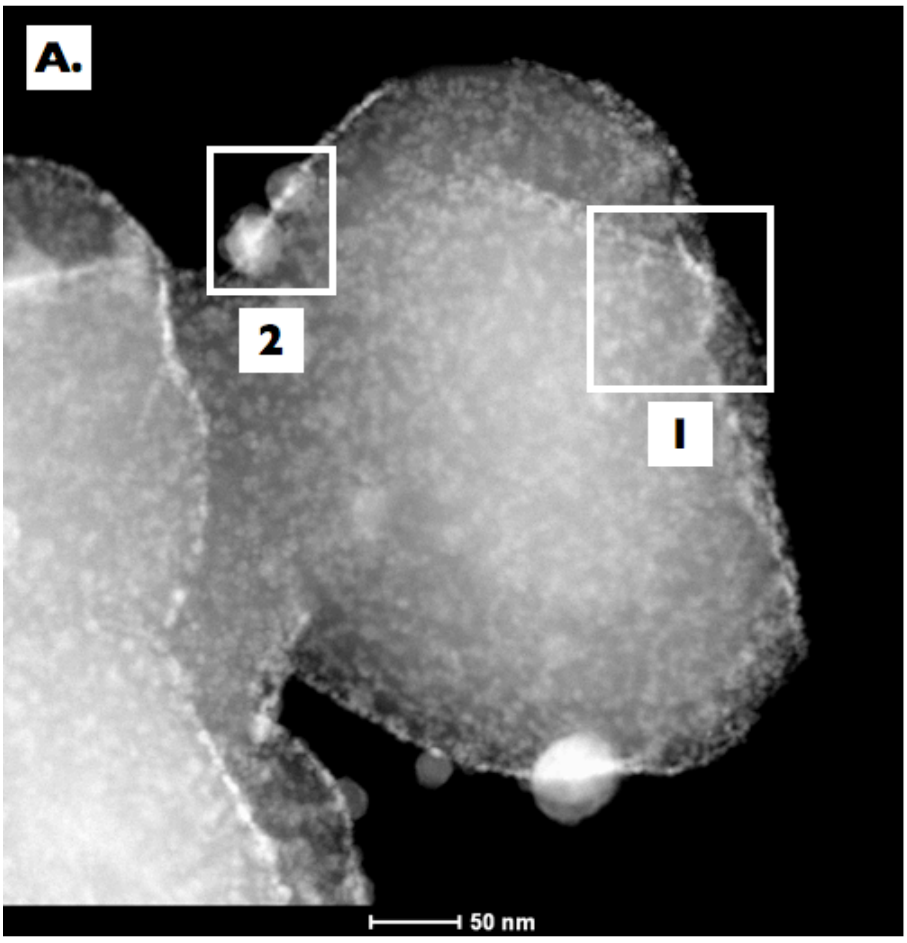

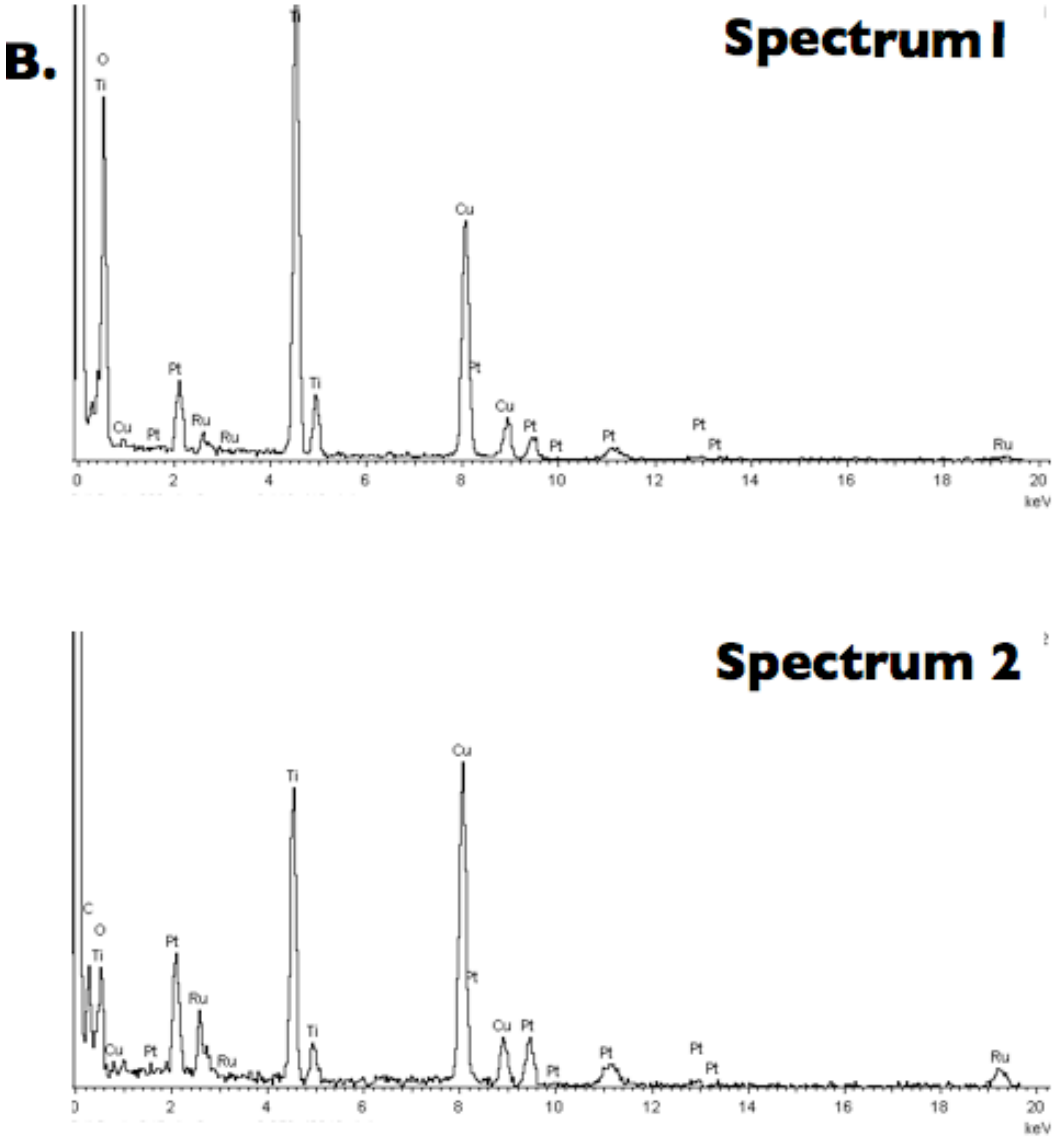

Figure 4-7 A): STEM HAADF image of the sample; and B): EDX spectra of the highlighted areas in A)

High-resolution observations Figure 4-8 (B and D) in STEM HAADF mode were conducted to the areas highlighted in white square in Figure 4-8 A and C, indicating that the catalyst nanoparticles possessed a core-shell structure, Pt rich in shell and Ru rich in

core. The thickness of the Pt rich shell is approximately from 0.6 nm to 1.3 nm, which is about 10 to 20% of the diameter of the nanoparticles presented in Figure 4-8 B and D.

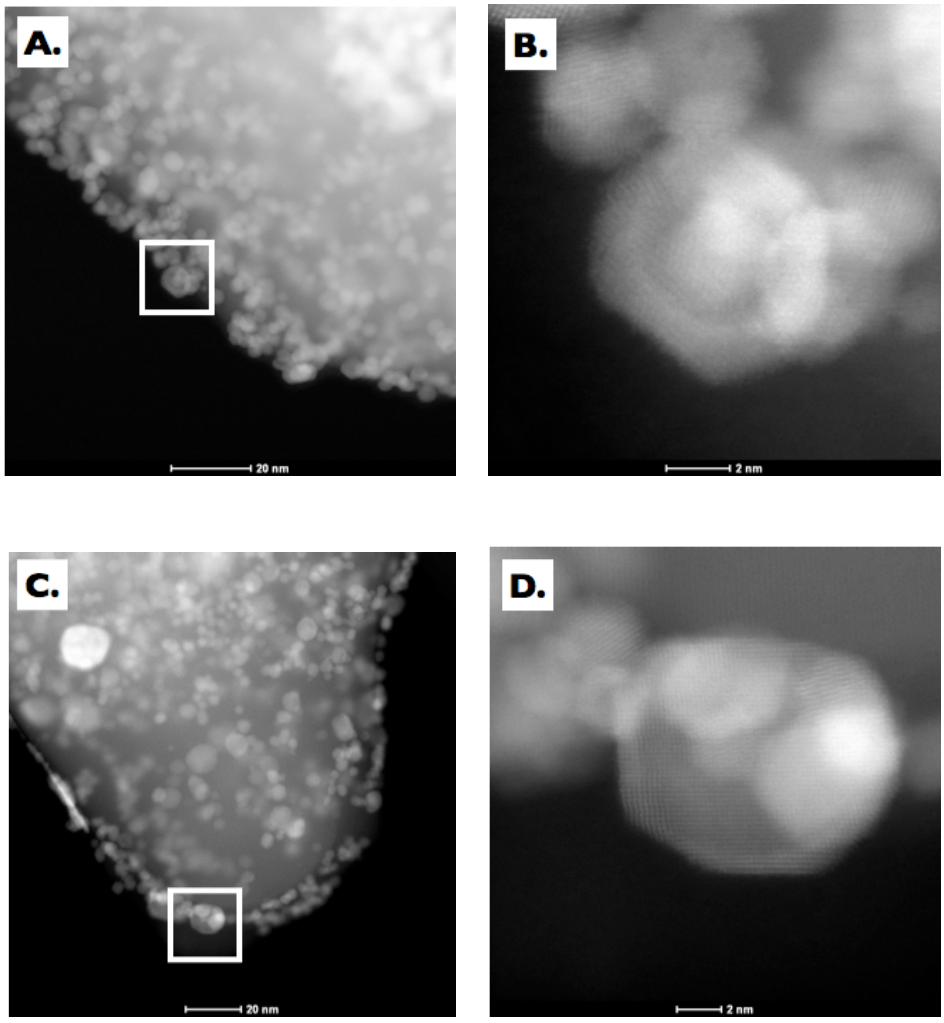

Figure 4-8 A) and C): STEM HAADF images of the catalyst sample at relatively low magnification; B) and D): high resolution micrographs in STEM HAADF mode of the highlighted square areas in A and C, presenting the nanoparticles with core-shell structure.

The elemental distribution of the individual nanoparticles with core-shell structure was further confirmed using EELS mapping as shown in Figure 4-9. Figure 4-9 A presents a typical nanoparticle with core-shell structure with a dimension about 20nm, which appears to overlap with a few smaller nanoparticles adjacent to its side. However, the shell of the large particle (highlighted by the green frame) is still visible. Ru and Pt maps of the corresponding area clearly demonstrate the variation of these two elements from the shell to core. The colour-coded composite map including signal from both Ru and Pt is shown in Figure 4-9 D, not only further confirming the core-shell structure but also indicates there is an area on the same particle with thinner or no Pt shell identified using white arrows. This thinner or lack of continuous Pt shell suggests some epitaxial effects with the Pt only covering most facets of the particles but not all.

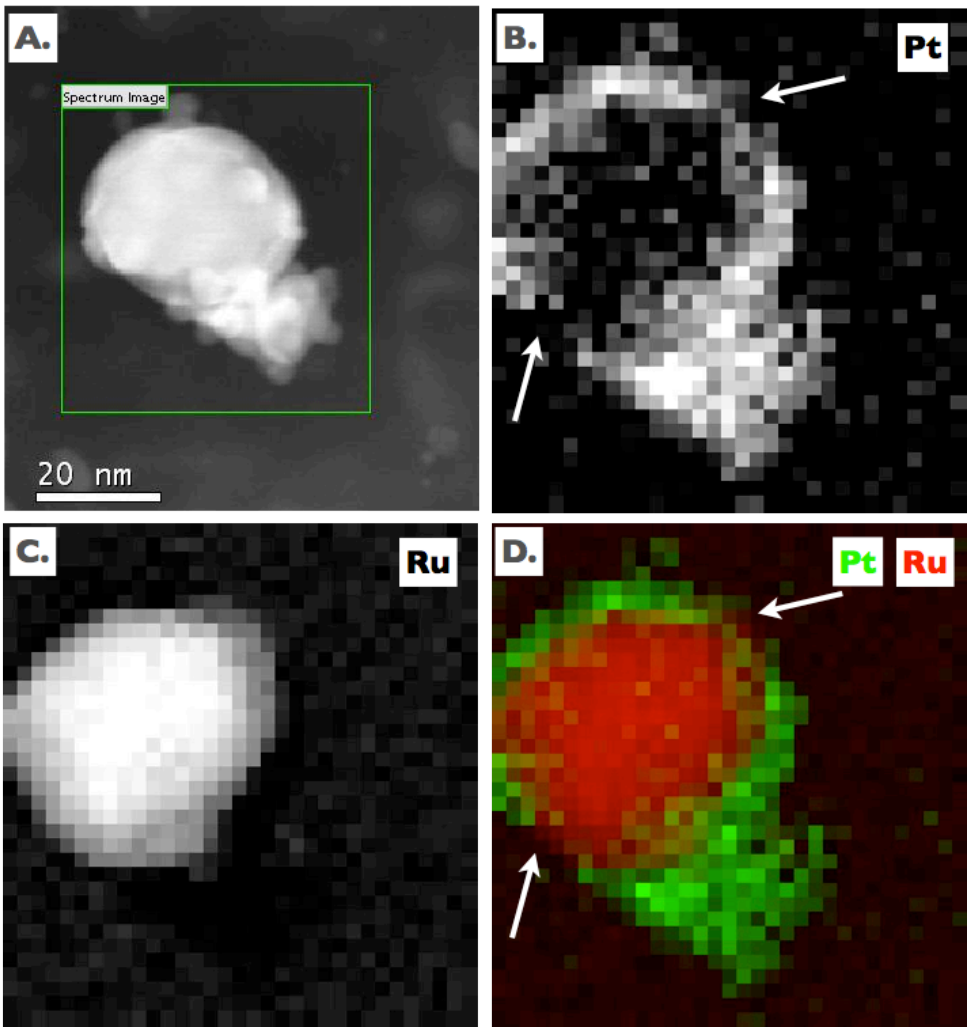

Figure 4-9 A): HAADF imaging of the area where further EELS mapping within the area framed by green line is carried out; B) and C) Ru and Pt maps respectively; D) composite maps including signal from both Ru (red) and Pt (green) .

More EELS mapping observations were carried out to study particles with different sizes, in order to probe Pt and Ru distribution variations. It is observed that the particle larger than 10nm, possess a relatively complete Pt shell as shown in Figure 4-10 and

Figure 4-11, while the core area is typically Ru rich as presented in Figure 4-12. The particles with smaller size, about 10nm, have an incomplete Pt shell (Figure 4-13).

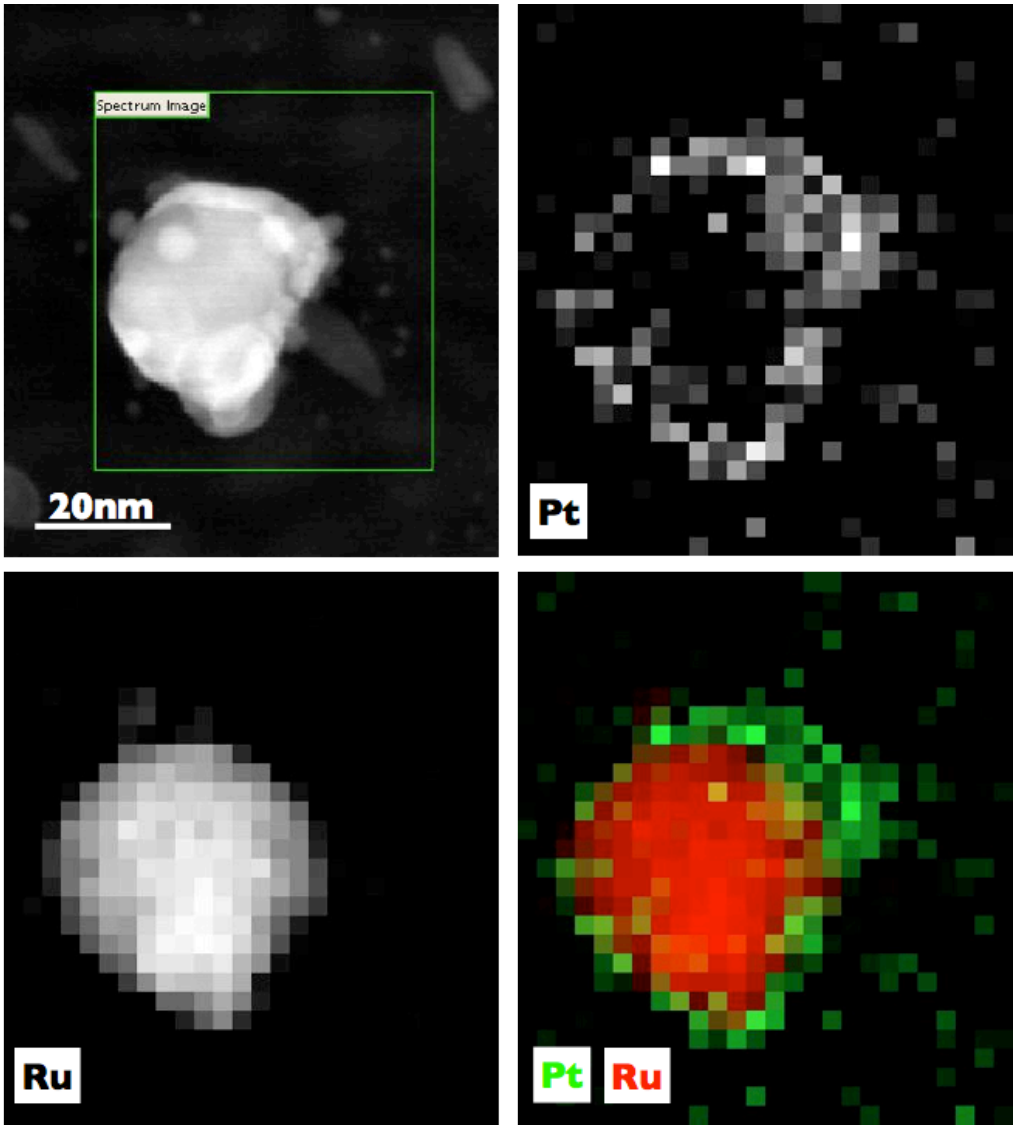

Figure 4-10 EELS maps of a typical nanoparticle with core-shell structure with a dimension about 25nm, overlapped with a few smaller nanoparticles

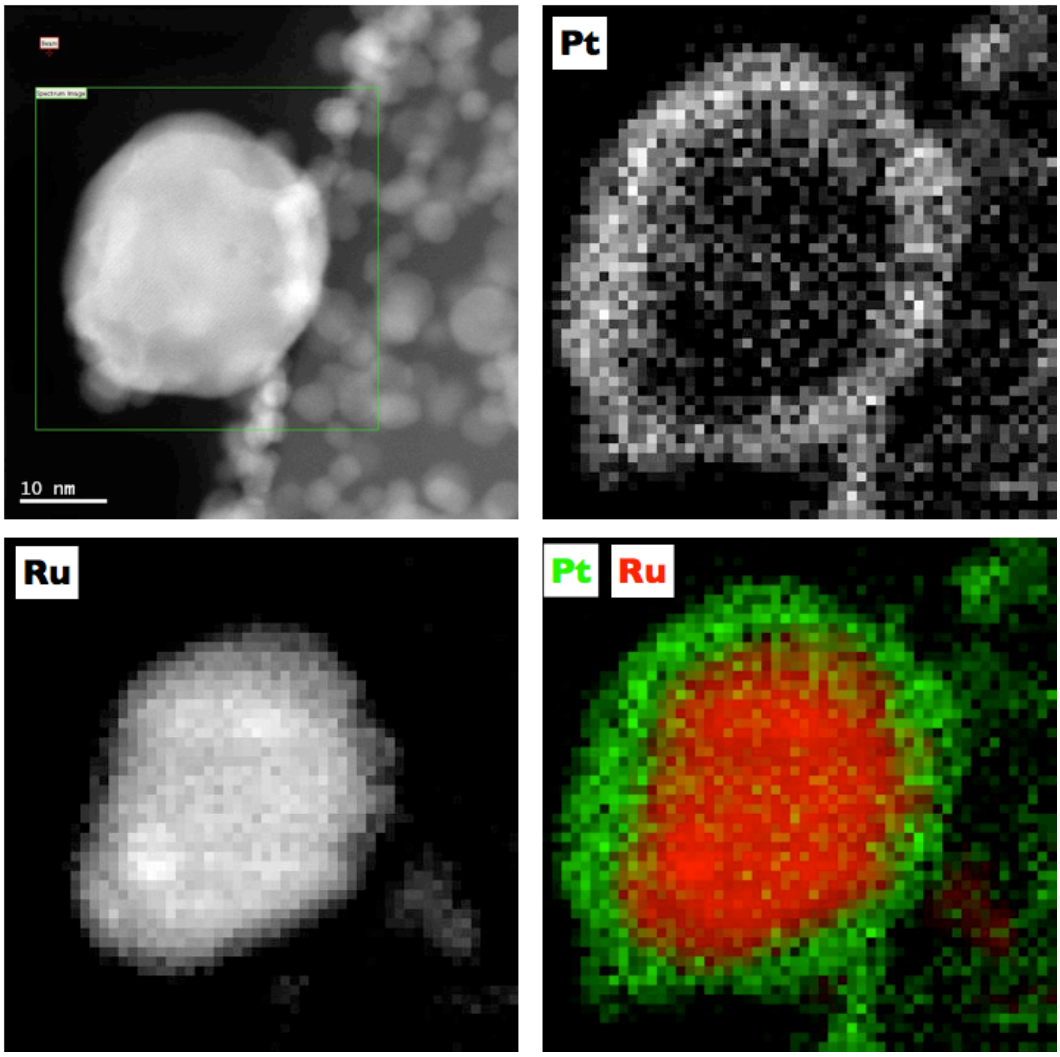

Figure 4-11 EELS maps of a typical nanoparticle with core-shell structure with a dimension over 20nm. It seemed that most of the very small particles surrounding the large one are only Pt.

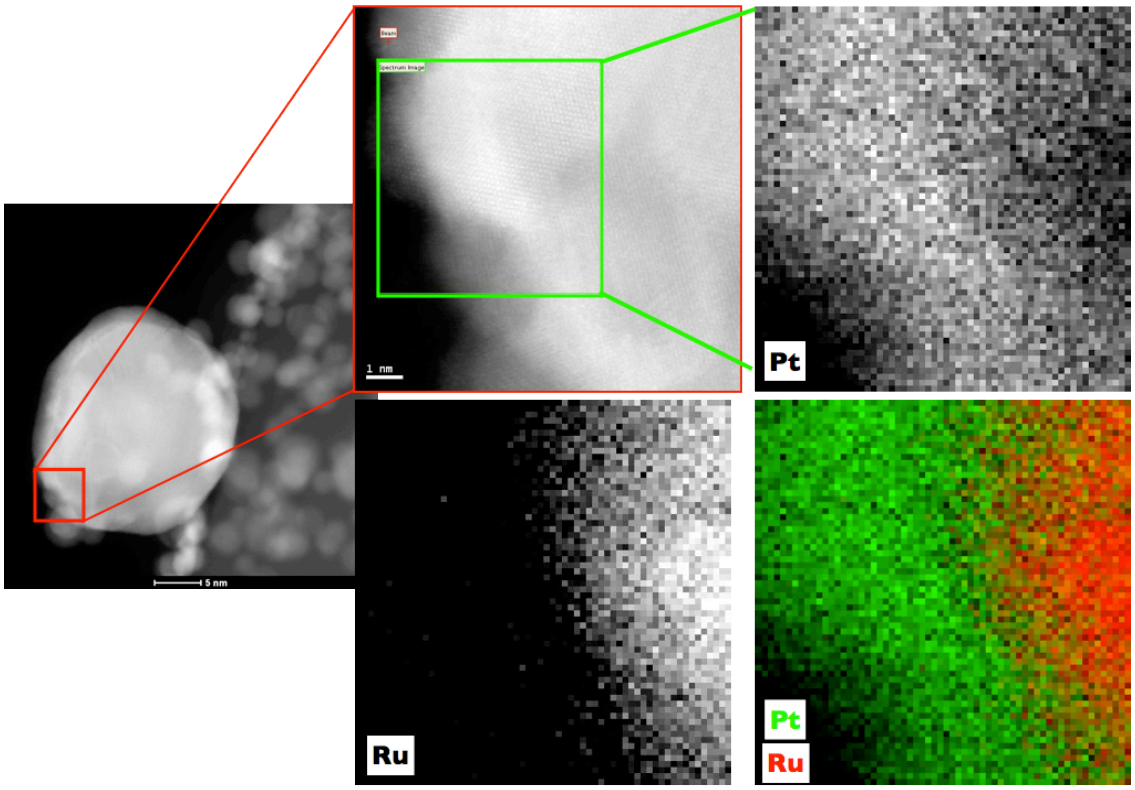

Figure 4-12 EELS maps of the highlighted area of the same particle presented in figure 4-11, indicating the Pt rich shell and Ru rich core of the selected area.

The measurement of surface atomic displacement is possible with the atomically resolved HAADF image shown in Figure 4-13. This result demonstrates a change of the interlayer distance at the surface compared to the bulk platinum. Prior to the calculation, the image is filtered by using bandpass filter in ImageJ to reduce the noise. The local positions of the maxima are then identified within ImageJ scripts to locate the column centers in Figure 4-13B. Lastly, the local maxima of the Ru core are used as a reference to

extrapolate the locations of the atoms and the determination of the local maxima allows the determination of the inter-atomic distances in the [111] direction.

To understand the consequence of these measurement, we need discuss the three fundamental effects in bimetallic catalysis: ensemble, ligand and geometric. Ensemble effects are caused by dissimilar surface atoms taking on distinct mechanistic functionalities. Ligand effects are related to the adjacent dissimilar surface metal atoms which induce electronic charge transfer between the atoms and affects their electronic band structure. Geometric effects are differences in reactivity based on the atomic arrangement of surface atoms and may include compressed or expanded arrangements of surface atoms (surface strain), which is the case presented in Figure 4-13.

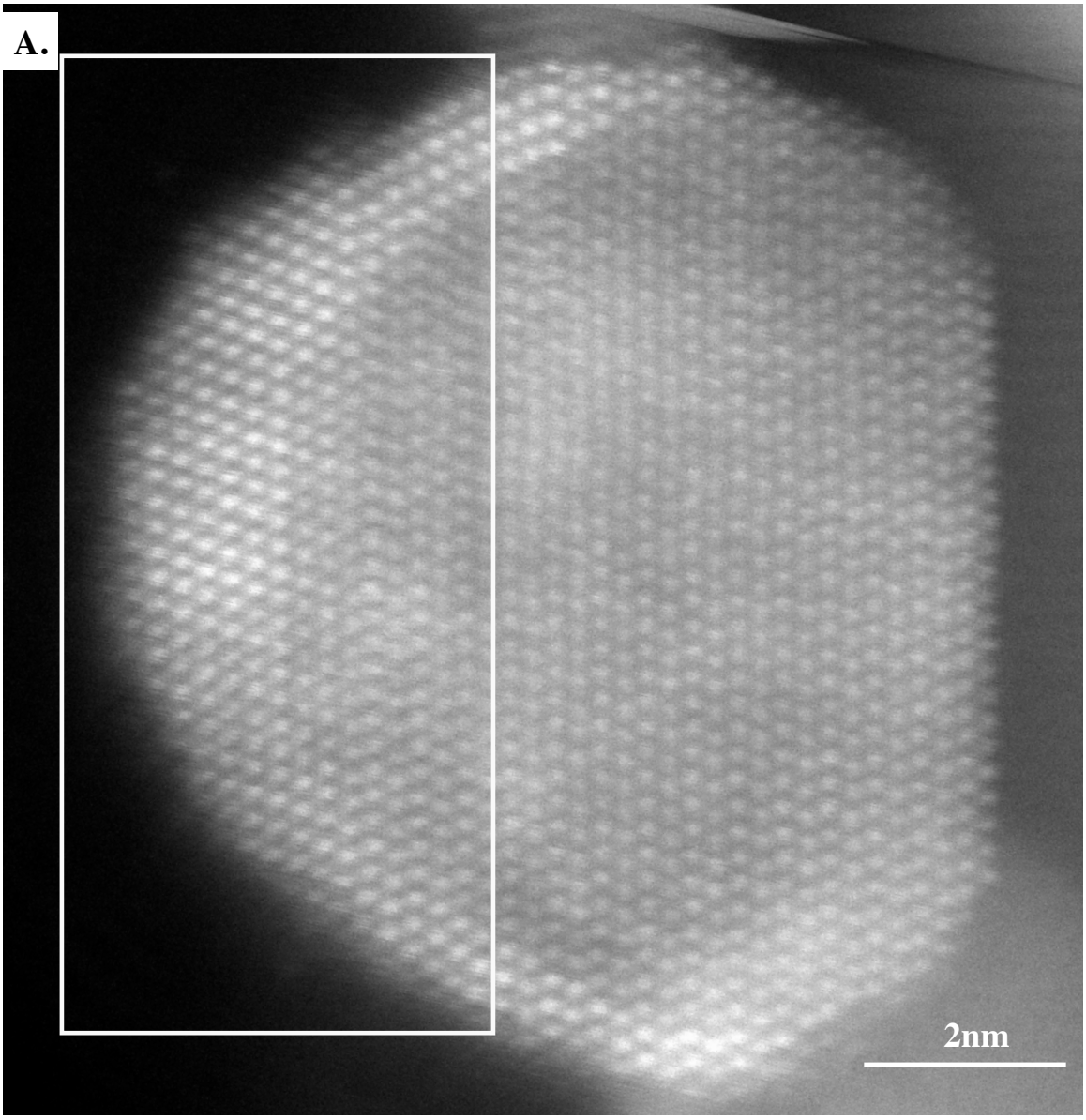
A.
2nm

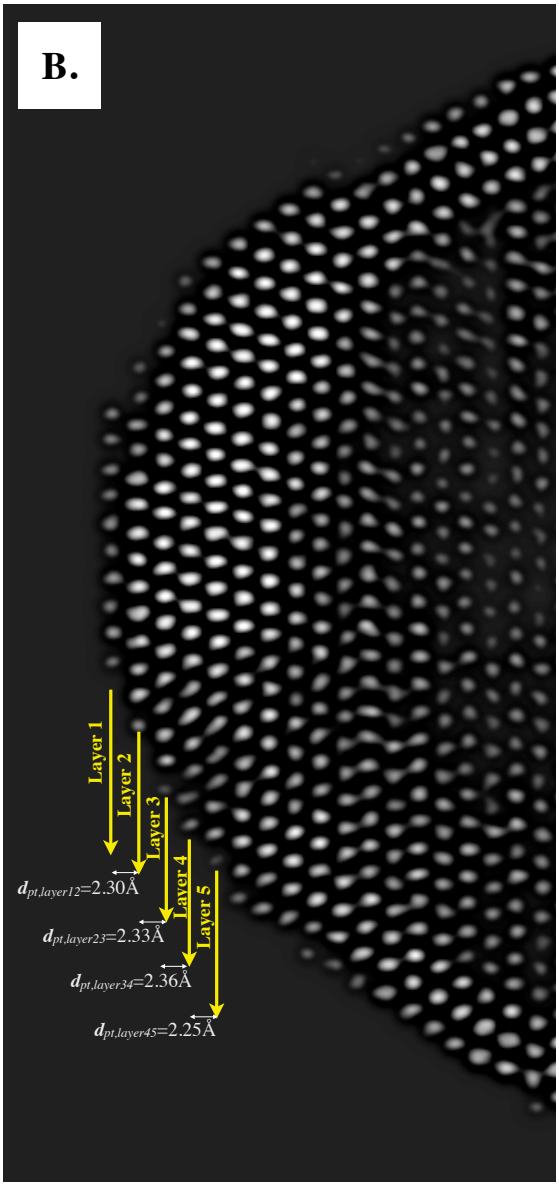
B.
Layer 1
Layer 2
Layer 3
Layer 4
Layer 5
$d_{pt,layer12}$=2.30Å
$d_{pt,layer23}$=2.33Å
$d_{pt,layer34}$=2.36Å
$d_{pt,layer45}$=2.25Å

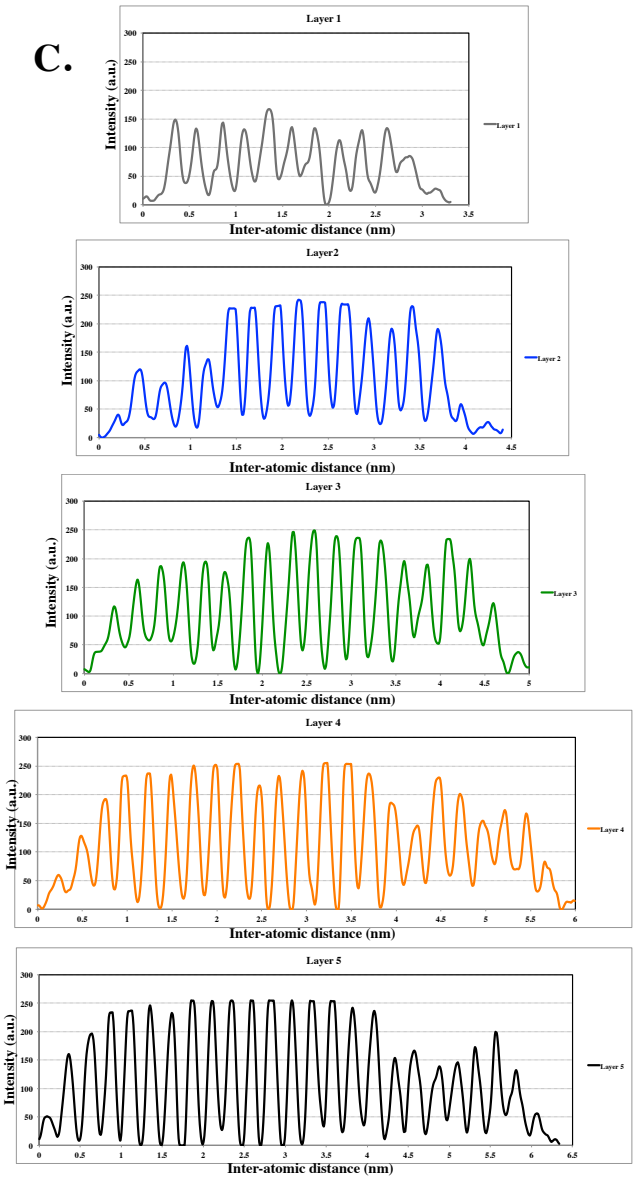
C.
Layer 1
Intensity (a.u.)
Inter-atomic distance (nm)
Layer2
Layer 3
Layer 4
Layer 5

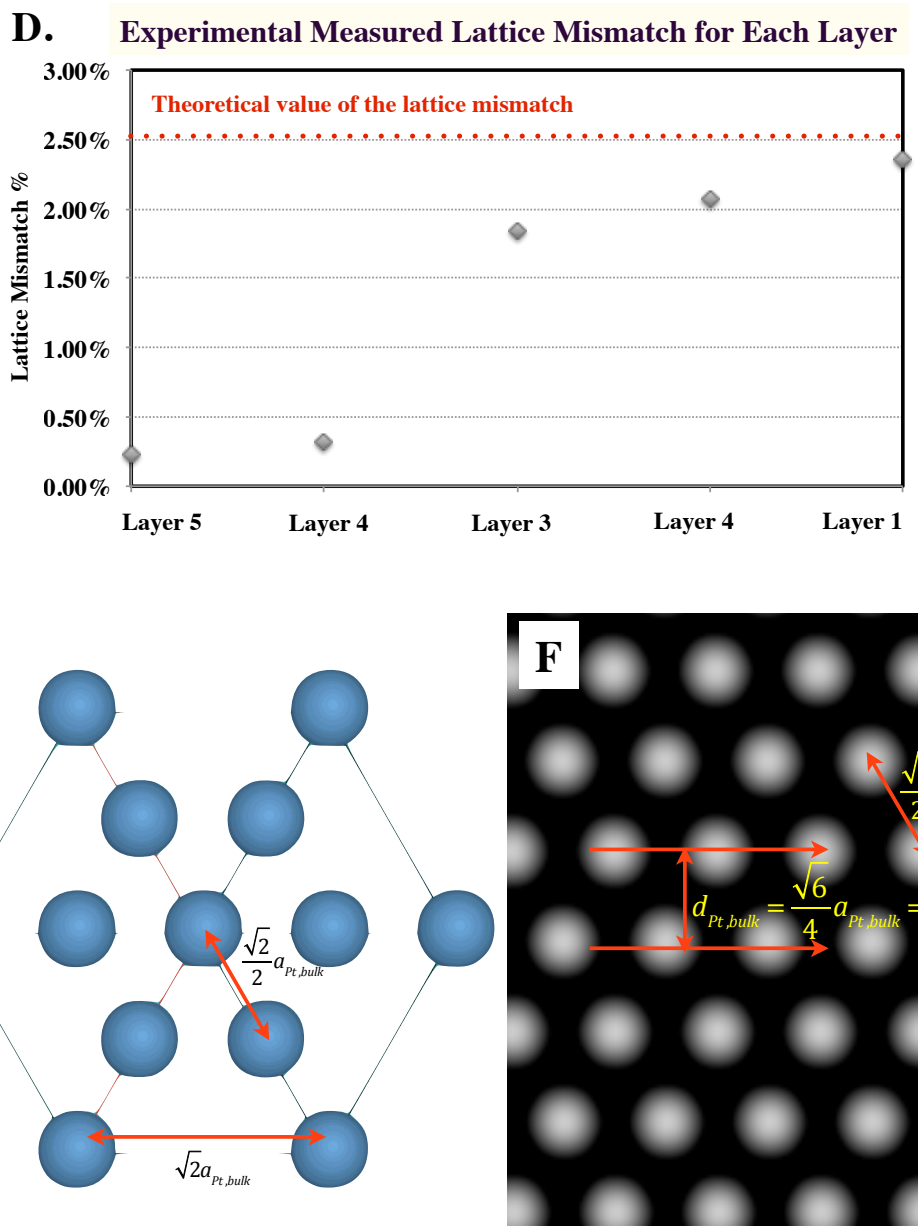

Figure 4-13 (A) STEM HAADF image of the PtRu particle with the size about 10nm (B): image filter was applied to the highlighted area in (A) in order to reduce the noise, the Pt rich shell was labeled from layer 1 to layer 5; (C): intensity line profiles of 5 identified layers, which is used to calculate the average inter-atomic distance for each

layer; (D): experimental calculated lattice mismatch according to the measurement involved in (C); (E) illustration of the Pt single unit cell viewed from (111) orientation; (F) simulated HAADF image of (E)

Given the core–shell nature of the catalyst particles, the lattice strain in the Pt shell is most relevant for surface catalysis. We assumed a Pt rich shell with lattice parameter a_{shell} that surrounded a Ru rich core with lattice parameter a_{core}. The interatomic distance in the projected image for shell, from Pt (111) zone axis, identified as $d_{shell/Pt(111)}$. The projected interatomic spacing for core area, from Ru (0001) zone axis, is identified as $d_{core/Ru(0001)}$. The theoretical lattice mismatch, $S_{(Pt)}$, in the particle shell relative to particle core, is given by equation (1)

$$S_{Pt} = \frac{d_{shell} - d_{core}}{d_{core}} \times 100\% = \frac{d_{shell/Pt(111)} - d_{core/Ru(0001)}}{d_{core/Ru(0001)}} \times 100\%$$

- As shown in to Figure 4-13 (E) , $d_{shell/Pt(111)} = \frac{\sqrt{2}}{2} a_{shell}$

$$S_{Pt} = \frac{\frac{\sqrt{2}}{2} a_{shell} - a_{core}}{a_{core}} \times 100\% = 2.52\% \qquad (1)$$

As shown in Figure 4-13 (D), the experimental measured lattice mismatch of the Pt shell is smaller than the theoretical value, which is due to the compressed interatomic distance of the top layers of the Pt rich shell. The actual local spacing between different

layers was measured as shown in Figure 13 (B). The spacing from the surface layer to the inner layer is 2.30Å ($layer_{12}$), 2.33Å($layer_{23}$), 2.35Å($layer_{34}$), 2.25Å($layer_{45}$), respectively. Figure 4-13 (E) to (F) illustrates the calculation of the spacing of the bulk Pt (2.403Å). Figure 4-13 (E) presents the Pt single unit cell viewed from (111) orientation by using JEMS.

The strain of the Pt shell (ε) is identified as the difference between the spacing between the bulk Pt ($d_{Pt,bulk}$) and the actual local measurement d_{Pt}, which is given by equation (2) as below:

$$\varepsilon = \frac{d_{Pt} - d_{Pt,bulk}}{d_{Pt,bulk}} \qquad (2)$$

According to the measurement of the interatomic distance of the shell, we found that the lattice mismatch between the Pt rich shell and the Ru rich core causes a decreased Pt–Pt interatomic distance and compressive strain within the Pt rich shell compared to pure bulk Pt. This induced compression of the lattice could affect significantly the reactivity and CO tolerance of the catalyst nanoparticle. The measurement of the interatomic distance is achieved by calculating the average interatomic distance from the top layer of the shell to the inner layer, identified as layer 1 to layer 5 as shown in Figure 4-13 B. Following equation (1), we calculated the experimental measured lattice mismatch $S_{(Pt)m}$

in the particle shell relative to the core. The lattice strain is calculated following the equation (2) for the Pt rich shell of the catalyst particle (Figure 4-13 B) relative to the bulk Pt (Figure 4-13 E to F). Following equation (2), the lattice strain for the Pt shell is calculated, which is -4.3% ($layer_{12}$), -2.9%($layer_{23}$), -1.9%($layer_{34}$), and -6.2%($layer_{45}$), respectively there the negative sign indicates a compression. The results indicate there is compression existed within the Pt rich shell.

To gain insight into how the compression of the core-shell catalysts affects the catalytic surface reactivity, there were a number of studies conducted by several research groups. For example, the d-band model developed by Nørskov and his co-workers has successfully related the adsorption properties of rate-limiting intermediates in catalytic processes to the electronic structure of the catalyst. For simple adsorbates, such as the ORR intermediates O and OH, this can be understood in a simple electron-interaction model in which the adsorbate valence p-level forms bonding and antibonding states with the metal d-band. The population of any antibonding state leads to Pauli repulsion, and the bond strength is thereby weakened. A downward shift of the d-band pulls more of the antibonding states below the Fermi level, which results in increasing occupation and weaker adsorbate bondings.[93]

Density functional theory studies from Alayoglu's works suggest that the enhanced catalytic activity for the core–shell nanoparticle originates from an increased availability of

CO-free Pt surface sites on the Ru@Pt nanoparticles. In their studies, the Ru@Pt nanoparticles are modeled by a four-layer slab of Ru h.c.p. lattice, with a 2 × 2 surface unit cell exposing the {0001} facet. The top layer of Ru atoms is replaced with Pt atoms (Pt*/Ru(0001)). As shown in Table 4-1, the reactivity of the Pt (111) surface and Pt*/Ru(0001) surface were compared through the calculated binding energies of reaction intermediates and the activation energy barriers (Ea) for elementary reaction steps. The binding energies for various species were calculated following the proposed reaction mechanism presented in Table 4-1.

In Alayoglu's study, the Pt monolayer deposited on the Ru (0001) substrate was compressed compared with the lattice constant of pure Pt-bulk. It was suggested that this compression would tend to decrease the interaction strength of adsorbates on Pt surface atoms in Ru@Pt particles. Moreover, when compared with the Pt atoms in the top layer of a Pt(111) surface, the interaction of the Pt-monolayer with the Ru-support atoms causes a further downshift in the d-band centre of surface Pt atoms, from –2.53 eV for pure Pt(111) to –2.98 eV for the Pt*/Ru(0001) surface. Downshifting the d-band centre of a surface has been shown to decrease the interaction strength of the surface with various adsorbates. As listed in Table 4-1, Alayoglu's study verified the general trend: Pt*/Ru(0001) binds all adsorbates less strongly than Pt(111). Atomic oxygen (O) and carbon monoxide (CO) show the largest reduction in binding energy, by 0.76 and 0.57

eV, respectively. In turn, the weaker CO binding on Pt*/Ru(0001) results in lower CO saturation, coverages for Pt*/Ru(0001), than on Pt(111).[116]

Table 4-1 Calculated binding energies of various species at 1/4 monolayer coverage and the activation energy (Ea) barriers of different elementary steps on Pt(111) and Pt*/Ru(0001) [116]

	Pt(111)	Pt*/Ru(0001)
d-band centre of surface Pt atoms, ε_d (eV)	−2.53	−2.98
Species	Binding energy (eV)	Binding energy (eV)
O_2	−0.65	−0.26
O	−3.87	−3.11
H	−2.72	−2.42
O_2H	−1.09	−0.95
OH	−2.09	−1.91
CO	−1.82	−1.25
H_2O	−0.27	−0.20
Elementary reactions	E_a (eV)	E_a (eV)
$H_2 + 2^* \rightarrow 2H^*$	0	0.16
$O_2 + 2^* \rightarrow 2O^*$	0.77	1.05
$O_2^* + H^* \rightarrow O_2H^{**}$	0.33	0.25
$O_2H^{**} \rightarrow O^* + OH^*$	0.16	0.42
$O^* + H^* \rightarrow OH^* + ^*$	0.85	0.58
$OH^* + H^* \rightarrow H_2O^* + ^*$	0.10	0.15
$CO^* + O^* \rightarrow CO_2^*$	0.79	0.41

Another example of this is found in Strasser's work [117] where researchers applied these ideas to single-crystal Pt surfaces by preparing and characterizing bimetallic single-crystal model surfaces that consist of atomic layers of Pt with various thicknesses grown on a Cu(111) substrate. This model mimics the structural and electronic environment of Pt layers that surround a particle core with significantly smaller lattice parameters, similar to the core-shell catalysts.

Researchers found that the d-band centre is downshifted from 2.87 eV to 3.26 eV below the Fermi level. The broadening is related directly to the compressive strain, because the electronic state overlap between the metal atoms increases with shorter interatomic distances; furthermore, keeping the d-occupancy constant for a pure metallic system gives rise to a downward shift of the d-band centre. To further corroborate the lattice-strain hypothesis in core–shell structures, Strasser's work experimentally verified the predicted effects on the band structure for compressively strained Pt layers. [117]

Instead of using the ideal system to study the core-shell structure effect, as in DFT calculation (Alayoglu) or deposited monolayer Pt on the substrate (Strasser), we studied the real catalyst nanoparticles that are used in PEMFC operation. Using the STEM HAADF imaging technique, we were able to probe and demonstrate the compressive strain existed within the shell.

As earlier DFT studies (Alayoglu) suggested, the compressed lattice of the shell layer of the Ru@Pt catalyst will increase the electronic state overlap of the Pt atoms. In addition, the d-band centre (ε_d) of the surface Pt of Ru@Pt catalyst is downshifted compared with Pt atoms in the top layer of pure Pt catalysts. Current STEM HAADF study represents the direct experimental confirmation of the computational prediction of band shifts of adsorbate-projected band structure by analyzing the real catalyst materials applied in PEMFC operation.

According to the Hammer-Nørskov mode (Nørskov), the CO binding energy should be proportional to the center of the locally projected d band of the surface atom. Therefore, the CO binding energy to the Pt rich layer of the particle shell decreased while the d-band centre (ε_d) of the surface Pt of Ru@Pt catalyst is downshifted.

For the elementary reactions,

$$A + * \underset{k_A^-}{\overset{k_A^+}{\rightleftharpoons}} A*$$

the fraction of occupied sites by species A is identified as θ_A following the equation below,

$$\theta_A = \frac{K_A p_A}{1 + K_A p_A} = 1 - \frac{1}{1 + K_A p_A} \quad (3)$$

where $K_A \propto e^{-E_a/RT}$ (4), and p_A is the partial pressure of A. As calculated from DFT studies (Alayoglu), the activation energy E_a of the elementary reaction step of $H_2 + 2* \rightarrow 2H*$ is increased, following equation (3) and (4), the fraction of occupied Pt sites by H_2 is increased at the Pt surface of the Ru@Pt catalyst.

In contrast, the activation energy E_a of the elementary reaction step of $CO + O* \rightarrow CO_2$ is decreased, resulting decreased fraction of occupied sites by CO and lower CO

saturation accordingly, so that improved CO tolerance of the catalyst layer could be achieved.

The resulting activity–strain relationships provide experimental evidence that the deviation of the Pt-shell lattice parameter from that of bulk Pt, that is the lattice strain in the shell, is the controlling factor in the catalytic enhancement of Ru@Pt nanoparticles; in particular, these relationships are consistent with computational predictions presented in Alayoglu's work that compressive strain enhances CO tolerance.

In conclusion, a coherent picture of the origin of the exceptional electrocatalytic properties for Ru@Pt particles is now established. Strain forms in Pt-enriched surface layers (shells) that are supported on a Ru rich core with a smaller lattice parameter. The compression in the shell modifies the d-band structure of the Pt atoms, and thereby weakens the adsorption energy of reactive intermediates compared to unstrained Pt and results in an increase in the catalytic reactivity, consistent with DFT predictions in earlier studies. Current STEM HAADF study provided the direct evidence that a unique feature of core-shell catalysts is the experimental control over the extent of induced strain and core composition. Both expansive and compressive strain can be achieved to control the strengthening or weakening of surface bonds by using different constituent elements. This enables continuous tuning of catalytic reactivity.

Further observations were conducted to study the particles more typical of the average size based on the distribution measured in Figure 4-6. From these measurements, we show that only Pt is detected (Figure 4-15, Figure 4-16 and Figure 4-17) in the small particle of about of 5nm size. Thus, our results on a range of particle sizes suggest that the many particles (in fact the majority) that are just Pt on the Ti_4O_7 might be the source of the actual electrochemical performance improvement, and not only the larger Ru-core Pt-shell particles.

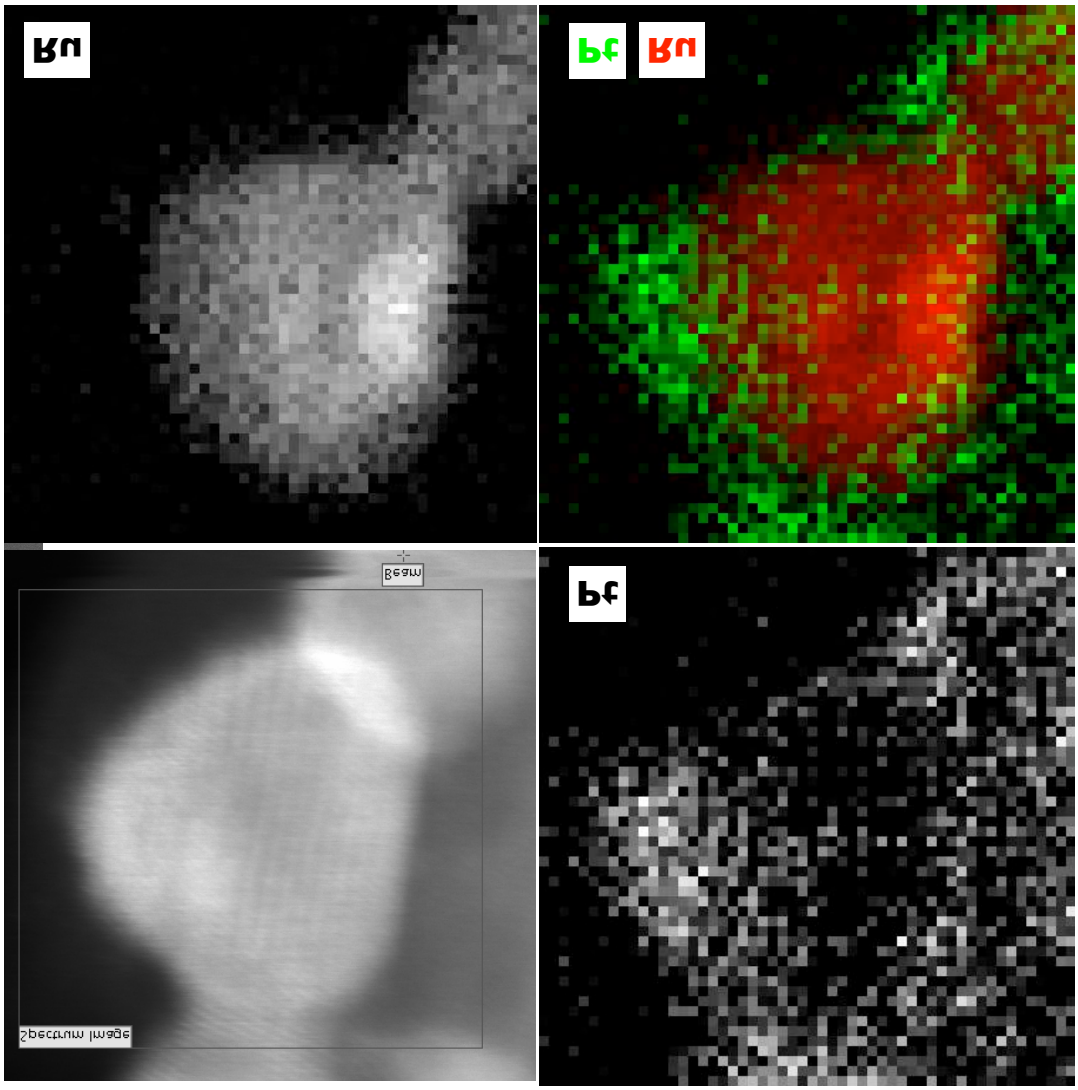

Figure 4-14 EELS maps of the catalyst nanoparticles presented in figure 4-13, dimension of which is about 10nm.

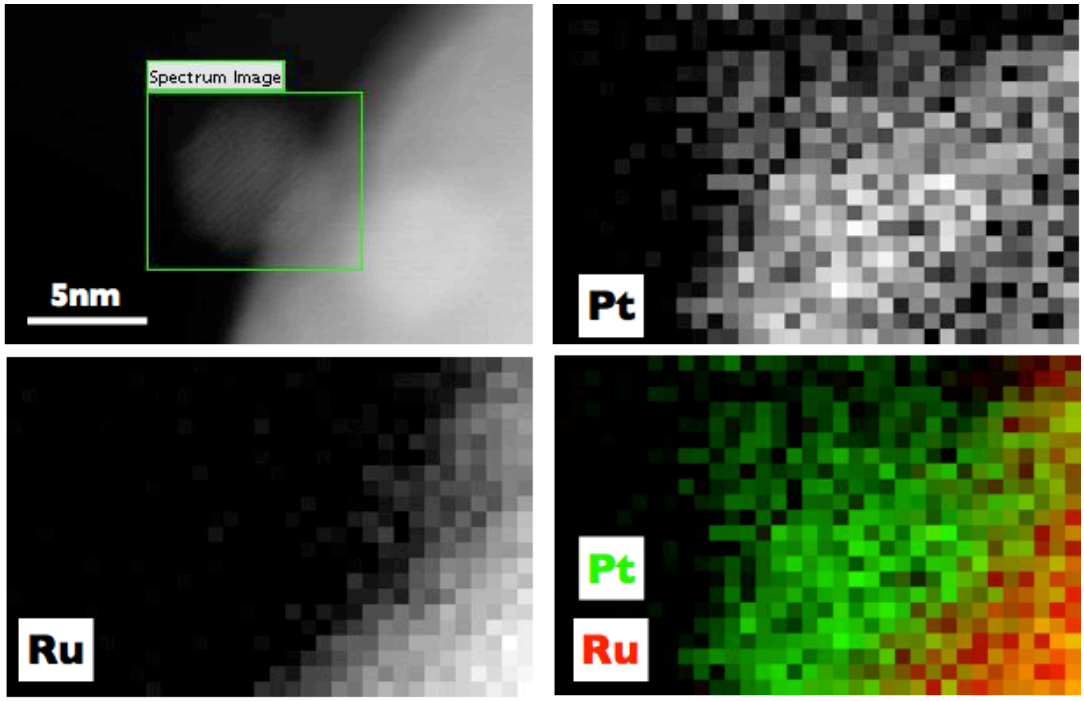

Figure 4-15 EELS maps presents a Pt catalyst nanoparticle with a dimension about 5nm near a Ru rich particle

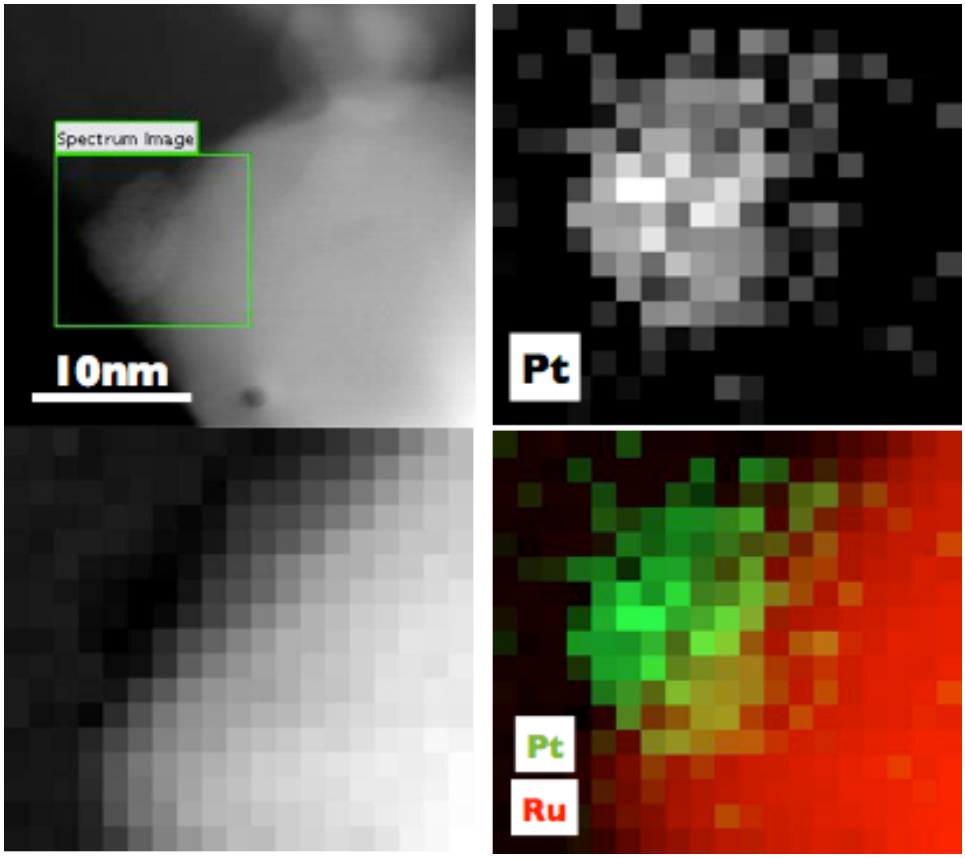

Figure 4-16 EELS mapping result of a Pt catalyst nanoparticle with a dimension about 5nm near a Ru rich particle

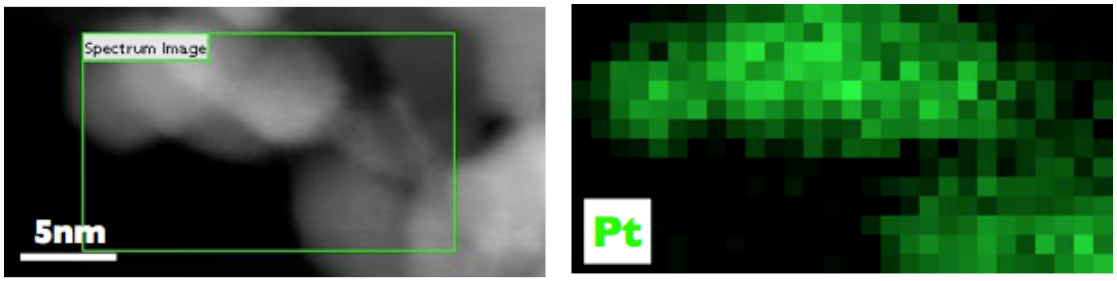

Figure 4-17 EELS maps of Pt catalyst nanoparticles with an average dimension about 5nm supported on the oxide

The improved CO tolerance is also demonstrated through the electrochemical measurement conducted by IFCI collaborators, as shown in below Table 4 - 1. The anode feed gas of H_2 containing 10, 50, 100, 300, and 500 ppm CO was used respectively to investigate the CO tolerance of the Ru@Pt/Ti_4O_7 comparing with the commercial pure PtRu alloy catalyst with conventional carbon support. As concentration of CO is increased, the performance of the catalyst is decreased since more CO occupied the active sites on pure Pt particles, leading to higher CO saturation coverage. However, when the Ru@Pt/ Ti_4O_7 core–shell catalyst consisting of novel structure of Ru-rich core and Pt-rich shell is used, higher CO tolerance can be achieved, compared to that of PtRu/C catalyst in various CO concentrations as shown in the Table 4 - 1.

Table 4 - 1 Overpotentials at a current density of 1.0A/cm^2 at various CO concentrations [120]

CO concentration (ppm)	Overpotential at 1.0 A/cm^2 using Ru@Pt/Ti_4O_7 catalyst (mV)	Overpotential at 1.0 A/cm^2 using PtRu/C alloy catalyst (mV)	Overpotential reduction (mV)
0	30.5	81.6	−51.1
10	30.6	203.7	−173.1
50	37.9	241.6	−203.7
100	41.2	245.2	−204.0
300	105.4	891.0	−785.6
500	179.2	938.6	−759.4

The major differences between the Ru@Pt/ Ti_4O_7 catalyst and commercial available PtRu/C catalysts are the structure of the catalyst nanoparticles and the support materials.

1). Unique structure of the catalyst nanoparticles: For Ru@Pt/Ti_4O_7 catalyst presented in current study, the core-shell structured Ru@Pt existed for the catalyst nanoparticles with relatively larger size (>5nm). The EDX and EELS characterization results confirmed this Ru@Pt/Ti_4O_7 catalyst synthesized by microwave irradiation approach, had indeed a core–shell structure with a Ru core and a Pt shell but that the smaller particles <3 nm contain only Pt (Figure 4-15, Figure 4-16, Figure 4-17). STEM HAADF results presented earlier demonstrate the induced strain with the Pt-rich shell of the Ru@Pt catalyst could be applied in tuning the catalytic performance.

2). Transition metal oxide is used as the catalyst support, comparing with the conventional carbon in the commercial available PtRu/C catalyst. As mentioned in earlier section (4.3.2), it has attracted great attention in recent years with respect to the development of non-carbon supported Pt and Pt alloy catalysts, including using transition metal oxide (i.e. TiO_x), in order to overcome the issue of carbon corrosion. It was reported the interaction between the Pt or Pt alloy catalyst and the support was found to be critical in improving both the catalyst activity and stability. [120] Therefore, as a further and continuous approach in exploring the catalysts, EELS analysis was conducted to learn the electronic structure of the non-carbon support Ti_4O_7 that used as the support for Ru@Pt catalyst.

As shown in Figure 4-18, Preliminary EELS analysis with 0.1eV energy resolution was conducted over the support of the catalyst sample. Different locations from the surface to the centre of the catalyst support were highlighted in red in Figure 4-18A. The EELS spectra of corresponding areas were presented in Figure 4-18B. Comparing the experimental results with the reference EELS spectra in Figure 4-18 C, there is large content of TiO_2 instead of Ti_4O_7. Both anatase and rutile exist within the support, and the relative content of the two phases changes at different locations of the particle sample.

According to the observed results, such electronic structure change indicates the strong interaction between the noble metal catalyst and transition metal oxide support, which is generally considered as a typical system for Strong Metal-Support Interactions (SMSI) effect. For the SMSI effect, one would expect transfer of d electrons from platinum (d7sp2) to low-lying vacant orbitals of titanium.[63] For every electron transferred with resulting unpairing of two internally paired electrons, two electrons are made available for bonding by pairing between atoms, and forming stable hypo-hyper bonding between Ti and Pt which will improve the stability of the catalyst.

B.

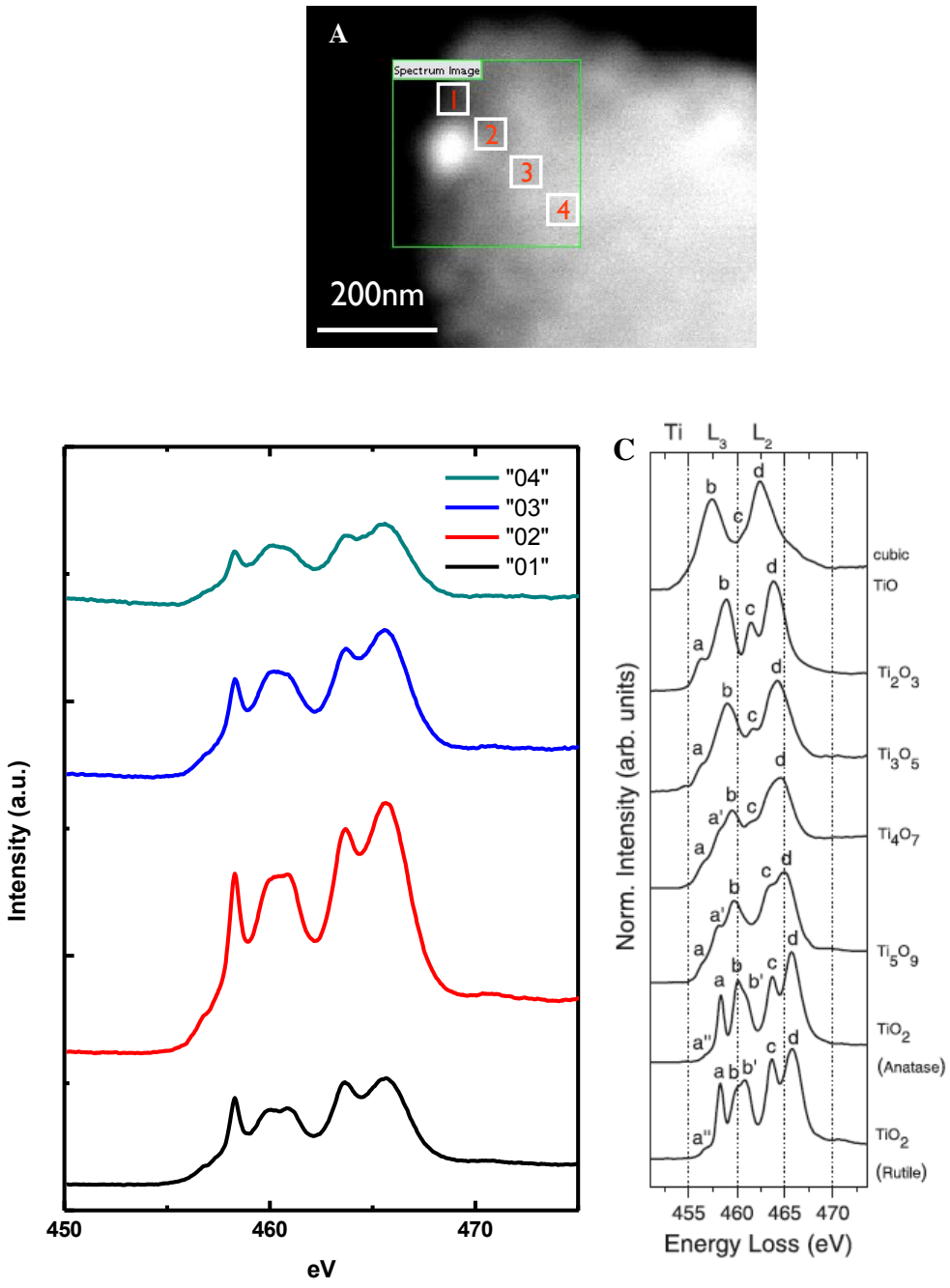

Figure 4-18 A: different locations from the surface to the centre of the catalyst support were highlighted in red; B: the EELS spectra of corresponding areas in A; C reference EELS spectra, American Mineralogist Volume 92, pages 577.586, 2007

4.4 Conclusion

The ultimate goal in catalytic design of the PEMFC is to have complete synthetic control of the material properties that determine the reactivity. Catalysts that consist of two metals (bimetallic) allow greater reactivity and more flexible design, as presented in this chapter. In the current study of Pt/Ru nanoparticles, we have shown that the enhanced CO tolerance may be achieved through the interactions between the Pt shell and Ru core atoms, which can modify the electronic structure of the Pt surface by the presence of subsurface Ru atoms or by disrupting the Pt surface arrangement. This leads to decrease of the interaction strength of adsorbates on the Pt surface atoms in Ru@Pt nanoparticles including weaker CO bonding on surface Pt atoms/Ru support, compared with Pt atoms on pure Pt particles. This modification may significantly destabilize CO on Pt, leading to a lower CO saturation coverage, thereby providing more free active sites for hydrogen oxidation reaction.

Furthermore, the replacement of the conventional carbon support by titanium oxide significantly affected the morphology and distribution of the PtRu catalyst, including core-shell structure nanoparticles with different shell coverage as well as pure catalyst nanoparticle. Lattice measurement (Figure 4-13) suggested that, within core-shell structure nanoparticles, not only the shell is rich in platinum; the compressive strain within the surface results in a shift of the electronic band structure of platinum and weakening chemisorption of oxygenated species. It was reported in Strasser's

computational study, the deviation of the Pt-shell is one of the controlling factors of electrocatalytic activity due to the change of the Pt 5d antibonding state. [117] Current experimental results provide the direct observation of such deviation of the Pt-lattice change and presence of the compression strain.

Here, on an atomic scale, we present microscopic and spectroscopic evidence for the formation of a PtRu alloy core–shell nanoparticle structure using STEM HAADF imaging, EDX elemental analysis, and EELS analysis. Given the measurement of the lattice spacing deviation and strain of the shell, our results demonstrate the core–shell structure of the catalyst and clarify the platinum-rich shell exhibits compressive strain.

Chapter 5. Transition metal oxide with SMSI effect between catalyst and support

5.1 Introduction

The most important signature of the SMSI effect accounts for the drastic changes in the performance of the catalyst when group VIII metals like Pt, supported on transition metal oxides. Both Brewer and Tauster's works predicted one would expect the electronic structure change and formation of intermetallic phase in Pt/TiO_2 system, which is typical system for SMSI studies.[61-63] In the current work, Pt supported on TiO_x is systematically studied. Furthermore, comparable studies were also conducted by using different catalyst system, for example, Pt supported on various complex transition metal oxides. In this chapter, experimental characterization approaches are introduced in section 5.2. After presenting the results of experimental characterization of the material and discussions of Pt/TiO_x catalyst system (section 5.3.1), comparable study results over various transition metal oxides support is described in section 5.3.2. Further work related to the 3D structure study as well as SMSI effect study through EELS are presented respectively in section 5.3.3 and 5.3.4, followed by a general conclusion (section 5.4).

5.2 Characterization approaches

In this work, the morphology and dispersion of the catalyst nanoparticles on the support material at relative low magnification were examined using a conventional transmission electron microscope (TEM, Philips CM12). Samples for TEM observations were directly supported on a copper mesh with holey carbon microgrids. The FEI Titan 80-300 Cubed TEM, operating at 200 kV was used for high-resolution observation. The instrument is equipped with a Gatan Imaging Filter (GIF) for energy-filtered imaging and an energy dispersive X-ray detector for elemental analysis and mappings. The instrument is also equipped a CEOS-designed hexapole-based aberration corrector for the image-forming lens and one for the probe-forming lens. It can achieve sub-Ångstrom resolution both for phase contrast imaging and STEM. The electron microscope operates a high-resolution monochromator, which allows 0.1eV energy resolution for electron energy loss spectroscopy (EELS).

STEM High-Angle Annular Dark-Field (HAADF) and Bright-Field (BF) images were acquired using a scanned focused probe together with a HAADF detector and BF detector respectively on the FEI Titan 80-300 Cubed TEM. The FEI Titan 80-300 with only image corrector was used to acquire the bright-field TEM images and conduct basic elemental analysis of the sample.

HAADF-STEM images for tomography tilt series were acquired by using a FEI Titan 80–300 field emission gun transmission electron microscope operated at 300 kV and with a Fischione high-tilt tomography sample holder. Images were taken with a tilt range from -67° to 75 °, and a 1 ° increment. 138 images of the tilt series without specimen self-shadowing were used to reconstruct the volume. The FEI software package Xplore3D Acquisition was applied to control the tilt angle, to maintain the object within the field of view, to correct for focusing changes, and to record and store 2D images at different tilting angles. Tomographic reconstruction was carried out with the FEI Inspect3D package and visualization as well as the segmentation of the reconstructed volume was achieved by using the Amira 5.3 package. More detailed explanation of the application of STEM Tomography technique is included in Chapter 6[126]

5.3 Results and discussion

5.3.1 Catalyst support with unique structure

The general morphology of the ($(Nb_2O_3+TiO_x)$ / C) sample prior to loading of the Pt catalyst is obtained with STEM in HAADF imaging conditions (Figure 5-1 A). The overview of this pure support shows the clear interconnected oxide network (relative bright area) structure on the carbon support (darker area) before catalyst loading. Based on Z-contrast, the bright features in the image correspond to the Nb and Ti atoms on the lighter background of the carbon support. No ordered arrangement of heavy atoms is observed suggesting no crystalline phase (Figure 5-1 B) is present following the synthesis. Such observations are fully reproducible and do not result from electron beam damage.

Following the Pt loading on complex support (10%Pt/20wt%Nb_2O_3/C) HAADF and bright-field imaging demonstrates that crystalline Pt catalyst nanoparticles are well dispersed on the hybrid graphitic carbon support (Figure 5-2). Combining imaging and elemental analysis, it was found that the catalyst nanoparticles are embedded into (and/or surrounded by) the oxide layer as pointed out using white arrows in Figure 5-2C. Higher loading on the same support, (30%Pt/20wt%Nb_2O_3/C), provides evidence of maintained uniform dispersion (Figure 5-3). Based on elemental mapping with energy dispersive X-ray spectrometry (Figure 5-4), it is possible to deduce that the Pt nanoparticles distribution is strongly correlated with the location of the transition metal oxide rather

than on the carbon. When present, the thickness of the disordered oxide network varies between 1nm to 2nm.

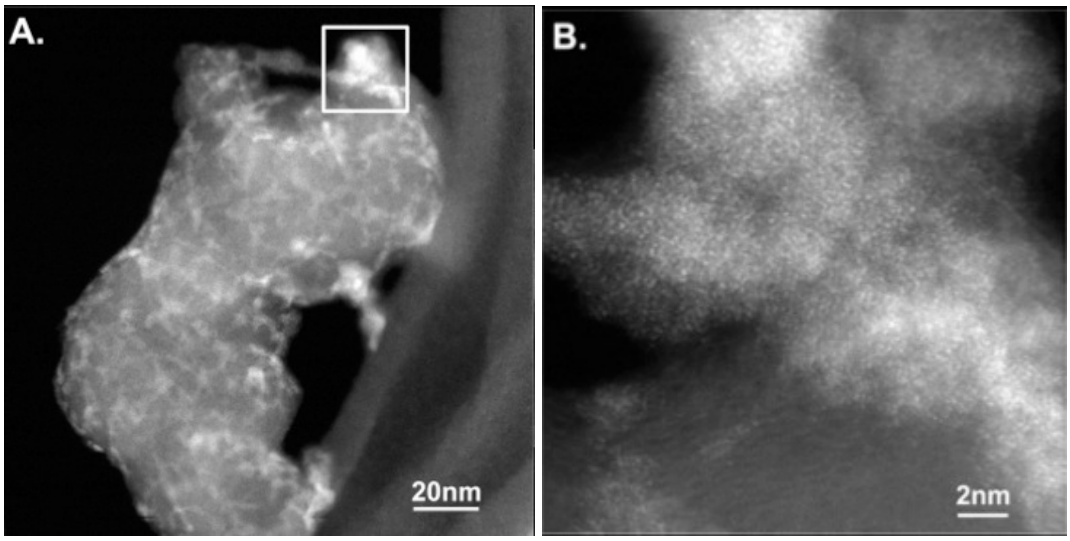

Figure 5-1 A) STEM HAADF image of the catalyst support of (Nb_2O_3+TiO_x) on carbon; B) high resolution micrograph of atomic resolved clusters within the oxide network region of the catalyst support

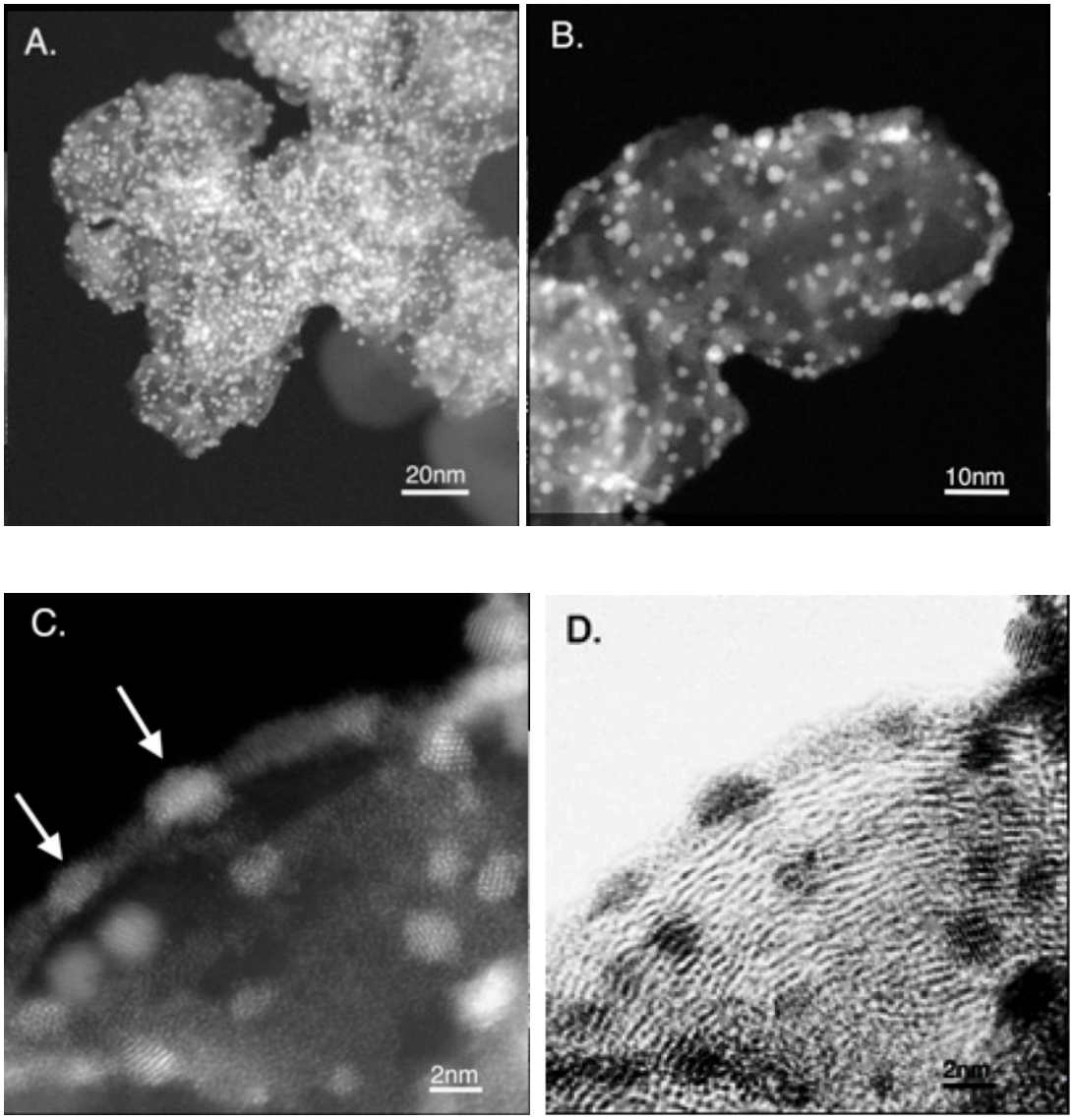

Figure 5-2 A and B) Overview of the catalyst particles at relatively low magnification, after loading Pt catalyst on the complex support, by using STEM HAADF; C) STEM HAADF micrographs and D) STEM bright-field of catalyst particles with highly distributed Pt nanoparticles on the support where the oxide network is visible as pointed by white arrows and the Pt by white arrows while the graphitic fringes of the carbon support are visible in D

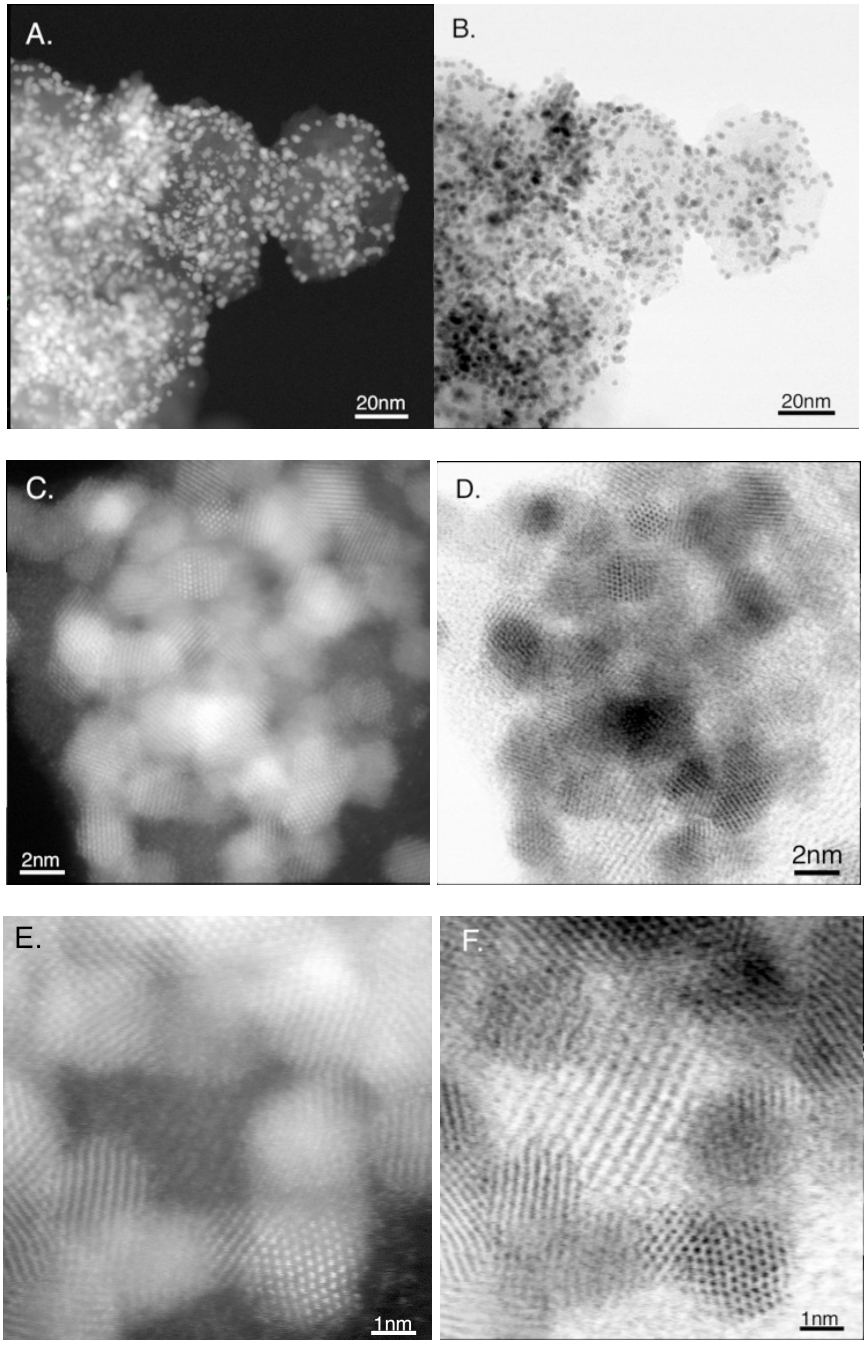

Figure 5-3 A and B) General morphology in STEM HAADF and bright-field STEM modes of the catalyst particles at relatively low magnification, after loading 30%wt Pt catalyst on the complex support; C and D) STEM HAADF micrographs of catalyst particles with highly distributed Pt nanoparticles on the support; E and F) detailed view of selected area in HAADF and BF STEM modes.

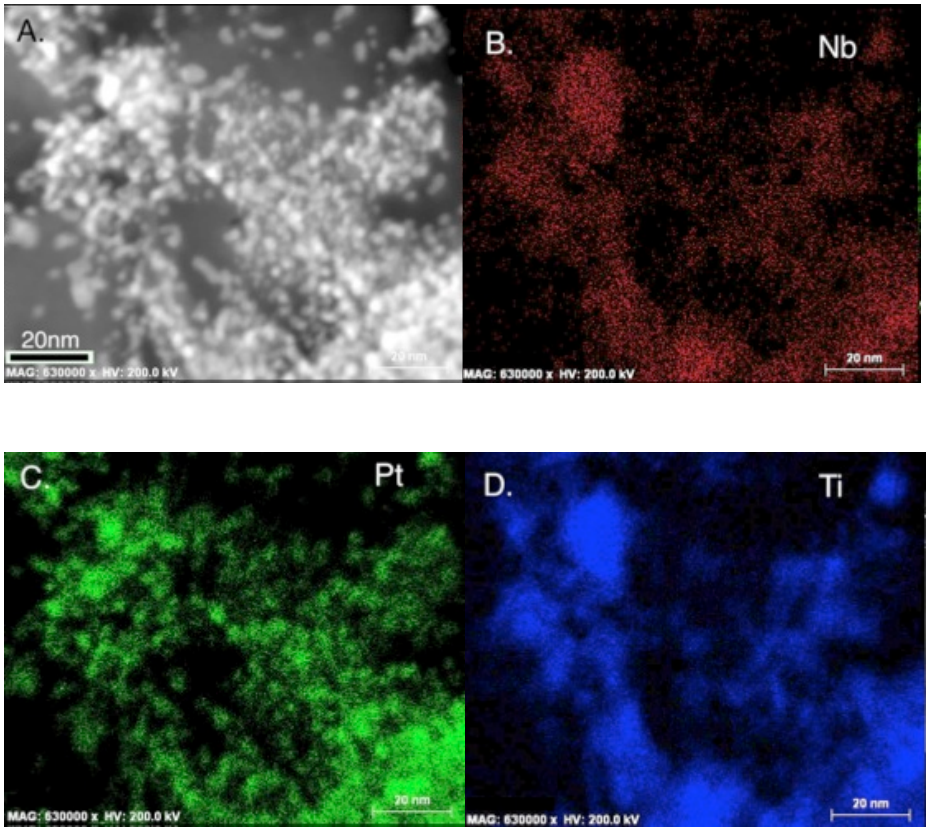

Figure 5-4 Elemental analysis over 10%Pt/20wt% Nb_2O_3+TiO_2/C. A) STEM image of the sample, and elemental maps of B) Nb, C) Pt, and D) Ti

5.3.2 Other complex supports

To provide further evidence of the unique structure of the network oxide layer and distribution of the loaded Pt nanoparticles, comparable studies were conducted over different samples with various complex supports including Pt(10%)–based catalysts on (10wt%Ta_2O_5+TiO_2)/C, Ta_2O_5/C and (20wt%WO_3+TiO_2)/C (C=Vulcan) supports.

The overview of the catalyst with support of (10wt%Ta_2O_5+TiO_2)/C at relative low magnification in the BF TEM mode is shown in the Figure 5-5, indicating that large number of catalyst particles is uniformly distributed on the carbon-oxide support.

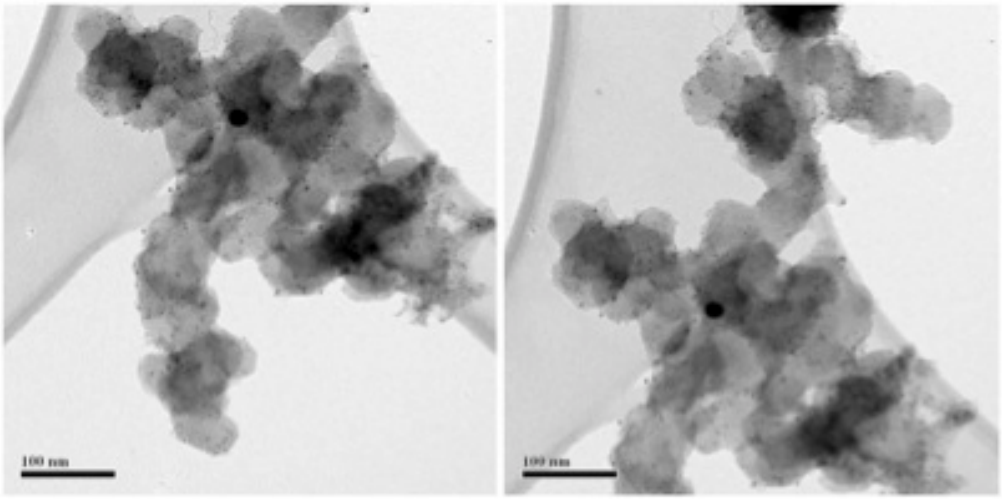

Figure 5-5 Overview of the sample Pt(10%)–based catalysts on C/(10%Ta_2O_5+TiO_2) at relative low magnification in bright field mode.

Further observations were carried out on the same samples by recording the high-resolution STEM HAADF and BF images, which provide further detailed information (Figure 5-6). STEM HAADF (Figure 5-6 A and B) and BF (Figure 5-6 C) observations of the sample along with elemental analysis indicate the hybrid oxide on carbon support exhibits a network structure. The catalyst nanoparticles and support areas are identified as shown in Figure 5-6-A. Figure 5-6 B and C present the corresponding areas highlighted

in squares in Figure 5-6 A in HAADF and BF modes respectively. Furthermore, along with the elemental analysis presented further below, Figure 5-6 B provides the evidence that the "network" structure is composed of disordered clusters where heavy single atoms of the transition metal network are visible as pointed out using white arrows in the image.

Elemental analysis is performed over the sample area shown in Figure 5-7-A using EDX measurements, which provide information related the elemental distribution of the sample. EDX spectra SP1 to SP3 in Figure 5-7 B show the point elemental analysis over three different areas of the sample including the catalysts nanoparticle and the network regions. Corresponding areas for EDX acquisition are labeled as shown in Figure 5-7 A. It is observed that the elements of Ti, O and C were detected from the network areas; while the rest of the areas mainly contained C. Moreover, it was also found that the Pt catalyst nanoparticles appeared preferentially within the Ti-O rich areas rather than the carbon rich areas, this being indicative of the stronger interaction between Pt and the transition metal oxide compared to the interaction with the carbon support.

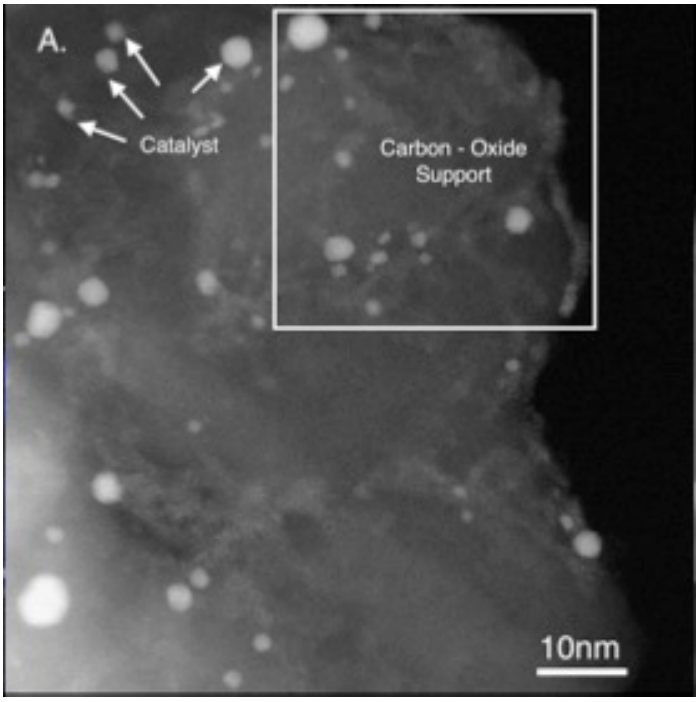
A.
Catalyst
Carbon - Oxide
Support
10nm

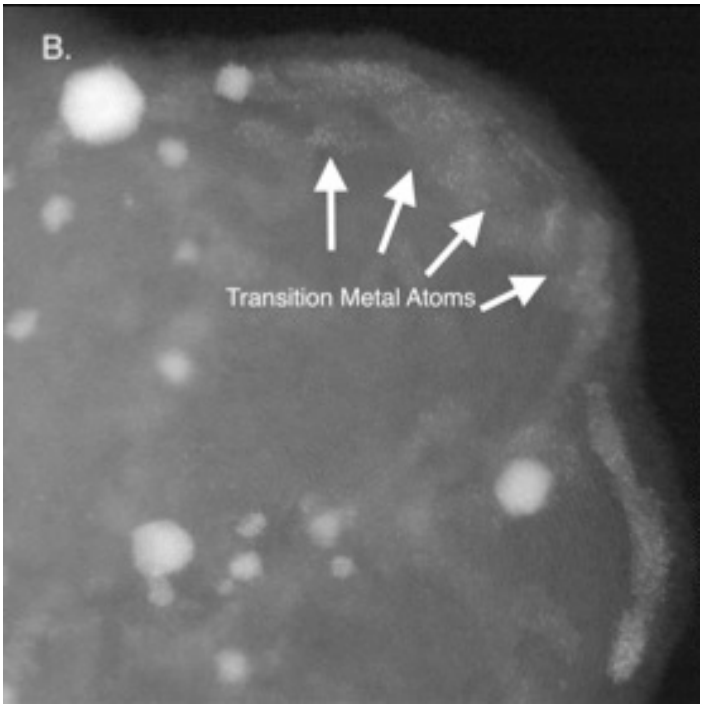
B.
Transition Metal Atoms

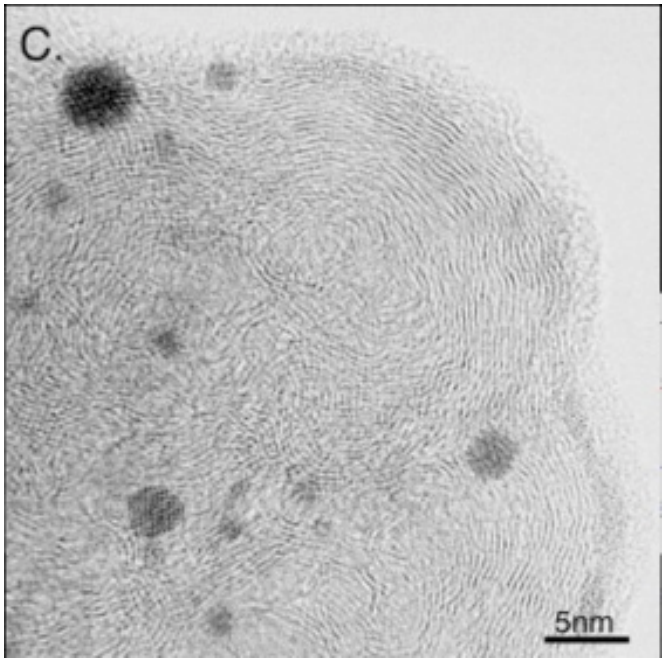

Figure 5-6 A STEM HAADF images of the catalyst sample with catalyst particles pointed out using white arrows; B and C: High resolution STEM HAADF and BF images of the corresponding highlighted area in A, clusters with single heavy atoms of the transition metals oxides are pointed out using white arrows

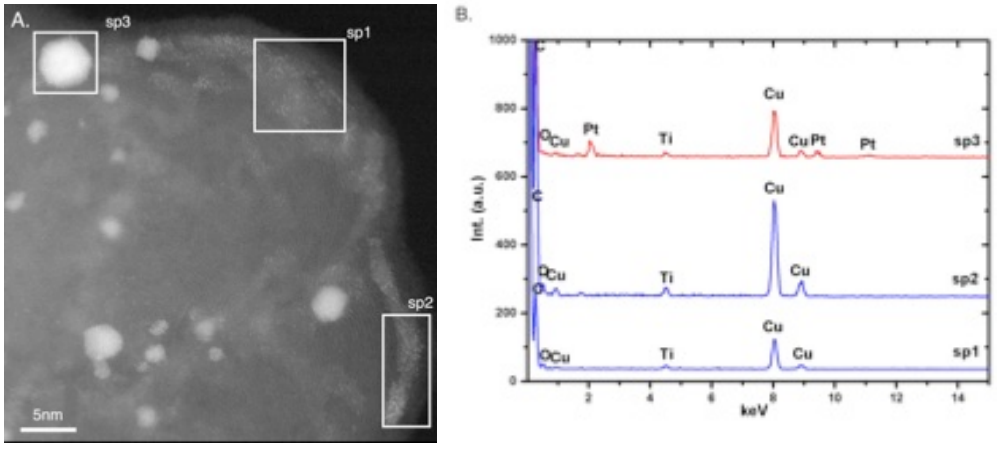

Figure 5-7A. STEM HAADF image of the sample with areas for elemental analysis highlighted in color squares; B: EDX spectra of corresponding areas. The Cu signal is from the TEM grid

This morphology of an oxide network with Pt particles appears to be general as shown in STEM HAADF and BF images obtained from different areas of the sample containing Pt(10%)–based catalysts on Ta_2O_5/C as shown in Figure 5-8 A to D. This again presents a highly interconnected network structure in the catalyst support layer, with the catalyst nanoparticles distributed on the surface of the hybrid support material. High-resolution observations of the corresponding highlighted areas provide evidence that the network structure is also formed and that it is similar compared with the C/(10%Ta_2O_5+TiO_2) support. In addition, the EDXS measurements provide confirmation that the areas identified with white arrows (Figure 5-9) correspond to the Ta-O rich atomic clusters making up the network structure. EDX spectra generated from different areas of the sample, Figure 5-10-B, show the variation of the chemical composition within the Pt catalyst loaded C/Ta_2O_5 sample. The corresponding areas used for EDX acquisition are highlighted in Figure 5-10-A. Based on the EDX analysis, it is obvious that the catalyst nanoparticles are more uniformly distributed on the surface of the oxide-rich area, or embedded within, of the support material rather the carbon rich area. This is further evidence of the stronger interaction between Pt catalyst particles and the transition metal oxide rich areas within the support.

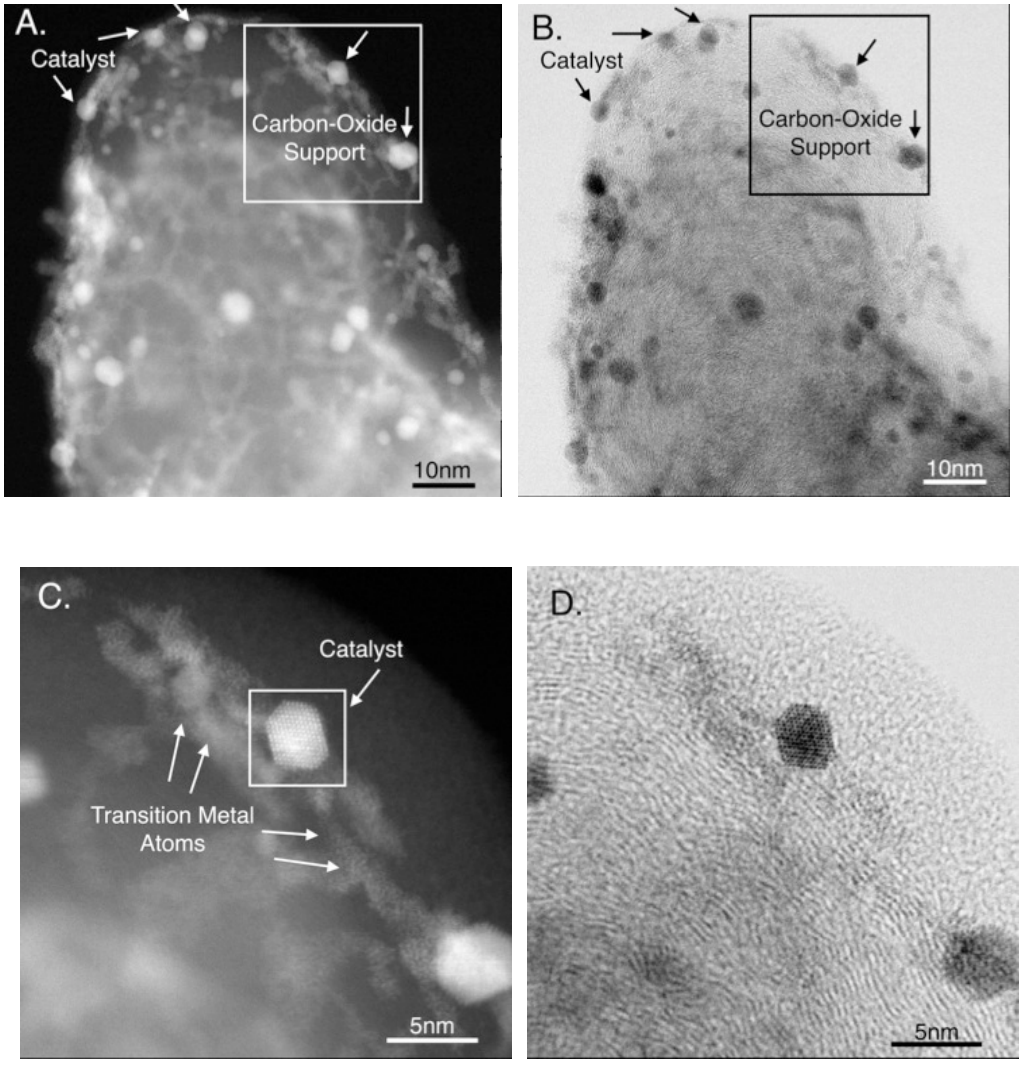

Figure 5-8 STEM HAADF and BF images taken at different areas of the sample, catalyst particles were pointed out using white or black arrows and Ta-O rich atomic cluster area were highlight using white arrows: C and D: High resolution STEM images of the highlighted area in A and B

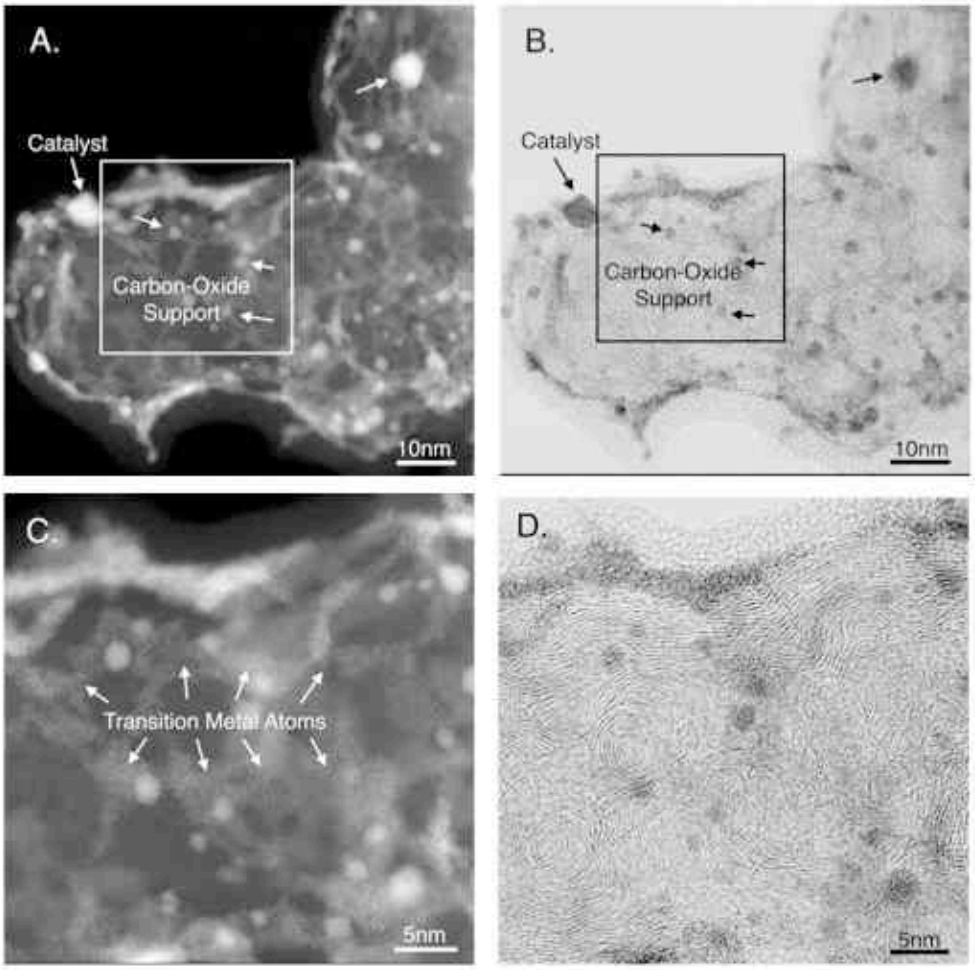

Figure 5-9 STEM HAADF and BF images at higher resolution obtained from different areas of the sample containing Pt(10%)–based catalysts on Ta_2O_5/C. A and B: STEM HAADF and BF images showing the corresponding areas highlighted using squares in C and D

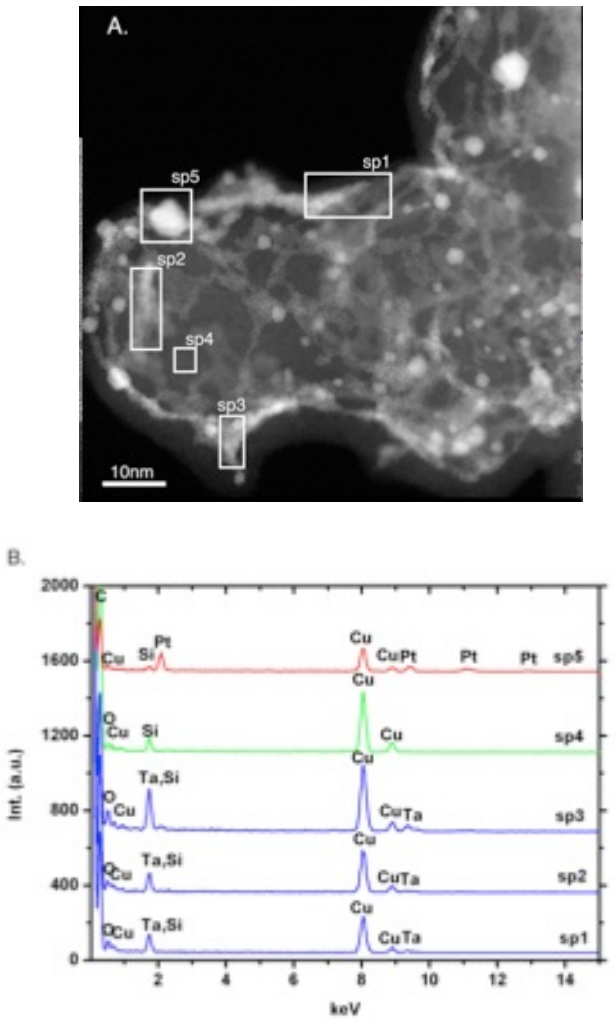

Figure 5-10 STEM HAADF image showing the corresponding areas for EDX acquisition, B: EDX spectra generated from various locations of the sample with 10%Pt catalyst loading

Elemental mapping has been carried out on several other samples (Figure 5-11) and confirms the correlation between the location of the Pt nanocatalysts and the support with systematic correlation between the location of the oxide and the location of the particles (Figure 5-12)

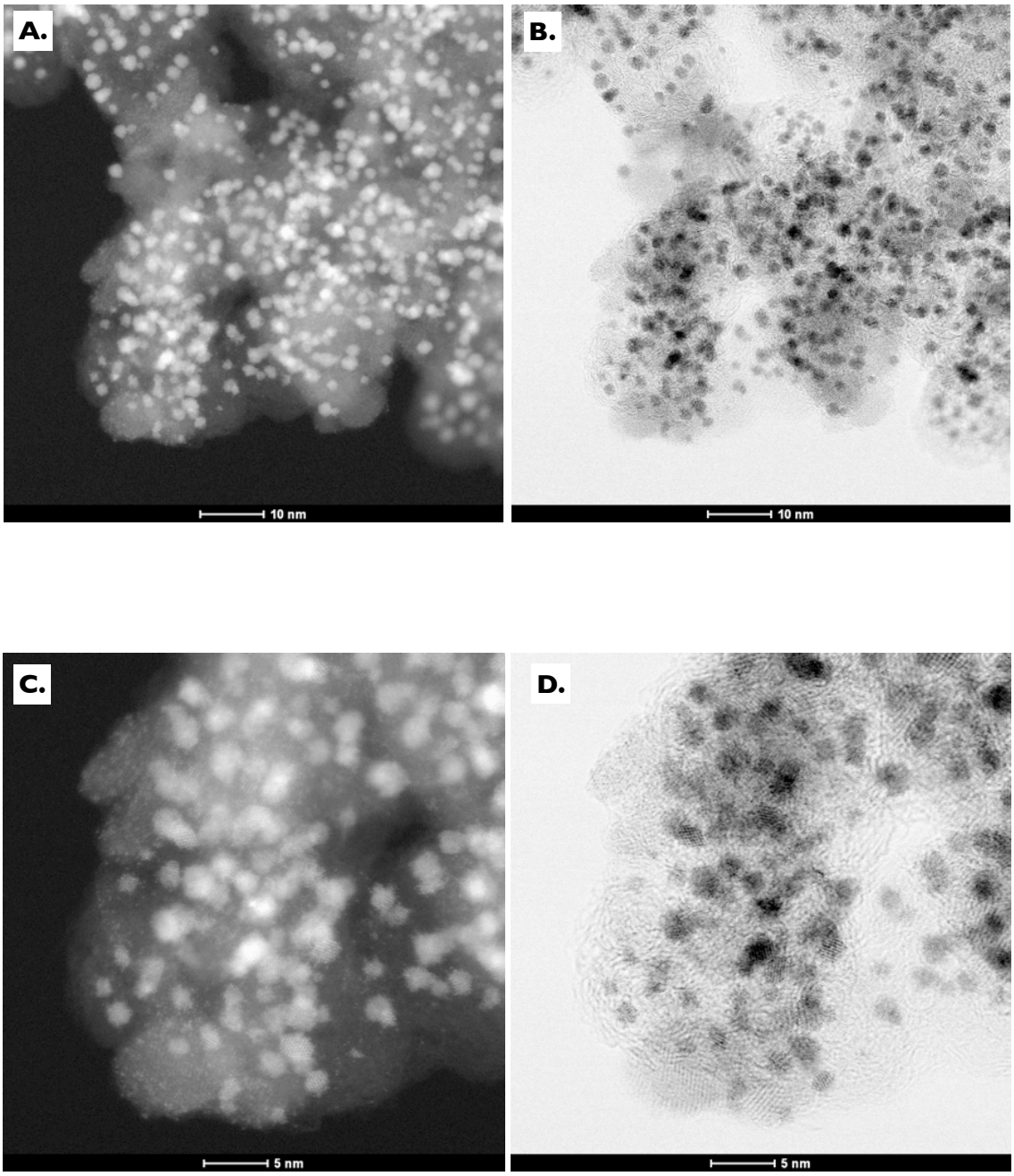
A.
10 nm
B.
10 nm
C.
5 nm
D.
5 nm

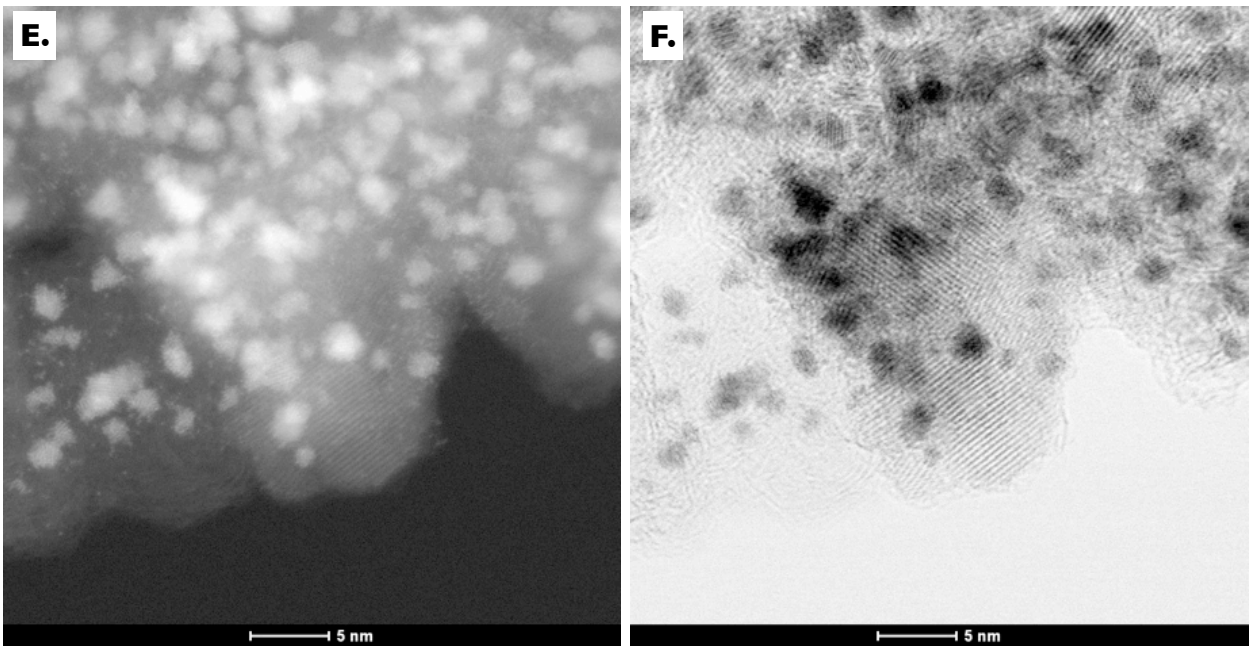

Figure 5-11 STEM HAADF and BF observation is also conducted on other catalyst system including 10wt%Pt/(20wt%WO_3+TiO_2)/C

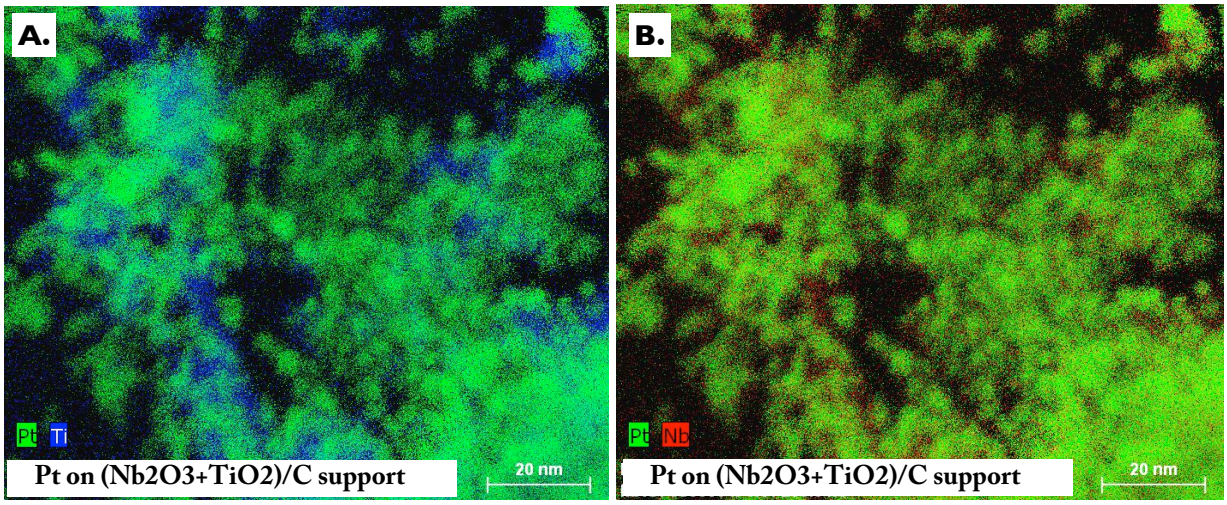

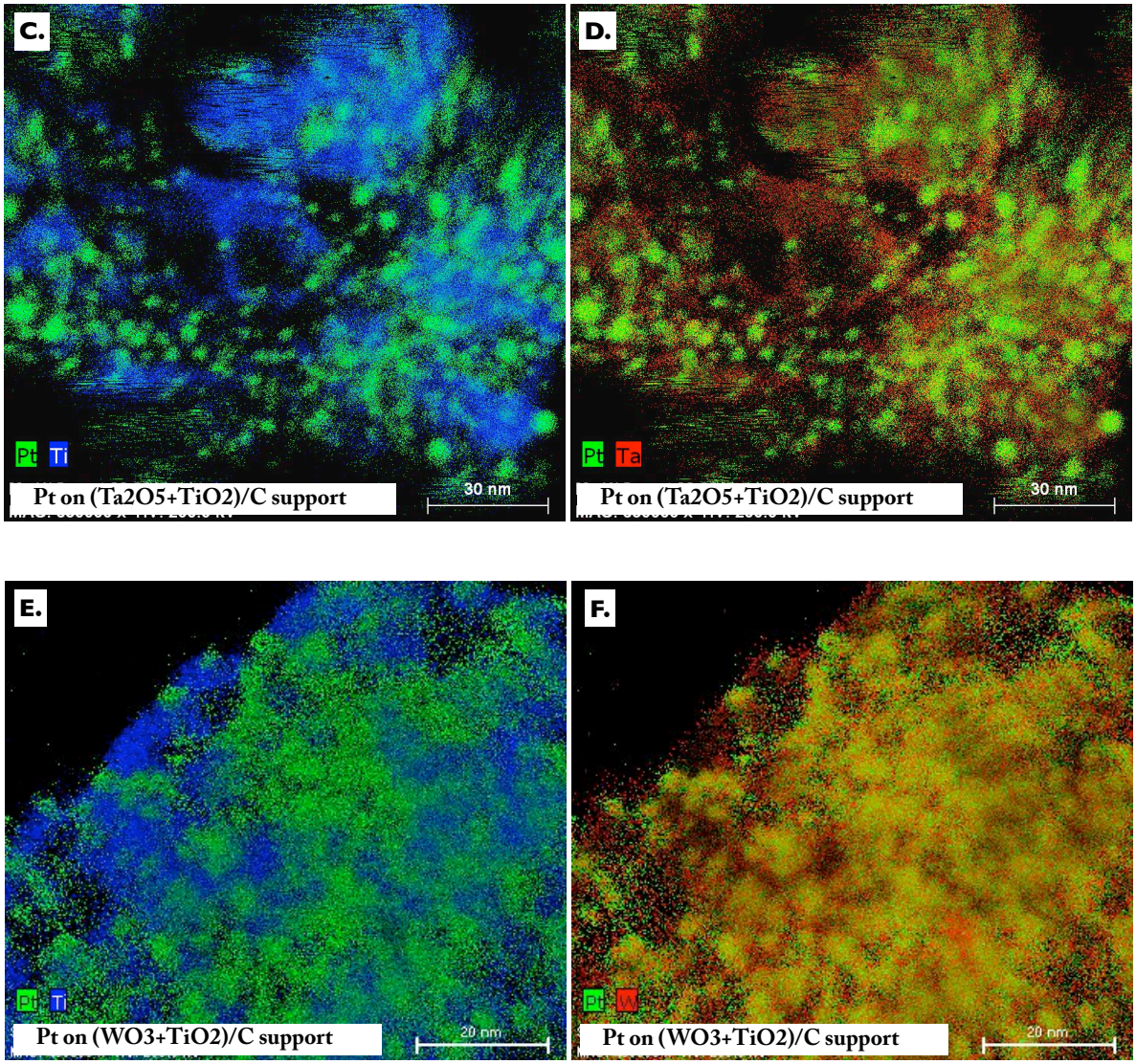

Figure 5-12 Comparable mapping results over different supports

5.3.3 3D structure of the catalyst

Electron tomography was used to further demonstrate the relative arrangement of the Pt and oxide support material. To provide further evidence of the morphology and the Pt nanoparticle distribution on the complex support and to ensure no information could be attributed to the overlapping structures projected in 2D, STEM HAADF tomography was applied to selected catalyst – support particles (diameter of about 150 nm). Here segmentation based on the intensity of the HAADF signal was done so as to differentiate the oxide network from the catalysts particles. From the reconstructed volume of the particle (Figure 5-13) we clearly observe that the Pt nanoparticles are well embedded or on the surface of the oxide layer. Further snapshots from different views of the reconstructed volume are shown in Figure 5-14 B to G.

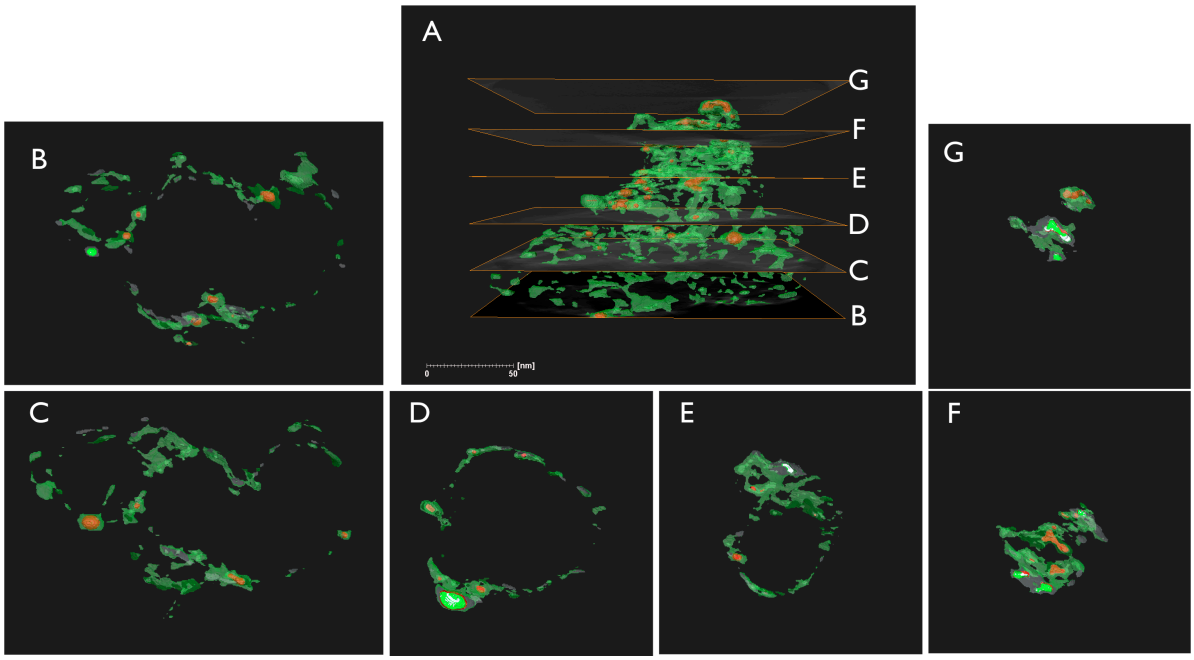

Figure 5-13 STEM HAADF tomography reconstruction of one of the catalyst particles: the green structure is the oxide support while the red particles are the Pt catalysts. A) overview of the full tomogram, B to G are the respective slices identified in A.

5.3.4 SMSI effect studied by EELS

High-resolution electron energy loss near edge structure spectra acquired over the hybrid support material (Figure 5-14A) shows a broad Ti L_{23} edge consistent with Magnéli phases, based on the reference spectra of standards (Ref 42). This phase on the carbon support would have high conductivity. Following subsequent loading of Pt on the same sample, the TiL_{23} edge is dramatically different (Figure 5-14). However, the features in the spectra do not exactly correspond to that of the precursor (Magneli phase

Ti_4O_7). The spectra are consistent with the presence of Ti^{4+} but also likely indicative of disorder as the features are broader than the spectra of crystalline anatase, rutile or brookite. This is consistent with HAADF images showing the disordered network. The spectra can also be indicative of TiO_2 phases, thus very defective and, based on the spectra and lack of reference of TiPt intermetallics, we cannot exclude the presence of $TiPt_3$ at the interface between titania and Pt since the spectra are averaged over large fields of view containing the oxide network and Pt particles embedded within it.

In order to elucidate the origin of the change in oxide nature and role of Pt in this transformation, as compared to possible environmental effects due to the synthesis steps related to the deposition of Pt, several experiments were carried out. Heat treatment under various conditions were applied to the pure support sample of (Nb_2O_3+TiO_x) / C. Samples were heat treated at 250°C, close to the temperature used during the synthesis condition, respectively in air and H_2 flow. The corresponding results show that there is no significant change of the valence of the Ti (Figure 5-15). Increasing the temperature from 250°C to 400°C, typical of the treatment condition in studying SMSI effect, [42] only causes very minor changes in the Ti edge present while the sample treated in the air flow at 400°C indicate a change consistent with the presence of Ti^{3+} but similar to an order structure and valence consistent with the presence of Nb.[127] None of the reference experiments provide such strong changes in the fine structure of the TiL23 edge in the Pt loaded on the hybrid TiO_x on carbon. These conditions would be strongly oxidizing TiO_x

to TiO_2 (Ti^{3+} to Ti^{4+}) and thermodynamically favored considering the possible presence of minute impurities in the hydrogen supply even to the ppm level of oxygen and water. According to the above experiments, the drastic change of the electronic structure of the oxide layer is therefore not due to the heat treatment involved during the sample synthesis, but is rather related to the Pt loading which induced SMSI effect and kinetically lowers the energy barrier of oxidizing Ti^{3+} to Ti^{4+} of the support. This electron interaction has been postulated to result in the stabilization of the Pt particles on the oxide network and leads to higher stability and durability of the fuel cell catalyst layer. Therefore, two roles are played by the pure support: the oxide network provides the medium to stabilize the Pt nanoparticles while the carbon support contributes more by conducting electrons. Such catalyst system will be one of the best catalyst candidates for fuel cell or other energy conversion applications due to their improved balance between the stability and performance.

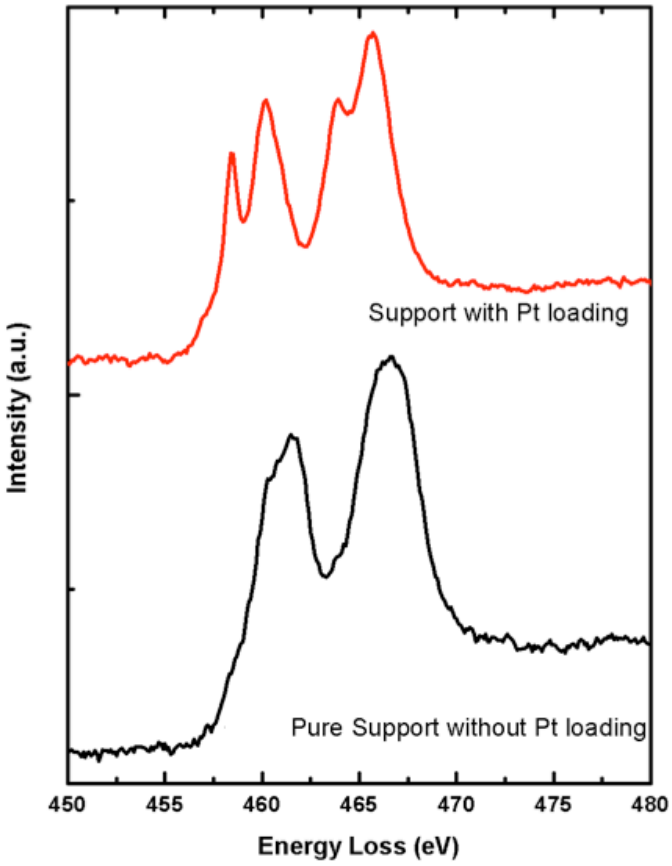

Figure 5-14 EELS spectra regarding the oxide structure of the catalyst before (black line) and after Pt loading (red line)

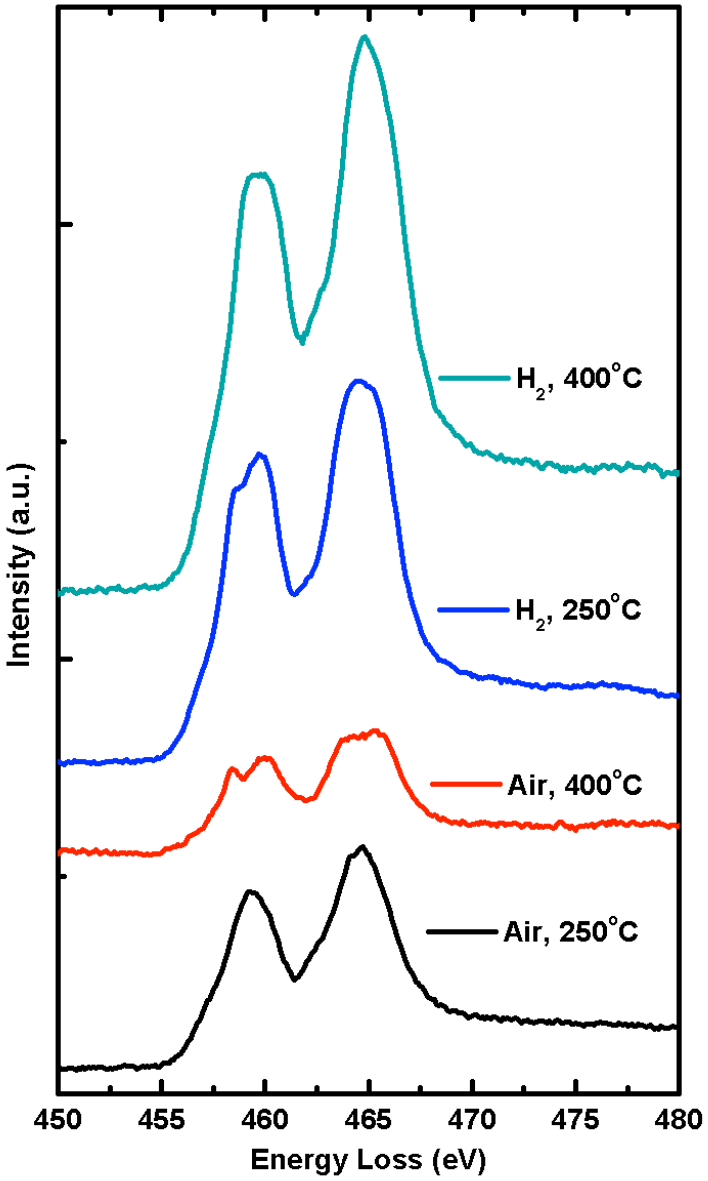

Figure 5-15 Ti L_{23} EELS spectrum of the support oxide structure of the catalyst treated at different conditions

Here, we clearly observe that this interface exists as the Pt is surrounded by the oxide, embedded or over it. This would lead the necessary conditions for the Tauster theory to apply whereby there is an interphase, the intermetallic phase $TiPt_3$, thus Brewer's hypo-hyper-d-d-interelectronic bonding present. In terms of magnitude of this electron transfer, however, given the loading of Pt and the fraction of the oxide in contact with the Pt catalysts, it appears that a large scale electron transfer cannot be detected, since our measurements at high energy resolution, do average over much more oxide than that is available at the interface between Pt and TiO_x. The fraction of interface atoms would be very small given the amount of oxide present. This observation from EELS is consistent with XPS data of the TiO_x-Nb_2O_5 showing a Ti^{4+} contribution but the change induced from the Pt addition is much strongly put into evidence here. Here, based on references of pure compounds of TiO_2 (i.e. pure anatase, rutile or brookite), it is clear that the spectra in Figure 5-14 cannot be solely attributed to pure TiO_2. Thus we cannot exclude that the TiL_{23} edge can contain additional contributions due to electron transfer from the Pt electrons. A pure sole electron transfer from Pt to the Magneli phase, however, would not be consistent with the observation since there is clearly an increase of the Ti valence. Thus the catalytic effect of Pt in the oxidation of Ti appears to dominate.

5.4 Conclusion

In the present work, Pt catalyst supported on complex oxide and carbon support have been synthesized by the sol-gel methods and show improved stability, electron conductivity, and catalytic properties.[124,125] Scanning Transmission Electron Microscopy (STEM) high angle annular dark-field (HAADF) (also known as Z-contrast) imaging was used to obtain structural details down to atomic scale. Elemental distribution of different components of the catalyst layer are tracked with imaging and analytical methods: from noble metal catalyst with higher atomic number to the lower atomic number support using high resolution energy dispersive X-ray spectrometry (EDXS). In addition, the STEM HAADF tomography characterization was applied to gain relevant information on preferential distribution of the catalyst on the supports in three dimensions (3D). In addition, using electron energy loss spectroscopy (EELS), the electronic structure of the catalyst support under various conditions was also studied to provide further evidence of the strong metal support interaction effect.

Based on scanning transmission electron microscopy, we have observed a strong interaction, between Pt and hybrid supports of various oxides ($Pt/Nb_2O_3/C$, $Pt/Ta_2O_5)/C$, $Pt/(Nb_2O_3+TiO_x)$ /C, $Pt/(Ta_2O_5+TiO_x)$ / C, $Pt/(WO_3+TiO_x)/C$). This interaction is based on the presence of an interconnected oxide network over the carbon support and the presence of Pt strongly connected to the oxide network. Evidence from

energy dispersive X-ray spectrometry and HAADF images and 3D electron tomography show that the Pt particles are either embedded, surrounded or on top of the oxide while practically no Pt is directly supported on the carbon in isolation. We have also observed strong interaction, and catalytic effects of the Pt with the oxide network indicating that the Pt role and interaction is broad ranging and not simply localized to only the interface Pt/Transition metal.

These results have been analysed and discussed in terms of the Brewer theory and SMSI effect and extent of electron transfer from Pt to the transition metal, as reflected in the case of TiO_x hybrid support.

Chapter 6. STEM HAADF Tomography for probing 3D structure of the catalysts

Utilization of effective catalysts comparing with commercial available ones is key approach to meet the new requirements of fuel cells. The controllable nanostructure, particle size, morphology, and/or porosity of the catalysts can increase the number of catalytically active sites, significantly improving the catalytic activity during the fuel cell cycling. It is well known that the chemical composition and structure of a catalyst can significantly affect its catalytic activity and performance. In packed and dense catalyst structures that do not have a periodic 3-dimensional (3D) arrangement, conventional characterization in 2-dimensional projections in (S)TEM do not fully represent the true structure of the sample. The STEM HAADF tomography technique introduced in below published paper provided the possibility to gain further relevant information on volume and morphology of catalyst materials in 3D.

DOI: 10.1002/cctc.201000403

STEM HAADF Tomography of Molybdenum Disulfide with Mesoporous Structure

Feihong Nan,[a] Chaojie Song,[b] Jiujun Zhang,[b] Rob Hui,[b] Jinwen Chen,[c] Craig Fairbridge,[c] and Gianluigi A. Botton*[a]

A highly ordered mesoporous molybdenum disulfide has been developed for catalysis in heavy oil refining. The morphology, structure, and composition of the material have been systematically characterized with advanced electron microscopy techniques. Scanning transmission electron microscopy with high-angle annular dark field tomography has been used to investigate the porous structure to give spatial information on the nanometre scale, and offer a direct view of individual porous particles in three-dimensions. The pore-size distribution, connectivity of the pores, and the mesoporous surface area have also been analyzed and offer useful information towards catalyst design.

Introduction

Transition metal chalcogenides have been commercially used in the petroleum refining industry to reduce the sulfur and nitrogen content in heavy oil for several decades.[1–3] Owing to accelerated demand and consumption of energy, the availability of easy-to-access conventional light sweet crude oil is declining. The utilization of extra heavy crude oil is becoming more common. However, upgrading and refining heavy oil is more complicated and may emit more greenhouse gases and air contaminants, which result in more environmental concerns than light sweet crude oil. Severe emission restrictions require more environmental friendly fuels with much lower sulfur and nitrogen containing compounds. Therefore, utilization of more effective catalysts than those currently available is one of the most important approaches to meet the new requirements.[4,5] Nanostructured molybdenum disulfide (MoS_2) exhibits a distinct crystal structure with unique physical and chemical properties, and has attracted considerable attention, owing to its high activity in the hydrodesulfurization (HDS) process to produce clean fuel.[6] The controllable nanostructure, particle size, morphology, and/or porosity of unsupported MoS_2 catalysts can increase the number of catalytically active sites, significantly improving the intrinsic HDS catalytic activity.[7] Therefore, the synthesis of nanostructured unsupported MoS_2 has become a promising research direction. As one type of nanostructured materials, mesoporous MoS_2 has been prepared and it has exhibited higher catalytic activity toward hydrodesulfurization.[7] The high surface area, regular porous structure, and unique pore sizes facilitate the diffusion of reactants and decrease the residence time, enhancing its catalytic activity.[8–10]

It is well known that the chemical composition and structure of a catalyst can significantly affect its catalytic activity and performance. Analytical electron microscopy is a well known powerful research tool that can illustrate this information. To investigate the chemical composition and structure of the catalyst and their effect on the activity and performance, advanced electron microscopy methods are required. For example, analytical electron microscopy techniques have been used to directly probe the local information of the catalytically active site at atomic scales.[11,12] Similarly, elemental analysis by using energy dispersive X-ray spectrometry (EDXS) and electron energy loss spectroscopy (EELS) can reveal the composition and distribution of the elements at the sub-nanometre scale.[13–15]

In packed and dense catalyst structures that do not have a periodic 3-dimensional (3D) arrangement, such characterization is an additional challenge as 2-dimensional projections do not fully represent the true structure of the sample. As a result, new techniques providing 3-dimensional morphological information of the sample become essential.[16–19] Over the last decade, 3D-electron tomography has developed and is applied routinely in the study of macromolecules and cells in biology. However, a few challenges have hindered the widespread application and interest of this technique in materials science and engineering. Firstly, unlike typical biological samples with more complex structures, most inorganic materials have been generally well represented by 2D projections. More importantly, the conventional approach used in biology, namely bright-field (BF) tomography, is generally not suitable for crystalline specimens, owing to the non-monotonic intensity of images with orientation and radiation damage of the sample while ex-

[a] F. Nan, Prof. G. A. Botton
Department of Materials Science & Engineering, McMaster University
1280 Main Street West, Hamilton, Ontario, L8S 4M1 (Canada)
Fax: (+1) 905 521 2773
E-mail: gbotton@mcmaster.ca
[b] Dr. C. Song, Dr. J. Zhang, Dr. R. Hui
Institute for Fuel Cell Innovation, National Research Council of Canada
4250 Wesbrook Mall, Vancouver, British Columbia, V6T 1W5 (Canada)
[c] Dr. J. Chen, Dr. C. Fairbridge
CanmetENERGY, Devon, Alberta, T9G1A8 (Canada)

Supporting information for this article is available on the WWW under http://dx.doi.org/10.1002/cctc.201000403.

periments are carried out at high accelerating voltages.[20,21] To improve the performance of the BF tomography in resolving the catalyst structure in three dimensions, electron tomography in low-voltage aberration corrected bright-field has been developed to reduce the effects from nonlinear dynamic diffraction.[17,19] Moreover, in recent years, extensive work has shown that, contrary to BF images, high-angle annular dark-field (HAADF) scanning TEM images, formed by using a scanned focused probe, provide the minimum contrast changes associated with coherent diffraction effect on crystalline samples. In fact, the intensity of STEM HAADF images varies monotonically both with atomic number and specimen thickness, thus making them ideal for the electron tomography reconstruction.[16,18,20]

In the present work, crystalline MoS_2 with highly ordered porous structure was successfully synthesized and characterized by using common physical characterization techniques including X-ray diffraction (XRD) and N_2 adsorption. STEM characterization was performed over the MoS_2 samples by providing direct structural and chemical compositional analysis. In addition, the STEM HAADF tomography technique was applied to MoS_2 to gain relevant information on volume and morphology, and their 3D distribution within the individual particles so as to determine porosity, connectivity and pore-size distribution.

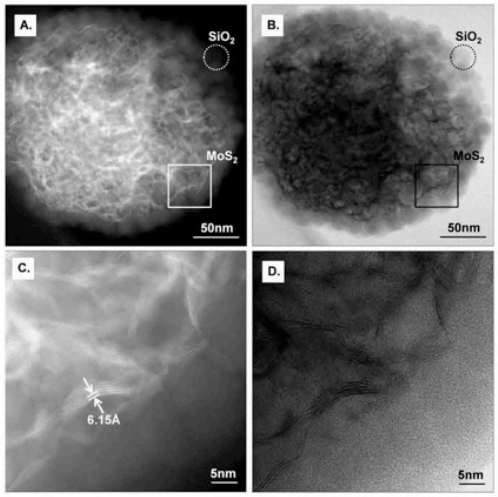

Figure 1. A and B) STEM HAADF and BF images of MoS_2 nanoparticles supported by silica templates at relatively low magnification; C and D) high resolution STEM HAADF and BF micrographs of MoS_2 nanocrystallites distributed inside the interstices of silica template spheres.

Results and Discussion

Physical characterization

The mesoporous material was synthesized by a two-step process whereby the MoS_2 forms within silica nanosphere (22 nm diameter) templates (see further details in the Experimental Section). As a second step, the product is subsequently etched in HF to remove the silica template with a resulting mesoporous MoS_2 structure. The MoS_2 product after HF leaching was characterized by using XRD and N_2 adsorption. XRD patterns showed 4 diffraction peaks at 14.1, 33.6, 40.0, and 59.4° corresponding to the 002, 100, 103, and 110 planes of MoS_2, respectively, in good agreement with the literature.[7] The (002) interplanar distances were found to be 6.23 Å, in close agreement with the value observed in the TEM. Analysis of the N_2 isotherm revealed a BET surface area of 221 m^2g^{-1} with a bimodal porous structure containing pore sizes of 5.8 nm and 18.4 nm, both in the mesopore-size range. The pore size of 5.8 nm was formed from the stacking of the MoS_2 plates on the silica nanospheres, and that of 18.4 nm was from the leaching of the silica template. Template removal might result in shrinking in pore size, forming smaller pores than the template particle size. The pore volume of the material was found to be 0.75 cm^3g^{-1}

HRTEM and EDXS analysis

Following the growth of MoS_2 in the silica template, STEM HAADF (Figure 1A and C) and BF (Figure 1B and D) observations along with the elemental analysis indicate that the templates possess a highly packed structure. MoS_2 crystallites with plane stacking of 4–10 layers are observed. The circular and rectangular areas highlighted in Figure 1A and B correspond to the template sphere and molybdenum disulfide nanocrystallites, respectively. High-resolution images (Figure 1C and D) of the highlighted rectangular area in Figure 1A and B present a layer spacing close to 6.15 Å, which corresponds to the d_{002} of MoS_2, which is consistent with the XRD measurements. Such observations were repeated several times on different particles, giving clear evidence for the presence of MoS_2 nanocrystallites inside the interstices of silica template spheres, which were also confirmed by elemental mapping results (Figure 2).

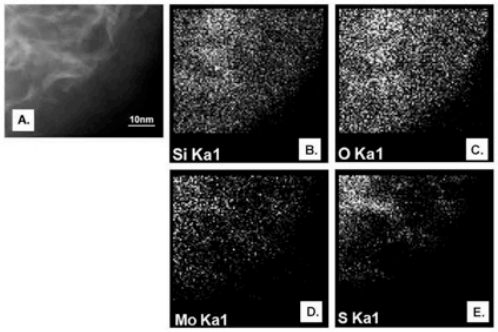

Figure 2. EDXS elemental maps of the MoS_2 grown in the silica templates. A) The STEM image and its corresponding elemental maps of B) Si, C) O, D) Mo, and E) S.

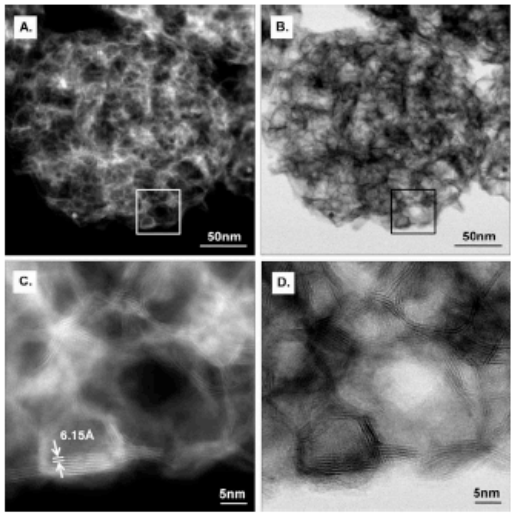

Figure 3. A and B) Overview of the MoS_2 particles at relatively low magnification, after removal of SiO_2 by HF, by using STEM HAADF and bright-field STEM modes, respectively; C) STEM HAADF micrograph of MoS_2 nanoparticles with a highly ordered mesoporous structure; D) detailed view of selected area in BF STEM mode.

STEM observations of the molybdenum disulfide catalysts after the removal of the silica template using HF provide evidence for the presence of a highly dispersed MoS_2 phase with mesoporous structure (Figure 3). The lattice fringes due to the MoS_2 crystallites with 6.15 Å (002) interplanar spacing were clearly observed (Figure 3C and D). Analysis of the elemental mapping (Figure 4) reveals the homogeneous distribution of

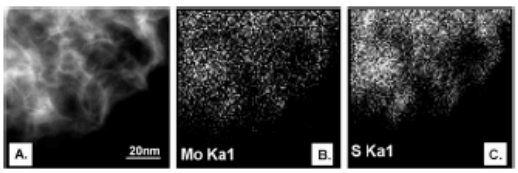

Figure 4. Elemental analysis over MoS_2 after removal of the SiO_2 templates using HF. A) STEM image, and the elemental maps of B) Mo and C) S.

Mo and S. To consider the effect from the overlapping of the S_K and Mo_L EDXS peaks, the $S_{K\alpha}$ and $Mo_{K\alpha}$ lines were selected for the elemental data acquisition and compared. Differences in the S map, as compared to the Mo map, would indicate changes in local Mo/S ratio. EDXS microanalysis performed over several areas revealed that both molybdenum and sulfur were uniformly distributed throughout the sample and that Si, O, and F were not detected (see the Supporting Information).

STEM HAADF tomography

To provide further evidence of the connectivity and the pore-size distribution and to ensure no information could be attributed to the overlapping structures projected in 2D, STEM HAADF tomography was applied to one of MoS_2 particles (diameter of about 500 nm). From the reconstructed volume of the particle (Figure 5) we can observe that the pores inside the

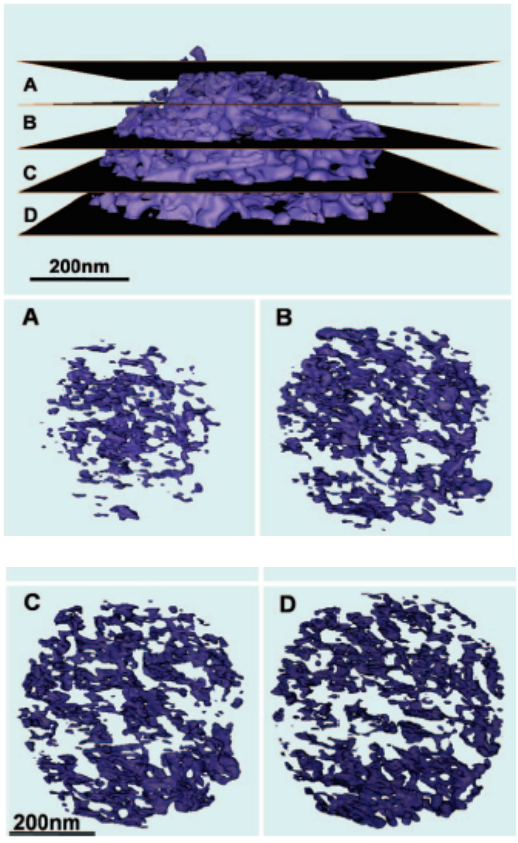

Figure 5. STEM HAADF tomography reconstruction and slice view corresponding to the different locations of a MoS_2 mesoporous particle.

particle are highly interconnected and extend to the surface of the catalyst grain. The size distribution of the pores ranges from 5 nm to 50 nm with a minimal bottleneck diameter of about 5 nm. The opening pores on the particle surface are between 10 nm and 50 nm, thus providing the *meso*-channels to allow heavy crude oil molecules to reach the active sites.[22]

The total surface area (external and internal) of the corresponding particle shown in Figure 1, calculated by counting the voxels of the surface material in contact with the vacuum, was 7.80 μm^2. The volume of the same particle calculated by counting the voxels inside the particle material was 2.46×

10^7 nm^3. From these two measurements based on the tomography reconstruction and the bulk density values of MoS_2, we calculated that a specific surface area of 64.4 m^2g^{-1} for this individual particle. Even though these values are in the same order of magnitude as the value obtained for BET (221 m^2g^{-1}), they are significantly lower. The main origin to this difference is likely related to the contribution of the micropores with sizes smaller than 2 nm, that is, smaller than the resolution of the reconstructed volume, 2.4×2.4×2.4 nm (the size of a single voxel). However, the local tomography measurements are in good agreement with the presence of mesopores of 5.8 nm and 18 nm diameter from N_2 adsorption measurement with the pore-size distribution calculated using the measurement applied to tomography reconstruction volume (Figure 6).

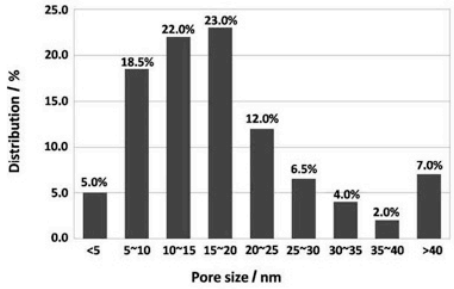

Figure 6. The pore-size distribution of a MoS_2 mesoporous particle.

In addition to the surface area calculation, the distribution of surface area and connectivity of the pores within different regions of the particles can also be calculated (Figure 5). These local measurements from tomography enable the direct visualization of complex structures not possible by other characterization techniques.

Conclusions

STEM HAADF and BF images combined with electron tomography reconstruction have enabled the investigation of molybdenum disulfide catalysts for heavy oil refining. Local measurements of surface area have been performed based on tomographic measurements and have been compared with macroscopic BET data that provides active surface area measurements. The tomography technique also provided information on the structure of the MoS_2 catalyst, in terms of the connectivity of the mesopores, and gave insight into the accessibility of reactant molecules to the inner regions of the particles. Furthermore, the shapes of the pores, the pore volume, and the mesoporous surface area of particles were quantified. Two-dimensional HRTEM characterizations gave evidence of the existence of the mesopores within the crystalline MoS_2. A uniformly distributed mesoporous structure was described according to the elemental analysis by using EDXS.

This information on the pore connectivity provides useful insight into the efficiency and catalytic activity of these materials for cracking of heavy crude oil.

Experimental Section

Synthesis of MoS_2: MoS_2 was synthesized by using ultrasonic spray pyrolysis (USP) according to a literature procedure.[7] First $(NH_4)_2MoS_4$ (2.08 g) was dissolved in deionized water (100 mL), followed by the addition of SiO_2 (6 g, 22 nm) colloid solution. The mixture was then diluted to 200 mL, and stirred for 1 hour. The solution was then loaded into the USP system. The pyrolysis temperature was controlled at 700 °C, and the argon flow rate was 5 $L min^{-1}$. The product was collected, recovered by filtration, and air dried. The silica template was removed by soaking the product in a 10% HF ethanol solution for 24 h.

Physical characterization of MoS_2: The XRD measurements were performed by using a Bruker D8 X-ray diffractometer equipped with a graphite monochromator and a vertical goniometer with $Cu_{K\alpha}$ radiation. The specific surface area measurement was performed by the BET method in a surface area analyzer (SA3100, Beckman Coulter).

HRTEM imaging and EDX analysis: STEM HAADF and BF imaging were applied to the analysis of molybdenum disulfide samples. Samples for STEM observations were directly supported on a copper mesh with a porous carbon film. Observations in STEM mode were performed by using a FEI Titan 80–300 Cubed transmission electron microscope equipped with a CEOS-designed hexapole-based aberration corrector for the image-forming lens and one for the probe-forming lens and operated at an accelerating voltage of 200 kV. The instrument was also equipped with a Gatan Imaging Filter (GIF) for energy-filtered imaging and an energy dispersive X-ray detector (Oxford Instruments, Inca system) for elemental analysis and mapping.

STEM HAADF tomography: In this work, the tilt series were recorded in the STEM HAADF mode. HAADF-STEM images were acquired by using a FEI Titan 80–300 field emission gun transmission electron microscope operated at 300 kV and with a Fischione high-tilt tomography sample holder. Images were taken with a tilt range from −75 to 70°, and a 2° increment between −50 to 50° and a 1° increment elsewhere. The tilt series without specimen self-shadowing consisted of 95 images. The FEI software package Xplore3D Acquisition was used to control the tilt angle, to maintain the object within the field of view, to correct for focusing, and to record and store 2D images at different tilting angles. Tomographic reconstruction was carried out with the FEI Inspect3D package and visualization as well as the calculation of the reconstructed volume was achieved by using the Amira4.1 package.

Acknowledgements

This work was funded by the Government of Canada's Program for Energy Research and Development, PERD 1.1.3, Petroleum Conversion for Cleaner Air, the Institute for Fuel Cell Innovation, National Research Council Canada, and McMaster University. GAB is grateful to NSERC for funding this project via a strategic grant. Electron microscopy work presented here was carried out at the Canadian Centre for Electron Microscopy, a facility supported by NSERC and McMaster University.

Keywords: EDX spectroscopy · transmission electron microscopy · mesoporous · molybdenum · tomography

[1] R. Nava, J. Morales, G. Alonso, C. Ornelas, B. Pawelec, J. L. G. Fierro, *Appl. Catal. A* **2007**, *321*, 58.
[2] R. Romero-Rivera, A. Del Valle, G. Alonso, E. Flores, F. Castillon, S. Fuentes, J. Cruz-Reyes, *Catal. Today* **2008**, *130*, 354.
[3] T. A. Zepeda, B. Pawelec, A. Olivas, J. L. G. Fierro, *Mater. Res. Innovations* **2007**, *11*, 54.
[4] T. A. Zepeda, B. Pawelec, J. L. G. Fierro, T. Halachev, *Appl. Catal. B* **2007**, *71*, 223.
[5] K. Soni, B. S. Rana, A. K. Sinha, A. Bhaumik, M. Nandi, M. Kumar, G. M. Dhar, *Appl. Catal. B* **2009**, *90*, 55.
[6] S. T. Wang, C. H. An, J. K. Yuan, *Materials* **2010**, *3*, 401.
[7] S. E. S. a. K. S. Suslick, *J. Am. Chem. Soc.* **2005**, *127*, 9990.
[8] Y. F. Shi, Y. Wan, R. L. Liu, B. Tu, D. Y. Zhao, *J. Am. Chem. Soc.* **2007**, *129*, 9522.
[9] Z. D. Huang, W. Bensch, L. Kienle, S. Fuentes, G. Alonso, C. Ornelas, *Catal. Lett.* **2008**, *122*, 57.
[10] Z. D. Huang, W. Bensch, L. Kienle, S. Fuentes, G. Alonso, C. Ornelas, *Catal. Lett.* **2009**, *127*, 132.
[11] P. L. Gai, *Curr. Opin. Solid State Mater. Sci.* **2001**, *5*, 371.
[12] C. Kiely, *Nat. Mater.* **2010**, *9*, 296.
[13] Z. L. Wang, *Adv. Mater.* **2003**, *15*, 1497.
[14] S. Lazar, Y. Shao, L. Gunawan, R. Nechache, A. Pignolet, G. A. Botton, *Microsc. Microanal.* **2010**, *16*, 416.
[15] G. Botton in *Science of Microscopy, Vol. 1* (Ed.: J. C. H. S. Peter W. Hawkes), Springer, **2008**.
[16] J. M. Thomas, P. L. Gai, *Adv. Catal.* **2004**, *48*, 171.
[17] K. P. de Jong, L. C. A. van den Oetelaar, E. T. C. Vogt, S. Eijsbouts, A. J. Koster, H. Friedrich, P. E. de Jongh, *J. Phys. Chem. B* **2006**, *110*, 10209.
[18] I. Arslan, J. C. Walmsley, E. Rytter, E. Bergene, P. A. Midgley, *J. Am. Chem. Soc.* **2008**, *130*, 5716.
[19] M. Bar Sadan, L. Houben, S. G. Wolf, A. Enyashin, G. Seifert, R. Tenne, K. Urban, *Nano Lett.* **2008**, *8*, 891.
[20] M. Weyland, *Top. Catal.* **2002**, *21*, 175.
[21] P. A. Midgley, M. Weyland, T. J. V. Yates, I. Arslan, R. E. Dunin-Borkowski, J. M. Thomas, *J. Microsc.* **2006**, *223*, 185.
[22] O. Ersen, C. Hirlimann, M. Drillon, J. Werckmann, F. Tihay, C. Pham-Huu, C. Crucifix, P. Schultz, *Solid State Sci.* **2007**, *9*, 1088.

Received: November 14, 2010
Published online on March 2, 2011

Chapter 7. Conclusions and future works

The rational design and morphology control of PEMFC catalysts from fundamental principles has the potential to provide a great opportunity to improve their catalytic properties and increase their activity on a mass basis. However, understanding and direct evidence of the nanoparticle structures down to the atomic level is critical in determining the relationship with the catalytic activities in fuel cell applications.

Pt-based catalysts are considered as the most practical catalysts in current PEMFC technology for both anode hydrogen oxidation reaction (HOR) and cathode oxygen reduction reaction (ORR). However, impurities such as CO include within reformed hydrogen could be easily adsorbed on Pt particle surface and poison the anode catalyst layer, leading to significant fuel cell performance degradation. Bimetallic heterogeneous catalysts such as carbon-supported Pt–Ru alloy with core–shell structure (Ru@Pt) show enhanced CO oxidation activity when compared to PtRu alloy and monometallic Pt and Ru nanoparticle catalysts.

As presented in chapter 4, for current study of PtRu catalysts nanoparticles, our experimental results shown that the enhanced CO oxidation may be achieved through the interactions between the Pt shell and Ru core atoms, which can modify the electronic structure of the Pt surface by the presence of subsurface Ru atoms or by disrupting the Pt surface arrangement. This leads to decrease of the interaction strength of adsorbates on

the Pt surface atoms in Ru@Pt nanoparticles including weaker CO bonding on surface Pt atoms/Ru support, compared with Pt atoms on pure Pt particles. This modification may significantly destabilize CO on Pt, leading to a lower CO saturation coverage, thereby providing more free active sites for hydrogen oxidation reaction. Within the core-shell structure nanoparticles in current study, not only the shell is rich in Pt, the deviation of the Pt-lattice change is also detected. Furthermore, the possibility of presence of the compressive strain within the Pt rich shell is proved by the lattice measurements, which is likely one of the key factors that affect the catalytic activity. Strasser's computational study suggested the deviation of the Pt-shell is one of the controlling factors of electrocatalytic activity due to the change of the Pt 5d anti-bonding state.[117] Moreover, while replacing the conventional carbon support by titanium oxide, the morphology and distribution of the PtRu catalyst are significantly affected due to that.

Furthermore, Pt catalyst supported on complex oxide and carbon support synthesized by the sol-gel methods were studied to investigate the relationship between the catalyst and its support. According to STEM characterization results, we have observed a strong interaction, between Pt and hybrid supports of various oxides and carbon which include Nb_2O_3 / C, Ta_2O_5 / C, (Nb_2O_3+TiO_x) / C, (Ta_2O_5+TiO_x) / C, and (WO_3+TiO_x)/C). Observations from STEM images and HAADF and energy dispersive X-ray spectrometry show that preferential distribution of the catalyst on the supports, Pt particles are either embedded, surrounded or on top of the oxide while practically no Pt is

directly supported on the carbon in isolation. Such evidence indicates the interaction between the catalyst and support is based on the presence of an interconnected oxide network over the carbon support and the presence of Pt strongly connected to the oxide network. In addition, using electron energy loss spectroscopy (EELS), the electronic structure of the catalyst support under various conditions was also studied to provide further evidence of the strong metal support interaction effect.

The goal of current research is probing the relationship between catalyst features and the fuel cell performance. The study investigated different catalyst systems including core-shell structured catalyst, catalysts with unique carbon-transition metal oxide supports with the application of in-depth structural analysis, such as XRD, HRTEM, (S)TEM, and HAADF STEM tomography. Further works shown as below should be conducted in next step:

- In situ TEM observation should be applied to investigate the dynamic process and morphology variations of both catalysts and its support materials at the atomic scale.

- Catalysts with different size and shape should be prepared and studied in order to provide the route to control the morphology of the catalyst layer during the fuel cell operation.

- Comparable electron microscopy analysis should be used to investigate the changes of material microstructure and morphology under different synthesis routes and working cycles.

- Comparable study should be conducted between the catalyst systems of commercial available Pt/C, PtRu/C, Pt@Ru/C, and Pt@Ru/complex support.

- Fuel Cell testing should be conducted to compare the performance by using different complex support materials.

- Fuel Cell testing: the membrane electrode assemblies (MEA) should be prepared following the standard procedures, and its performance should be evaluated.

Bibliography

1. Eaves, S.; Eaves, J. A Cost Comparison of Fuel-Cell and Battery Electric Vehicles. *J. Power Sources* **2004**, *130*, 208–212.
2. Cheng, X.; Shi, Z.; Glass, N.; Zhang, L.; Zhang, J. J.; Song, D. T.; Liu, Z. S.; Wang, H. J.; Shen, J. A Review of PEM Hydrogen Fuel Cell Contamination: Impacts, Mechanisms, and Mitigation. *J. Power Sources* **2007**, *165*, 739–756.
3. Liu, H. S.; Song, C. J.; Zhang, L.; Zhang, J. J.; Wang, H. J.; Wilkinson, D. P. A Review of Anode Catalysis in the Direct Methanol Fuel Cell. *J. Power Sources* **2006**, *155*, 95–110.
4. Brandon, N. P.; Skinner, S.; Steele, B. C. H. Recent Advances in Materials for Fuel Cells. *Annu. Rev. Mater. Res.* **2003**, *33*, 183–213.
5. Biyikoglu, A. Review of Proton Exchange Membrane Fuel Cell Models. *Int. J. Hydrog. Energy* **2005**, *30*, 1181–1212.
6. Zhang, J. *PEM Fuel Cell Electrocatalysts and Catalyst Layers Fundamentals and Applications*; Zhang, J., Ed. Springer, 2008.
7. Jaksic, J. A.; Krstajic, N. V.; Vracar, L. M.; Neophytides, S. G.; Labou, D.; Falaras, P.; Jaksic, M. M. Spillover of primary oxides as a dynamic catalytic effect of interactive hypo-d-oxide supports. In; Pergamon-Elsevier Science Ltd, 2007; Vol. 53, pp. 349–361.
8. Krstajic, N. V.; Vracar, L. M.; Radmilovic, V. R.; Neophytides, S. G.; Labou, M.; Jaksic, J. M.; Tunold, R.; Falaras, P.; Jaksic, M. M. Advances in Interactive Supported Electrocatalysts for Hydrogen and Oxygen Electrode Reactions. *Surface Science* **2007**, *601*, 1949–1966.
9. Yoshida, K.; Kawai, T.; Nambara, T.; Tanemura, S.; Saitoh, K.; Tanaka, N. Direct Observation of Oxygen Atoms in Rutile Titanium Dioxide by Spherical Aberration Corrected High-Resolution Transmission Electron Microscopy. *Nanotechnology* **2006**, *17*, 3944–3950.
10. Ioroi, T.; Senoh, H.; Yamazaki, S. I.; Siroma, Z.; Fujiwara, N.; Yasuda, K. Stability of Corrosion-Resistant Magneli-Phase Ti4O7-Supported PEMFC Catalysts at High Potentials. *Journal of The Electrochemical Society* **2008**, *155*, B321–B326.
11. Liborio, L.; Harrison, N. Thermodynamics of Oxygen Defective Magneli Phases in Rutile: a First-Principles Study. *Phys. Rev. B* **2008**, *77*.
12. Barbir, F. *PEM Fuel Cells: Theory and Practice*; Barbir, F., Ed. 2005th ed. Elsevier Academic Press: New York, 2005.
13. Zhang, J. L.; Xie, Z.; Zhang, J. J.; Tanga, Y. H.; Song, C. J.; Navessin, T.;

Shi, Z. Q.; Song, D. T.; Wang, H. J.; Wilkinson, D. P.; *et al.* High Temperature PEM Fuel Cells. *J. Power Sources* **2006**, *160*, 872–891.

14. Zhang, L.; Zhang, J.; Wilkinson, D. P.; Wang, H. Progress in Preparation of Non-Noble Electrocatalysts for PEM Fuel Cell Reactions. *J. Power Sources* **2006**, *156*, 171–182.
15. Song, C.; Neburchilov, V.; Zhang, J.; Botton, G. Characterization of the Catalysts for PEMFC Using Aberration-Corrected Analytical Transmission Electron Microscopy. **2011**.
16. Liborio, L.; Mallia, G.; Harrison, N. Electronic Structure of the Ti_4O_7 Magnéli Phase. *Phys. Rev. B* **2009**, *79*.
17. Park, H. S.; Cho, Y. H.; Jung, C. R.; Jang, J. H.; Sung, Y. E. Performance Enhancement of PEMFC Through Temperature Control in Catalyst Layer Fabrication. *Electrochimica Acta* **2007**, *53*, 763–767.
18. Zhang, S.; Yuan, X.; Wang, H.; MErida, W.; Zhu, H.; Shen, J.; Wu, S.; Zhang, J. A Review of Accelerated Stress Tests of MEA Durability in PEM Fuel Cells. *Int. J. Hydrog. Energy* **2009**, *34*, 388–404.
19. Song, C.; Baker, R.; Hui, R.; Zhang, J.; Nan, F. Nanocrystalline Tungsten Carbide (WC) Synthesis/Characterization and Its Possible Application as a PEM Fuel Cell Catalyst Support. *Electrochimica Acta* **2011**.
20. Antolini, E.; Gonzalez, E. R. Ceramic Materials as Supports for Low-Temperature Fuel Cell Catalysts. *Solid State Ionics* **2009**, *180*, 746–763.
21. Vracar, L. M.; Gojkovic, S. L.; Elezovic, N. R.; Radmilovic, V. R.; Jaksic, M. M.; Krstajic, N. V. Magneli Phase Titanium Oxides as Catalyst Support - Electrochemical Behavior of Ebonex/Pt Catalysts. *Journal of New Materials for Electrochemical Systems* **2006**, *9*, 99–106.
22. Bracey, J. Enhanced Activity of $PdTiO_2$ Catalysts for the COH_2 Reaction in the Absence of Strong Metal-Support Interactions (SMSI). *Journal of Catalysis* **1984**, *86*, 384–391.
23. Conner, W., Jr Spillover in Heterogeneous Catalysis - Chemical Reviews (ACS Publications). *Chem. Rev.* **1995**.
24. Uchijima, T. SMSI Effect in Some Reducible Oxides Including Niobia. *Catalysis Today* **1996**.
25. Santiesteban, J.; Calabro, D.; Borghard, W. H-Spillover and SMSI Effects in Paraffin Hydroisomerization Over Pt/WOx/ZrO_2Bifunctional Catalysts. *Journal of Catalysis* **1999**.
26. Pereira, M.; Noronha, F. SMSI Effect in the Butadiene Hydrogenation on Pd-Cu Bimetallic Catalysts. *Catalysis Today* **1993**.
27. Ferdousi, B. N.; Mominul Islam, M.; Okajima, T.; Mao, L.; Ohsaka, T. Enhanced Catalytic Reduction of Oxygen at Tantalum Deposited Platinum Electrode. *Chem. Commun.* **2010**, *46*, 1165.

28. Wang, S.; Moon, S. The Effect of SMSI (Strong Metal-Support Interaction) Behavior on CO Adsorption and Hydrogenation on Pd Catalysts. *Journal of Catalysis* **1981**, *71*, 167–174.
29. Lu, C.; Lin, Y. Naphthalene Hydrogenation Over Pt/TiO_2-ZrO_2 and the Behavior of Strong Metal-Support Interaction (SMSI). *Applied Catalysis A-General* **2000**.
30. Badyal, J.; Lambert, R.; Harrison, K.; Riley, C. Investigation of the SMSI Phenomenon with TiO2/Ru/SiO2 Model-Dispersed Catalysts. *Journal of Catalysis* **1991**.
31. Masud, J.; Alam, M. T.; Okajima, T.; Ohsaka, T. Catalytic Electrooxidation of Formaldehyde at Ta_2O_5-Modified Pt Electrodes. *Chem. Lett.* **2011**, *40*, 252–254.
32. Ruppert, A. Pt/ZrO_2/TiO_2 Catalysts for Selective Hydrogenation of Crotonaldehyde: Tuning the SMSI Effect for Optimum Performance. *Applied Catalysis A-General* **2007**.
33. Suzuki, T.; Souda, R. The Encapsulation of Pd by the Supporting TiO_2(110) Surface Induced by Strong Metal-Support Interactions. *Surface Science* **2000**, *448*, 33–39.
34. Caballero, A.; Holgado, J.; Gonzalez-delaCruz, V. In Situ Spectroscopic Detection of SMSI Effect in a Ni/CeO_2 System: Hydrogen-Induced Burial and Dig Out of Metallic Nickel. *Chem Commun* **2009**.
35. Masuda, T.; Fukumitsu, H.; Fugane, K.; Togasaki, H.; Matsumura, D.; Tamura, K.; Nishihata, Y.; Yoshikawa, H.; Kobayashi, K.; Mori, T.; *et al.* Role of Cerium Oxide in the Enhancement of Activity for the Oxygen Reduction Reaction at Pt–CeO xNanocomposite Electrocatalyst - an in Situ Electrochemical X-Ray Absorption Fine Structure Study. *J Phys Chem C* **2012**, *116*, 10098–10102.
36. Baker, R.; Prestridge, E. Electron Microscopy of Supported Metal Particles: I. Behavior of Pt on Titanium Oxide, Aluminum Oxide, Silicon Oxide, and Carbon. *Journal of Catalysis* **1979**.
37. Baker, R.; Prestridge, E. Electron Microscopy of Supported Metal Particles II. Further Studies of Pt/TiO_2. *Journal of Catalysis* **1979**.
38. Baker, R.; Prestridge, E. Electron Microscopy of Supported Metal Particles: III. the Role of the Metal in an SMSI Interaction. *Journal of Catalysis* **1983**.
39. Robertson, I. M.; Schuh, C. A.; Vetrano, J. S.; Browning, N. D.; Field, D. P.; Jensen, D. J.; Miller, M. K.; Baker, I.; Dunand, D. C.; Dunin-Borkowski, R.; *et al.* Towards an Integrated Materials Characterization Toolbox. *J Mater Res* **2011**, *26*, 1341–1383.
40. Kelley, M.; Short, D. In Situ TEM and ISS Studies of Supported Metal "SMSI" Catalysts. *Journal of Molecular Catalysis* **1983**, *20*, 235–249.

41. Blankenburg, K. Reversal of the SMSI State on Pt/Ti02 by CO Hydrogenation. *Journal of Catalysis* **1991**.
42. Bernal, S.; Calvino, J. J.; Cauqui, M. A.; Gatica, J. M.; López Cartes, C.; Pérez Omil, J. A.; Pintado, J. M. Some Contributions of Electron Microscopy to the Characterisation of the Strong Metal–Support Interaction Effect. *Catalysis Today* **2003**, *77*, 385–406.
43. Iddir, H.; Skavysh, V.; Ogut, S.; Browning, N.; Disko, M. Preferential Growth of Pt on Rutile TiO2. *Phys. Rev. B* **2006**, *73*.
44. Iddir, H.; Disko, M.; Ogut, S. Atomic Scale Characterization of the Pt/TiO_2 Interface. *Micron* **2005**.
45. Ou, D. R.; Mori, T.; Fugane, K.; Togasaki, H.; Ye, F.; Drennan, J. Stability of Ceria Supports in $Pt–CeO_X/C$ Catalysts. *J Phys Chem C* **2011**, *115*, 19239–19245.
46. Awaludin, Z.; Suzuki, M.; Masud, J.; Okajima, T.; Ohsaka, T. Enhanced Electrocatalysis of Oxygen Reduction on $Pt/TaO_X/GC$. *J Phys Chem C* **2011**, *115*, 25557–25567.
47. Awaludin, Z.; Sheng, J. M. G.; Okajima, T.; Ohsaka, T. Effects of TaOx on Pt Composite Catalysts for Oxygen. *Langmuir* **2012**, 1–40.
48. Sheng, T.; Guoxing, X. The Nature of the SMSI State of the Pt/TiO_2 System. *Journal of Catalysis* **1988**.
49. Nobile, A. Importance of the Anatase-Rutile Phase Transition and Titania Grain Enlargement in the Strong Metal-Support Interaction Phenomenon in Fe/TiO_2 Catalysts. *Journal of Catalysis* **1989**, *116*, 383–398.
50. Yoshitake, H.; Iwasawa, Y. Electronic Metal Support Interaction in Platinum Catalysts Under Deuterium-Ethene Reaction Conditions and the Microscopic Nature of the Active Sites. *J. Phys. Chem.* **1992**, *96*, 1329–1334.
51. Fugane, K.; Mori, T.; Ou, D. R.; Suzuki, A.; Yoshikawa, H.; Masuda, T.; Uosaki, K.; Yamashita, Y.; Ueda, S.; Kobayashi, K.; *et al.* Activity of Oxygen Reduction Reaction on Small Amount of Amorphous CeOx Promoted Pt Cathode for Fuel Cell Application. *Electrochimica Acta* **2011**, *56*, 3874–3883.
52. Ou, D. R.; Mori, T.; Togasaki, H.; Takahashi, M.; Ye, F.; Drennan, J. Microstructural and Metal–Support Interactions of the $Pt–CeO_2/C$ Catalysts for Direct Methanol Fuel Cell Application. *Langmuir* **2011**, *27*, 3859–3866.
53. Zhao, Y.; Feltes, T. E.; Regalbuto, J. R.; Meyer, R. J.; Klie, R. F. An Analytical Scanning Transmission Electron Microscopy Study of the Support Effects on Mn-Promoted Co Fischer–Tropsch Catalysts. *Catal. Sci. Technol.* **2011**, *1*, 1483.
54. Fugane, K.; Mori, T.; Ou, D. R.; Yan, P.; Ye, F.; Yoshikawa, H.; Drennan, J. Improvement of Cathode Performance on $Pt\text{-}CeO_X$ by Optimization of Electrochemical Pretreatment Condition for PEFC Application. *Langmuir*

2012, *28*, 16692–16700.
55. Vaughan, O. A Golden Opportunity. *Nature Nanotech* **2010**, *5*, 5–7.
56. Lee, I.; Morales, R.; Albiter, M. A.; Zaera, F. Synthesis of Heterogeneous Catalysts with Well Shaped Platinum Particles to Control Reaction Selectivity. *Proceedings of the National Academy of Sciences* **2008**, *105*, 15241–15246.
57. Brunauer, S.; Emmett, P. H.; Teller, E. Adsorption of Gases in Multimolecular Layers. *J. Am. Chem. Soc.* **1938**, *60*, 309–319.
58. Tauster, S. J.; Fung, S. C.; Garten, R. L. Strong Metal-Support Interactions. Group 8 Noble Metals Supported on Titanium Dioxide. *J. Am. Chem. Soc.* **1978**, *100*, 170–175.
59. Datye, A. Electron Microscopy of Catalysts: Recent Achievements and Future Prospects. *Journal of Catalysis* **2003**.
60. Tauster, S. J.; Fung, S. C.; Baker, R. T. K.; Horsley, J. A. Strong Interactions in Supported-Metal Catalysts. *Science* **1981**, *211*, 1121–1125.
61. Baker, R. T. K.; Tauster, S. J.; Dumesic, J. A. Strong Metal-Support Interactions. **1986**.
62. Tauster, S. J. Strong Metal-Support Interactions. *Acc. Chem. Res.* **1987**, *20*, 389–394.
63. Brewer, L. Bonding and Structures of Transition Metals. *Science* **1968**, *161*, 115–122.
64. Zhou, W.; Wachs, I. E.; Kiely, C. J. Nanostructural and Chemical Characterization of Supported Metal Oxide Catalysts by Aberration Corrected Analytical Electron Microscopy. *Curr Opin Solid St M* **2012**, *16*, 10–22.
65. Neophytides, S. G.; Zafeiratos, S. H.; Jaksic, M. M. Novel Trends in ELectrocatalysis: Extended Brewer Hypo-Hyper-D-Interionic Bonding Theory and Selective Interactive Grafting of Composite Bifunctional Eletrocatalysts for Simultaneous Anodic Hydrogen and CO Oxidation. *Chem. Ind.* **2003**, *57*, 368–392.
66. Ardenne, von, M.; Beischer, D. Untersuchungen Von Katalysatoren Mit Dem Universal-Elektronenmikroskop. *Angewandte Chemie* **1940**, *53*, 103–107.
67. Turkevich, J. Electron Microscopy of Catalysts. *The Journal of Chemical Physics* **1945**, *13*, 235.
68. Crewe, A. V. A High-Resolution Scanning Transmission Electron Microscope. *J Appl Phys* **1968**, *39*, 5861.
69. Iijima, S. High-Resolution Electron Microscopy of Crystal Lattice of Titanium-Niobium Oxide. *J Appl Phys* **1971**, *42*, 5891.
70. Crewe, A. V.; Wall, J.; Langmore, J. Visibility of Single Atoms. *Science* **1970**,

168, 1338–1340.

71. Stroud, A. N.; Welter, L. M.; Resh, D. A.; Habeck, D. A.; Crewe, A. V.; Wall, J. Scanning Electron Microscopy of Cells. *Science* **1971**, *164*, 830–832.
72. James, E.; Browning, N. Practical Aspects of Atomic Resolution Imaging and Analysis in STEM. *Ultramicroscopy* **1999**, *78*, 125–139.
73. Pennycook, S.; Rafferty, B.; Nellist, P. Z-Contrast Imaging in an Aberration-Corrected Scanning Transmission Electron Microscope. *Microsc Microanal* **2000**, *6*, 343–352.
74. Bell, A. T. The Impact of Nanoscience on Heterogeneous Catalysis. *Science* **2003**, *299*, 1688–1691.
75. Rolison, D. R. Catalytic Nanoarchitectures--the Importance of Nothing and the Unimportance of Periodicity. *Science* **2003**, *299*, 1698–1701.
76. Howe, J. M.; Oleshko, V. P. Application of Valence Electron Energy-Loss Spectroscopy and Plasmon Energy Mapping for Determining Material Properties at the Nanoscale. *J Electron Microsc* **2004**, *53*, 339–351.
77. Ziese, U.; de Jong, K. P.; Koster, A. J. Electron Tomography: a Tool for 3D Structural Probing of Heterogeneous Catalysts at the Nanometer Scale. *Applied Catalysis A-General* **2004**, *260*, 71–74.
78. Liu, J. Scanning Transmission Electron Microscopy and Its Application to the Study of Nanoparticles and Nanoparticle Systems. *J Electron Microsc* **2005**, *54*, 251–278.
79. Browning, N. D.; Chisholm, M. F.; Pennycook, S. J. Atomic-Resolution Chemical Analysis Using a Scanning Transmission Electron Microscope (Vol 366, Pg 143, 1993). *Nature* **2006**, *444*, 235–235.
80. Kiely, C. Electron Microscopy: New Views of Catalysts. *Nature Publishing Group* **2010**, *9*, 296–297.
81. Herzing, A. A.; Kiely, C. J.; Carley, A. F.; Landon, P.; Hutchings, G. J. Identification of Active Gold Nanoclusters on Iron Oxide Supports for CO Oxidation. *Science* **2008**, *321*, 1331–1335.
82. Su, D. S.; Jacob, T.; Hansen, T. W.; Wang, D.; Schlögl, R.; Freitag, B.; Kujawa, S. Surface Chemistry of Ag Particles: Identification of Oxide Species by Aberration-Corrected TEM and by DFT Calculations. *Angew. Chem. Int. Ed.* **2008**, *47*, 5005–5008.
83. Allard, L. F.; Bigelow, W. C.; Jose-Yacaman, M.; Nackashi, D. P.; Damiano, J.; Mick, S. E. A New MEMS-Based System for Ultra-High-Resolution Imaging at Elevated Temperatures. *Microscopy Research and Technique* **2009**, *72*, 208–215.
84. Allard, L. F.; Borisevich, A.; Deng, W.; Si, R.; Flytzani-Stephanopoulos, M.; Overbury, S. H. Evolution of Gold Structure During Thermal Treatment of Au/FeOx Catalysts Revealed by Aberration-Corrected

Electron Microscopy. *J Electron Microsc* **2009**, *58*, 199–212.
85. Kwon, O.-H.; Zewail, A. H. 4D Electron Tomography. *Science* **2010**, *328*, 1668–1673.
86. Evans, J. E.; Jungjohann, K. L.; Browning, N. D.; Arslan, I. Controlled Growth of Nanoparticles From Solution with in Situ Liquid Transmission Electron Microscopy. *Nano Lett* **2011**, *11*, 2809–2813.
87. Scott, M. C.; Chen, C.-C.; Mecklenburg, M.; Zhu, C.; Xu, R.; Ercius, P.; Dahmen, U.; Regan, B. C.; Miao, J. Electron Tomography at 2.4-Ångström Resolution. *Nature* **2012**, *483*, 444–447.
88. Yoshida, H.; Kuwauchi, Y.; Jinschek, J. R.; Sun, K.; Tanaka, S.; Kohyama, M.; Shimada, S.; Haruta, M.; Takeda, S. Visualizing Gas Molecules Interacting with Supported Nanoparticulate Catalysts at Reaction Conditions. *Science* **2012**, *335*, 317–319.
89. Thomas, J. Electron Microscopy and the Materials Chemistry of Solid Catalysts. *Advances in Catalysis* **2004**.
90. Midgley, P. A.; Weyland, M. 3D Electron Microscopy in the Physical Sciences: the Development of Z-Contrast and EFTEM Tomography. *Ultramicroscopy* **2003**, *96*, 413–431.
91. Du, K.; Ernst, F.; Pelsozy, M. C.; Barthel, J.; Tillmann, K. Expansion of Interatomic Distances in Platinum Catalyst Nanoparticles. *Acta Mater* **2010**, *58*, 836–845.
92. Jensen, T.; Lauritsen, J.; Helveg, S. Effect of Particle Morphology on the Ripening of Supported Pt Nanoparticles. *The Journal of…* **2012**.
93. Nørskov, J. K.; Rossmeisl, J.; Logadottir, A.; Lindqvist, L.; Kitchin, J. R.; Bligaard, T.; Jónsson, H. Origin of the Overpotential for Oxygen Reduction at a Fuel-Cell Cathode. *J. Phys. Chem. B* **2004**, *108*, 17886–17892.
94. Stamenkovic, V. R.; Mun, B. S.; Arenz, M.; Mayrhofer, K. J. J.; Lucas, C. A.; Wang, G.; Ross, P. N.; Markovic, N. M. Trends in Electrocatalysis on Extended and Nanoscale Pt-Bimetallic Alloy Surfaces. *Nature Publishing Group* **2007**, *6*, 241–247.
95. Chan, M. C. Y.; Chen, L.; Nan, F.; Britten, J. F.; Bock, C.; Botton, G. A. Structure, Ordering, and Surfaces of Pt–Fe Alloy Catalytic Nanoparticles From Quantitative Electron Microscopy and X-Ray Diffraction. *Nanoscale* **2012**, *4*, 7273.
96. Ortalan, V.; Uzun, A.; Gates, B. C.; Browning, N. D. Towards Full-Structure Determination of Bimetallic Nanoparticles with an Aberration-Corrected Electron Microscope. *Nature Nanotech* **2010**, *5*, 843–847.
97. Williams, D. B.; Carter, C. B. *Transmission Electron Microscopy: a Textbook for Materials Science (4 Vol Set)*; A Textbook for Materials Science; 2nd ed. Springer, 2009; p. 760.

98. Hawkes, P.; Spence, J. C. H. *Science of Microscopy*; Springer Science & Business Media, 2008; p. 766.
99. Grogger, W.; Hofer, F.; Kothleitner, G.; Schaffer, B. An Introduction to High-Resolution EELS in Transmission Electron Microscopy. *Topics in Catalysis* **2008**, *50*, 200–207.
100. Graham, U. M.; Khatri, R. A.; Dozier, A.; Jacobs, G.; Davis, B. H. 3D Ridge-Valley Structure of a Pt-Ceria Catalyst: HRTEM and EELS Spectrum Imaging. *Catalysis Letters* **2009**, *132*, 335–341.
101. Lazar, S.; Shao, Y.; Gunawan, L.; Nechache, R.; Pignolet, A.; Botton, G. A. Imaging, Core-Loss, and Low-Loss Electron-Energy-Loss Spectroscopy Mapping in Aberration-Corrected STEM. In *Microscopy and Microanalysis*; 2010; Vol. 16, pp. 416–424.
102. Stoyanov, E.; Langenhorst, F.; Steinle-Neumann, G. The Effect of Valence State and Site Geometry on Ti L3,2 and O K Electron Energy-Loss Spectra of TixOy Phases. *American Mineralogist* **2007**, *92*, 577–586.
103. Botton, G. A. Probing Bonding and Electronic Structure at Atomic Resolution with Spectroscopic Imaging. *Mrs Bull* **2012**, *37*, 21–28.
104. Braidy, N.; Jakubek, Z. J.; Simard, B.; Botton, G. A. Quantitative Energy Dispersive X-Ray Microanalysis of Electron Beam-Sensitive Alloyed Nanoparticles. *Microsc Microanal* **2008**, *14*, 166–175.
105. Botton, G. A.; Lazar, S.; Dwyer, C. Elemental mapping at the atomic scale using low accelerating voltages. In *Ultramicroscopy*; 2010; Vol. 110, pp. 926–934.
106. Zhao, Y.; Feltes, T. E.; Regalbuto, J. R.; Meyer, R. J.; Klie, R. F. In-Situ Electron Energy Loss Spectroscopy Study of Mn-Promoted Co/TiO2 Fischer–Tropsch Catalysts. *Catalysis Letters* **2011**, *141*, 641–648.
107. Weyland, M. Electron Tomography of Catalysts. *Topics in Catalysis* **2002**, *21*, 175–183.
108. Weyland, M.; Midgley, P. A. Electron Tomography. *Materials Today* **2004**, *7*, 32–40.
109. Gommes, C. J.; de Jong, K.; Pirard, J.-P.; Blacher, S. Assessment of the 3D Localization of Metallic Nanoparticles in Pd/SiO_2 Cogelled Catalysts by Electron Tomography. *Langmuir* **2005**, *21*, 12378–12385.
110. Xin, H. L.; Mundy, J. A.; Liu, Z.; Cabezas, R.; Hovden, R.; Kourkoutis, L. F.; Zhang, J.; Subramanian, N. P.; Makharia, R.; Wagner, F. T.; *et al.* Atomic-Resolution Spectroscopic Imaging of Ensembles of Nanocatalyst Particles Across the Life of a Fuel Cell. *Nano Lett* **2012**, *12*, 490–497.
111. Midgley, P. A.; Yates, T.; Arslan, I.; Tong, J.; Thomas, J. M. Electron Tomography for Nanoscale Materials Science. *Microsc Microanal* **2005**, *11*.
112. Midgley, P. A.; Ward, E. P. W.; Hungría, A. B.; Thomas, J. M.

Nanotomography in the Chemical, Biological and Materials Sciences. *Chem. Soc. Rev.* **2007**, *36*, 1477.

113. Saghi, Z.; Midgley, P. A. Electron Tomography in the (S)TEM: From Nanoscale Morphological Analysis to 3D Atomic Imaging. *Annu. Rev. Mater. Res.* **2012**, *42*, 59–79.
114. Scott, M. C.; Chen, C.-C.; Mecklenburg, M.; Zhu, C.; Xu, R.; Ercius, P.; Dahmen, U.; Regan, B. C.; Miao, J. Electron Tomography at 2.4 Å Resolution. *arXiv* **2011**, *cond-mat.mtrl-sci*.
115. Zhang, L.; Kim, J.; Chen, H.; Nan, F.; Dudeck, K. … -Shell Structured Electrocatalyst with Ru Rich in Core and Pt Rich in Shell for Hydrogen Oxidation Reaction and Its Implication in Proton Exchange Membrane Fuel Cell. *Journal of Power …* **2011**.
116. Alayoglu, S.; Nilekar, A. U.; Mavrikakis, M.; Eichhorn, B. Ru–Pt Core–Shell Nanoparticles for Preferential Oxidation of Carbon Monoxide in Hydrogen. *Nature Materials* **2008**, *7*, 333–338.
117. Strasser, P.; Koh, S.; Anniyev, T.; Greeley, J.; More, K.; Yu, C.; Liu, Z.; Kaya, S.; Nordlund, D.; Ogasawara, H.; *et al.* Lattice-Strain Control of the Activity in Dealloyed Core–Shell Fuel Cell Catalysts. *Nature Chem* **2010**, *2*, 454–460.
118. Zhang, L.; Kim, J.; Zhang, J.; Nan, F.; Gauquelin, N.; Botton, G. A.; He, P.; Bashyam, R.; Knights, S. Ti4O7 Supported Ru@Pt Coreâ€"Shell Catalyst for CO-Tolerance in PEM Fuel Cell Hydrogen Oxidation Reaction. *Applied Energy* **2013**, *103*, 507–513.
119. Chorkendorff, I.; Niemantsverdriet, J. W. *Concepts of Modern Catalysis and Kinetics*; John Wiley & Sons, 2006; p. 469.
120. Zhang, L.; Kim, J.; Zhang, J.; Nan, F.; Gauquelin, N. Ti 4 O 7 Supported Ru@ Pt Core–Shell Catalyst for CO-Tolerance in PEM Fuel Cell Hydrogen Oxidation Reaction. *Applied Energy* **2013**.
121. Spencer, M. Models of Strong Metal-Support Interaction (SMSI) in Pt on TiO2 Catalysts. *Journal of Catalysis* **1985**.
122. Badyal, J.; Gellman, A. Model Studies of the SMSI Phenomenon: I. Co and Hydrogen Chemistry at the Ru---Ti Interface. *Journal of Catalysis* **1988**.
123. Jennison, D.; Dulub, O.; Hebenstreit, W. Structure of an Ultrathin TiO X Film, Formed by the Strong Metal Support Interaction (SMSI), on Pt Nanocrystals on TiO 2(110). *Surface Science* **2001**.
124. Papakonstantinou, G. D.; Jaksic, J. M.; Labou, D.; Siokou, A.; Jaksic, M. M. Spillover Phenomena and Its Striking Impacts in Electrocatalysis for Hydrogen and Oxygen Electrode Reactions. *Advances in Physical Chemistry* **2011**, *2011*, 1–22.
125. Jaksic, J. M.; Labou, D.; Papakonstantinou, G. D.; Siokou, A.; Jaksic, M. M.

Novel Spillover Interrelating Reversible Electrocatalysts for Oxygen and Hydrogen Electrode Reactions. *J Phys Chem C* **2010**, *114*, 18298–18312.

126. Nan, F.; Song, C.; Zhang, J.; Hui, R.; Chen, J.; Fairbridge, C.; Botton, G. A. STEM HAADF Tomography of Molybdenum Disulfide with Mesoporous Structure. *ChemCatChem* **2011**, *3*, 999–1003.

127. Shao, Y.; Maunders, C.; Rossouw, D.; Kolodiazhnyi, T.; Botton, G. A. Quantification of the Ti Oxidation State in BaTi1−xNbxO3 Compounds. *Ultramicroscopy* **2010**, *110*, 1014–1019.